Universität Hamburg
DER FORSCHUNG | DER LEHRE | DER BILDUNG

Zirconia microparticles and gold nanoshells: building blocks for novel functional materials in catalysis and high-temperature photonics

Zirkonia-Mikropartikel und Gold-Nanoschalen: Bausteine für neuartige funktionelle Materialen in Katalyse und Hochtemperatur-Photonik

DISSERTATION

zur Erlangung des Grades

"Doktor der Naturwissenschaften"(Dr. rer. nat.)

an der Fakultät für Mathematik, Informatik und Naturwissenschaften, Universität Hamburg

vorgelegt von

Gregor Thomas Dahl

Hamburg, 2020

Die praktischen Arbeiten zur vorliegenden Dissertation wurden am Institut für Physikalische Chemie in der Arbeitsgruppe von Prof. Dr. Horst Weller im Zeitraum vom 01.10.2016 bis 30.06.2020 durchgeführt. Sie waren Teil des Sonderforschungsbereichs "SFB 986 – Maßgeschneiderte Multiskalige Materialsysteme M^3" im Rahmen des Teilprojekts "C6 – Ceramic Microparticles: Building Blocks for High Temperature Photonic Materials".

Gutachter der Dissertation:	Dr. Tobias Vossmeyer
	Prof. Dr. Alf Mews
Gutachter der Disputation:	Prof. Dr. Horst Weller
	Prof. Dr. Michael Fröba
	Prof. Dr. Gabriel Bester
Datum der Disputation:	25.09.2020
Datum der Druckfreigabe:	30.09.2020

"The good thing about science is that it's true whether or not you believe in it." - Neil deGrasse Tyson

Meinen geliebten Eltern.

Acronyms

AAS	atomic absorption spectroscopy
APS	air plasma-spraying
APTES	3-aminopropyl triethoxysilane
CS	crystallite size
EB-PVD	electron-beam physical-vapor deposition
EDX	energy-dispersive X-ray spectroscopy
GHS	globally harmonized system
H- and P-statements	hazard and precautionary statements
HAADF	high-angle annular dark-field
HPC	hydroxypropyl cellulose
ICP	inductively coupled plasma
IR	infrared
OES	optical emission spectroscopy
PWF	phase weight fraction
rpm	revolutions per minute
SEM	scanning electron microscopy
STEM	scanning transmissions electron microscopy
TBC	thermal barrier coating
TEM	transmission electron microscopy
TEOS	tetraethyl orthosilicate
TGO	thermally grown oxide
THF	tetrahydrofuran
THPC	tetrakis(hydroxymethyl)phosphonium chloride
TOC	total organic carbon
TUHH	Hamburg University of Technology
UHH	University of Hamburg
UV	ultraviolet

vis	visible
w/o	without
w.r.t.	with respect to
XRD	X-ray diffraction
YSZ	yttria-stabilized zirconia

Formula Symbols

a	lattice parameter a
A	absorbance
A_{450}	absorbance at $\lambda = 450\,\text{nm}$
b	lattice parameter b
β	lattice parameter β
c	cubic
c	lattice parameter c
c_p	particle concentration
d	mean particle diameter
D	grain boundary diffusion coefficient
D_0	preexponential constant
ΔG	free enthalpy difference
ΔH	excess enthalpy
δ	grain boundary thickness
E_A	activation energy
$E_{A,c}$	activation energy of the catalyzed reaction
g	gravitational force equivalent
k_B	Boltzmann constant
λ	wavelength
m	monoclinic
M_b	grain boundary mobility
M_{w}	molecular weight
n	number of particles
Ω	atomic volume
σ	standard deviation
t	tetragonal
T	temperature

x variable stochiometric factor

Z number of formula units (per unit cell)

List of Figures

List of Tables

Contents

1 Zusammenfassung

Zirkonia Mikro- und Mesopartikel haben sich im Hinblick auf verschiedenste Anwendungsgebiete, z.B. Wärmedämmbeschichtungen, Strukturfarben, Thermophotovoltaik und heterogene Katalyse, zu einem interessanten Forschungsfeld entwickelt. Die in dieser Arbeit vorgestellten Ergebnisse leisten einen Beitrag zum Verständnis der Faktoren, die ihre Synthese und mikrostrukturellen Eigenschaften bei hohen Temperaturen beeinflussen. Darüber hinaus wird die Darstellung von komplexeren Metall-Keramik-Kompositmaterialien basierend auf Silika- und Zirkoniapartikeln thematisiert.

Es wird gezeigt, dass der Einsatz von Hydroxypropylcellulose und Eicosansäure als Stabilisatoren und eine behutsame Anpassung ihres Mischungsverhältnisses eine präzise Kontrolle der finalen Größe von Zirkonia-Mesopartikeln bei der Sol-Gel-Synthese ermöglichen. Dieser Ansatz erlaubt zudem ein gezieltes Ausgleichen von Einflüssen anderer Faktoren, z.B. die Reaktivität der Vorläuferverbindungen von Dotanden, auf die Partikelgröße. Eine gezielte Dotierung mit definierten Aluminagehalten bis $50\,mol\%$ wurde erfolgreich mittels Co-Präzipitation erreicht. Alumina-dotierte Zirkoniapartikel zeigten eine erhöhte Stabilität gegen Auseinanderbrechen bei Temperaturen bis $1000\,°C$. Der beobachtete Effekt konnte auf die zunehmende Stabilisierung der tetragonalen Kristallstruktur, die Unterdrückung der destruktiven martensitischen Phasentransformation und die Hemmung des Kornwachstums durch die Bildung von aluminareichen Domänen an den Korngrenzen zurückgeführt werden.

Zirkoniapartikel mit einer Codotierung von $8\,mol\%$ Yttria und $20\,mol\%$ Alumina zeigten eine sehr hohe thermische Stabilität, welche mit der von $8\,mol\%$ Yttria-monodotierten Zirkoniapartikeln vergleichbar ist. Jedoch wiesen codotierte Partikel im Vergleich zu Yttria-monodotierten Partikeln eine stärkere Hemmung des Kornwachstums bei $1400\,°C$ auf, wie Röntgenbeugungsanalysen zeigten. Auch hier ist die Entstehung diffusionshemmender aluminareicher Domänen zwischen den Körnern eine mögliche Erklärung für diese Beobachtung.

In einer weiteren Studie wird das kontrollierte Wachstum von geschlossenen Goldnanoschalen auf kugelförmigen Silikamesopartikeln mithilfe von Goldnanopartikel-Keimen gezeigt. Des Weiteren konnte eine äußere homogene Silikananoschale auf dieser Goldnanoschale abgeschieden werden. Elektronenmikroskopische Untersuchungen von gealterten Proben solcher Kompositpartikel zeigten eine erhebliche Segregation und die Bildung einer Camouflage-Struktur der Goldnanoschale nach einen Zeitraum von drei Monaten.

Als Ursachen werden die niedrige Adhäsion zwischen Silika und Gold sowie eine hohe Oberflächenenergie vermutet. Die mangelhafte Stabilität der Goldnanoschalen-Struktur im Silika@Gold-Partikelsystem stellt dessen Eignung für den Einsatz in photonischen Anwendungen, z.B. als Bausteine in selektiven Emitter-Metaoberflächen für die Thermo-photovoltaik, infrage. Eine Verwendung in anderen Bereichen, wie etwa in der Katalyse, ist jedoch denkbar.

Zuletzt wird die Synthese eines neuartigen Materialsystems vorgestellt: Zirkonia@Gold-Kompositpartikel konnten mittels Immobilisierung von Goldnanopartikeln auf der Oberfläche von Zirkonia-Mesopartikeln und anschließender reduktiver Abscheidung von Gold dargestellt werden. Die permanente Anhaftung der Goldnanopartikel auf der Zirkoniaoberfläche wurde durch elektrostatische Kopplung mithilfe des bifunktionellen Haftvermittlers Aminomethylphosphonsäure sowie durch pH-Optimierung mit Salzsäure erreicht. Abschließend wurde das inkrementelle Aufwachsen von Gold während des zyklischen Abscheidungsprozesses anhand von elektronenmikroskopischen und elementanalaytischen Untersuchungen charakterisiert.

2 Abstract

Zirconia micro- and mesoparticles have come to be an interesting field of research within the scope of a wide range of applications, e.g., thermal barrier coatings, structural coloration, thermophotovoltaics, and heterogeneous catalysis. The results presented in this work contribute to the understanding of the factors that govern their synthesis and microstructural properties at high temperatures. The preparation of more complex metal-ceramic composite material systems based on silica and zirconia particles is also addressed.

It is demonstrated that the use of hydroxypropyl cellulose and eicosanoic acid as stabilizers as well as careful adjustment of their mixing ratio enable the precise control over the final particle size during the sol-gel synthesis of zirconia mesoparticles. This approach also enables the compensation of impacts of other factors, e.g., the reactivity of dopant precursors, on the particle size. Moreover, targeted doping with defined amounts of alumina of up to 50 mol% was successfully accomplished by co-precipitation. Alumina-doped zirconia particles showed an increased stability against disintegration at temperatures of up to 1000 °C. The observed effect was attributed to the stabilization of the tetragonal polymorph, the suppression of the destructive martensitic phase transition, and the attenuation of grain growth by the formation of inter-grain alumina-rich domains.

Zirconia particles codoped with yttria (8 mol%) and alumina (20 mol%) exhibited high thermal stability similar to that of 8 mol% yttria-monodoped zirconia particles. However, in contrast to yttria-monodoped samples, codoped particles exhibited a superior attenuation of grain growth at 1400 °C, as X-ray diffraction analysis revealed. Likewise, the formation of alumina-rich domains between neighboring grains was proposed to explain this observation.

In a further study the controlled growth of closed gold nanoshells on silica mesospheres via gold nanoparticle seeding is reported. Moreover, an outer silica nanoshell could be deposited homogeneously on top of the gold shell. Electron microscopy imaging of aged samples of such composite particles revealed the substantial segregation of gold and the formation of a camouflage structure over the course of three months. The origin of this effect is presumed to be the poor adhesion between silica and gold and a high surface energy. The deficient long-term stability of the gold nanoshell morphology in the silica@gold particle system questions its suitability for photonic applications,

e.g., as building blocks in selective emitter metasurfaces for thermophotovolotaics. The employment in other fields of interest, such as catalysis, however, is conceivable.

Finally, the preparation of a novel material system is reported: Zirconia@gold composite particles could be prepared by gold nanoparticle immobilization on the surface of calcined zirconia mesoparticles and subsequent gold deposition by seeded reduction. The permanent attachment of gold nanoparticles on the zirconia surface was achieved by electrostatic coupling using the bifunctional linker aminomethylphosphonic acid and by optimization of the pH via acidification with hydrochloric acid. Lastly, the incremental gold deposition during the cyclic seeded growth process was characterized using electron microscopy and elemental analysis.

3 Introduction

In a rapidly growing global community with a concurrently increasing demand for continual supply of energy, mobility, and cheap consumer goods, expectations on science are high to deliver fast solutions for these needs. At the same time, we are facing urgent challenges in terms of environmental impacts and climate change, that require new approaches towards sustainability in existing and future technologies. Besides efforts on the political level, research plays a key role in tackling these challenges. As a consequence, the focus of many researchers is continuously shifting towards the corresponding scientific topics.

In this context, the targeted manipulation of existing and the development of novel functional materials with improved properties have become major goals. Therefore, a thorough understanding of the processes governing these properties is essential. In this dissertation, new fabrication approaches to novel ceramic materials as well as several studies concerning their physical and chemical properties will be presented. This chapter will provide a fundamental overview of the motivation for the respective materials and potential applications. Moreover, related state-of-the-art literature will be reviewed and some fundamental knowledge, necessary for the understanding of the results and respective discussions, will be recapitulated.

3.1 Motivation

Ceramic microparticles have attracted significant interest in recent years, due to the wide range of their potential applications. They are being considered as building blocks for photonic materials, such as next-generation thermal barrier coatings or thermostable structural colorants. Furthermore, metal-ceramic composites based on such particles have caught attention in the context of metamaterials for thermophotovoltaics and are currently being considered as novel catalyst materials. In the following, the social importance of these fields and the underlying basic technological concepts will be introduced, briefly.

3.1.1 Thermal Barrier Coatings

Today, the major part of the global energy supply originates from fossil fuels. Natural gas is the only fossil source with a continuously growing share in primary energy.[1] Its combustion using industrial gas turbines contributed more than 23 % of the world's electrical power generation in 2017.[2] Beyond this, gas turbines are also an essential
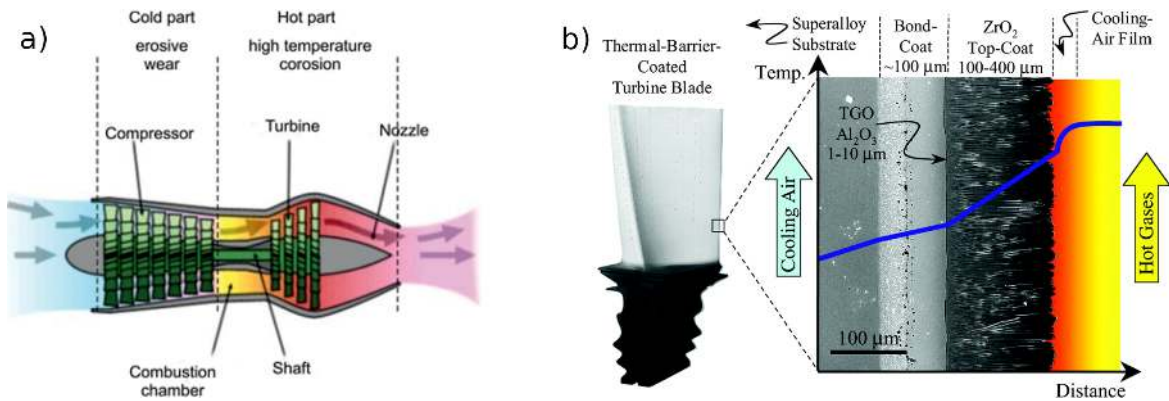
Figure 1: Thermal barrier coating in a gas turbine. a) Schematic illustration of a gas turbine. The combustion of the fuel generates very high temperatures, requiring thermal protection of the materials used in the hot part. Reprinted with permission from reference [4]. **b)** Cross-sectional scanning electron micrograph (SEM) of a commercial TBC, deposited by electron-beam physical-vapor deposition, and superimposed onto a schematic diagram showing the temperature gradient across the material layers. From [5]. Reprinted with permission from AAAS.

component of jet engines in the aviation sector, providing propulsion for most commercial airplanes. In 2018, the International Air Transport Association forecast that annual passenger numbers will nearly double to 8.2 billion by 2037.[3] With respect to these developments in power generation and air transportation, it is crucial to improve the efficiency and lifetime of gas turbines in order to satisfy the growing global demands in the near future.

A typical modern gas turbine is schematically illustrated in Figure 1a. It comprises a cold and a hot part. In the latter, injection of the fuel and combustion take place. The turbine blades are usually built from a nickel superalloy, which provides the required mechanical robustness but is limited in terms of thermal stability. For this reason, they are protected using a high temperature resistant multi-layer coating called thermal barrier coating (TBC), including a bond-coat, a very thin layer of thermally grown oxide (TGO), and a ceramic top-coat, as shown schematically in Figure 1b. It causes a significant temperature drop between the hot gas and the metallic blade, allowing for higher operating temperatures. This consequently increases both the energetic efficiency of the entire turbine and the cycle lifetime of the metallic blades. The state-of-the-art material for the top-coat is yttria-stabilized zirconia (YSZ), a high-performance ceramic, which combines very high chemical and thermal stability with favorable mechanical properties.[6] The most commonly used coating techniques are electron-beam physical-vapor deposition (EB-PVD) and air plasma spraying (APS).[5,6] Depending on the method, a columnar or lamellar microstructure, respectively, is obtained. Both processes

have different advantages and drawbacks regarding performance, cost, and lifetime.[6] For an improved TBC top-coat, novel microstructured zirconia-based materials, which exhibit a number of potential advantages over the conventional bulk structures, have been proposed recently.[7,8] While conventional coatings are practically transparent to infrared (IR) radiation, the reported three-dimensional assemblies of spherical microparticles cause a broadband reflection in the relevant spectral region, thus protecting the underlying material from a large portion of thermal radiation.[9] Due to the porosity of the structure, thermal conduction is also reduced significantly. As a consequence, the turbine operating temperature can be increased in order to reach a higher efficiency in energy conversion.[7] Therefore, such microparticle-based next-generation TBCs have the potential to increase gas turbine lifetime and reduce fuel consumption considerably.

3.1.2   Structural Coloration

Natural colorants have been used by our ancestors for tens of thousands of years, as prehistoric cave drawings impressively prove.[10] Ever since, coloration has successively broken its way into a growing number of application fields. In the 20th century, major progress in chemical synthesis initiated the success of synthetic colorants and mass coloration became a routine for many everyday life materials, e.g., paints, textiles, plastics, cosmetics, and food.[11] Many of them serve their purpose, but unresolved problems remain, particularly concerning the coloration of materials that need to withstand UV-irradiation or high temperatures during manufacturing or in their final application. Here, toxic and environmentally questionable substances, such as cadmium sulfoselenides, are still in use due to the lack of harmless alternatives.[12–14]

Traditionally, artificial colorants are based on pigments or dyes, where the color impression originates from selective absorption of light in the visible spectral region by contained chemical compounds. Later, it was recognized that some colors in nature, mostly blue shades,[15] are caused by a different phenomenon called *structural coloration*. Here, wavelength-selective reflection is induced by scattering of light in dielectric materials with a microscopic periodic or random arrangement, so-called *photonic structures*. Some impressive examples are shown in Figure 2. The characteristics of the optical behavior are mainly governed by the refractive indices of the involved materials and the geometry of the micrometer-sized features. Inspired by nature, several research groups have adapted this concept successfully in the recent past in order to design and tailor artificial structural colorants.[16]

With particular emphasis on high temperature stable colorants, a number of ceramic
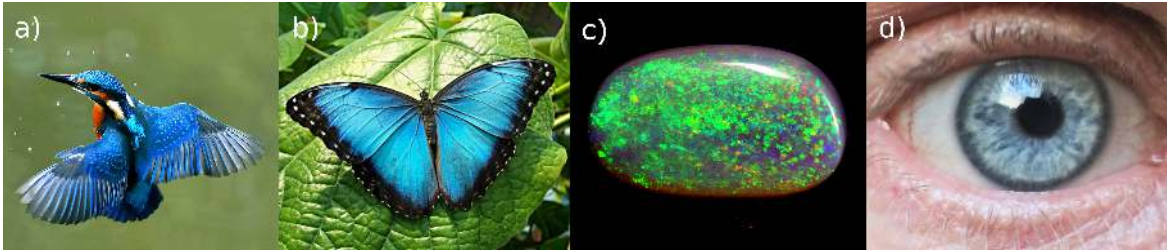
Figure 2: Structural coloration in nature. Selected examples for structural coloration in nature are **a)** a common kingfisher,[17] **b)** a morpho peleides,[18] **c)** a black opal,[19] and **d)** a blue human iris. The blue color impressions originate from microscopically structured arrangements, not from pigments. All images licensed under Creative Commons (a,b,c) or own work (d).

materials have been proposed recently, e.g., inverse opals,[20,21] hollow spheres,[14,22] and core@shell particles.[13,23] For the latter, ceramic submicrometer-sized spherical particles typically serve as the basic building blocks. For durable photonic properties at high temperatures, high shape persistence and good structural stability are crucial. Improvements concerning the thermal stability of ceramic microspheres are therefore one of several important contributions to the development of advanced ceramic structural colorants.

3.1.3   Thermophotovoltaics

With global deposits of fossil fuels drying up, yet the global demand for electrical power rising inexorably, a fundamental change in strategy for the generation of electricity is urgently required. Several renewable resources have evolved to contribute noticeably to the global power generation over the past decades. While hydropower and wind energy represent the greatest portion, the use of solar and other thermal energy continues to play only a minor role.[24] Although the progress in semiconductor technology enabled non-mechanical harvesting of solar energy, the intrinsically low efficiency of the most common material systems, e.g., silicon solar cells, remains a major drawback.[25] A closely related concept from the 1950s and 60s, that has not received broad attention until recent years, is thermophotovoltaic (TPV) energy conversion.[26–28] While a part of the sunlight is exploited in conventional photovoltaics, thermal radiation is used in TPV. The lower energy requires semiconductors of much smaller bandgap energies for efficient conversion.[27] As a consequence, heat sources with much lower temperatures than the sun can be employed, enabling a wide range of radiation sources. TPV systems can be used for primary power generation or waste-heat recovery and offer a number of advantages over conventional systems, e.g., portability, inexpensive maintenance, and
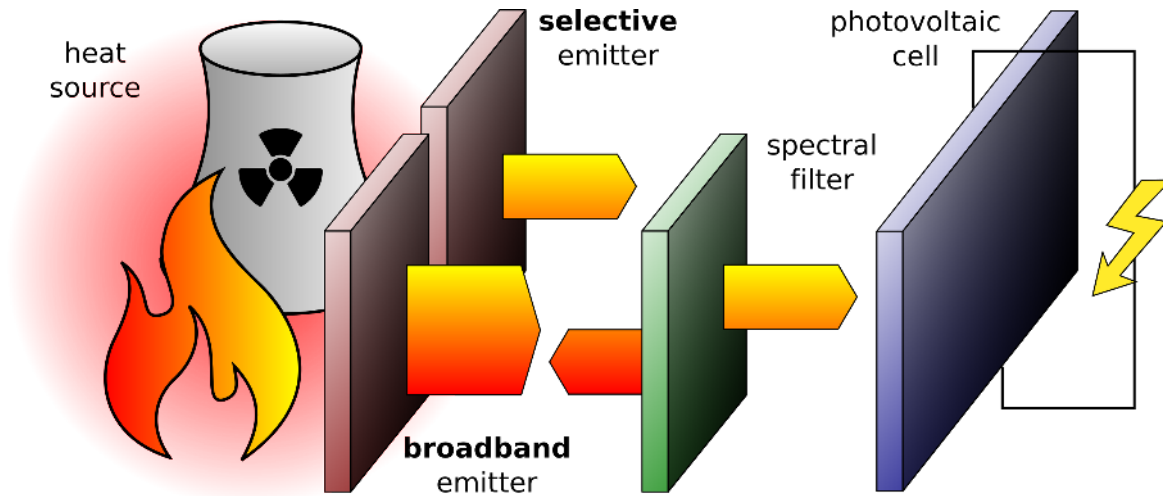
Figure 3: Thermophotovoltaic system. A TPV system includes at least a heat source, a thermal emitter, and a photovoltaic cell. Spectral control can be achieved by using a broadband emitter in combination with a spectral filter for photon recycling, or a selective emitter.

decreased pollutant emission.[26,27,29–31]

In a TPV system, the energy source transfers heat to an emitter, which sends it as thermal radiation to a photovoltaic cell with an appropriate electronic bandgap. This principle is illustrated in Figure 3. Here, only photons with an energy higher or equal to the bandgap induce an electric voltage, whereby the energy exceeding that of the bandgap reduces efficiency drastically and causes significant thermal loss. Therefore, a simple black body emitter is very inefficient, because only a small fraction of the emitted radiation is converted to electric power, while the greater part is wasted.[31] Current research in TPV therefore focuses on applicable ways of spectral control to increase the heat-to-power efficiency. Two concepts are under development: selective recycling of off-bandgap photons back to the emitter, and selective emission of in-bandgap photons by the emitter (see Figure 3), or combinations of both.[27]

Selective emitters receive heat from the energy source by radiation, convection, and conduction, which they transform to a narrowband radiation towards the PV cell.[32] In the past years, many research groups have made efforts to develop advanced selective emitter materials, as summarized recently in a comprehensive review.[33] Early materials for these components include ytterbia, erbia, holmia, and neodymia,[27] radiating at energies between 0.5 eV and 1.1 eV with typical operating temperatures of 1200 to 2000 K.[34] Here, the selective emission is based on electronic transitions.[33] More recent studies focus on photonic structures and metamaterials.[7,32,35] In this context, various material designs comprising dielectric and metallic components have
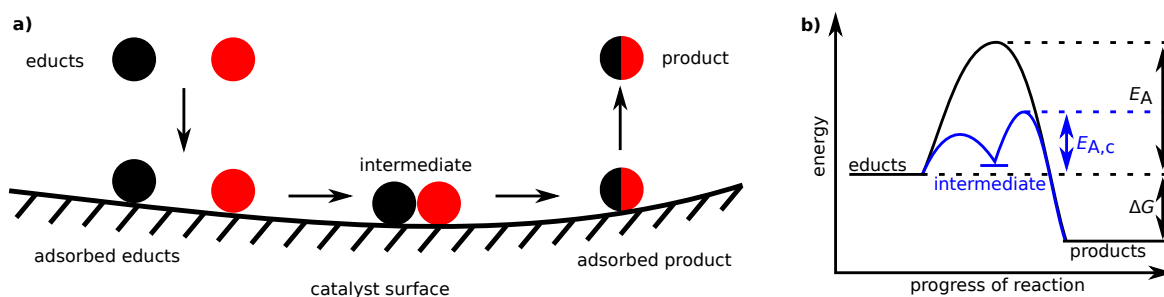
Figure 4: Heterogeneous catalysis. **a)** Schematic illustration of a simple, heterogeneously catalyzed reaction. The formation of the intermediate is only possible at the catlyst surface and provides an alternative mechanistic path from educts to product. **b)** Corresponding energy diagram. The reaction speed of the uncatalyzed reaction is determined by the activation energy E_A. The alternative reaction path via an intermediate lowers the highest kinetic barrier and therefore also the activation energy of the catalyzed reaction $E_{A,c}$. The free enthalpy difference ΔG is independent of the reaction path. All images adapted and reprinted with permission from reference [44].

been proposed, including core@shell structures, among others.[36–39] While theoretical conversion efficiency has improved substantially, long-term thermal stability of the emitter units remains a major practical challenge.

3.1.4   Heterogeneous Catalysis

Over the past century, catalysts have become an indispensable factor in the chemical industry and more recently in environmental control. Approximately 80 to 90 % of all processes in chemistry and petrochemistry involve at least one catalyzed step.[40,41] Moreover, catalysis plays an important role in gas cleaning and downstream oxidation for environmental protection.[42] Catalytic processes can be of homogeneous or heterogeneous nature, depending on whether the catalyst and reactants are in the same or different physical states. On an industrial scale, heterogeneous catalysis is by far the more common type, because it enables facile catalyst separation and regeneration.[43] Usually, solid state catalysts are employed, while reactants are present in the liquid or gaseous phase. Typical examples for large-scale applications are the production of ammonia, sulfuric acid, polymers, petrochemicals, bulk and fine chemicals.[41] Moreover, catalysts play an important role in oil refining.

Catalysts in general do not have an impact on the thermodynamic equilibrium of a reaction. They provide an alternative mechanistic reaction path involving one or more intermediates with catalyst participation, thus changing the overall kinetic barriers and, hence, the reaction speed. This mechanism is illustrated in Figure 4. In heterogeneous catalysis, the key steps are surface processes. For this reason, associated catalyst

properties, such as specific surface area, porosity, texture, and surface chemistry are crucial parameters.

By today, the variety of catalyst materials is enormous. They include various metals, metal oxides, solid state acids and bases, and complex composite materials. The types of catalyzed reactions are very specific for the different materials and range from hydrogenation, hydrogenolysis, and (partial) oxidation to dehydration, (de-)hydratization, (hydro)cracking, and isomerization, as well as hydrogen transfer.[43] Bi-functional catalysts represent a more complex class of materials, where two or more components provide active sites and contribute to the collective catalyst activity.[43] The fabrication of such materials requires a high degree of control during synthesis. While the catalysis community has developed a large number of methods for large-scale catalyst fabrication, means for high-precision design of complex catalyst materials is still lacking.[45] Recent progress in nanotechnology has led to a new availability of tools for the accurate design of new and complex nanostructured catalysts.[46] In this context, the exploration of synthetic approaches for innovative and complex materials makes an important contribution to the development of next-generation catalysts.

3.2   Zirconium Dioxide

Zirconium dioxide (ZrO_2), also known as zirconia, is one of the most widely used ceramic materials today. Since the nineteen-seventies, zirconia-based ceramics have been made use of in mechanical engineering. Due to their remarkably high strength, hardness, fracture toughness, and wear resistance, they are well-suited for various components, e.g., engine parts, cutting tools, and dentures.[47–50] Furthermore, the high ionic conductivity and chemical inertness of zirconia have enabled it to serve as a functional material in sensors and fuel cells.[51–54] Also, a high refractive index gives rise to the field of optical applications, for instance in structural coloration or thermophotovoltaics.[22,23,38,55] Some of the most esteemed properties, however, are its low thermal conductivity, thermal shock resistance, and high melting temperature, making it a material of choice in high temperature environments.[56–61] For this reason, zirconia is the preferred material for protective coatings, for example in TBCs used in airplane engines and gas turbines for power generation.[62] Other uses of zirconia include chromatography, catalysis, and biomedical applications.[48,63–67]

The high temperature behavior of zirconia materials is therefore of great relevance for its most important applications. When pure zirconia is subjected to temperatures of several hundred degrees centigrade or higher, structural degradation is often observed.
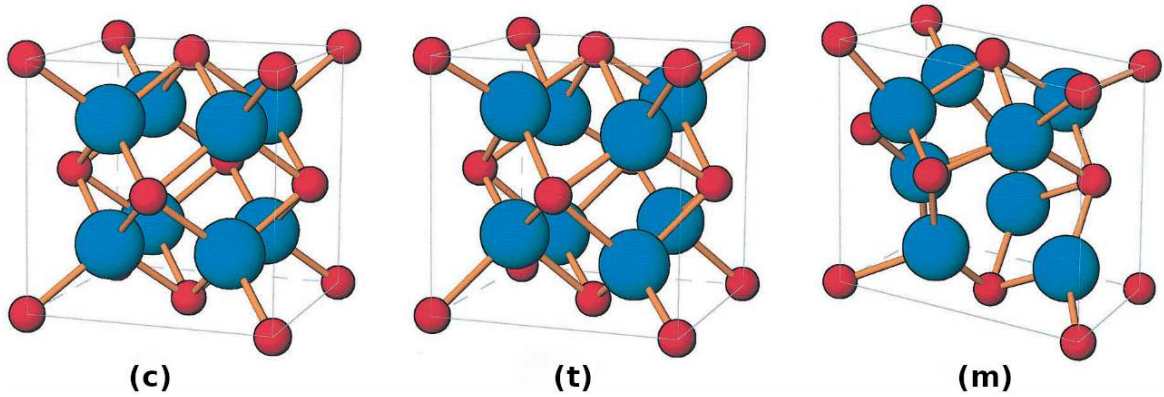
Figure 5: Crystal modifications of zirconia. Schematic representation of the three polymorphs, **(c)** cubic (F$m3m$), **(t)** tetragonal (P4$_2$/nmc), **(m)** monoclinic (P2$_1$/c). Zr^{4+} cations are indicated by red, O^{2-} anions by blue spheres. Adapted and reprinted with permission from reference [68].

Table 3: Lattice parameters of common zirconia crystal phases. The tetragonal and cubic phases correspond to yttria- and magnesia-stabilized zirconia, respectively. Z denotes the stoichiometry, i.e., the number of ZrO$_2$ formula units per unit cell.[69]

phase	space group	lattice constants / Å				unit cell volume / Å^3
		a	b	c	β	
monoclinic	P2$_1$/c	5.15	5.21	5.32	99.2	140.9 (Z=4)
tetragonal	P4$_2$/nmc	3.61	-	5.18	-	67.3 (Z=2)
cubic	F$m3m$	5.09	-	-	-	131.6 (Z=4)

This is predominantly caused by two effects: phase transformation and grain growth. These two phenomena will be addressed in the following paragraphs.

3.2.1   Crystal Structure and Phase Transformations

Crystalline zirconia typically exhibits one of three polymorphs, i.e., cubic (c), tetragonal (t), or monoclinic (m), as illustrated in Figure 5. Details of the crystal structures are summarized in Table 3. At ambient pressure, the favorable modification is determined by the temperature. At low temperatures (below ∼1200 °C) the monoclinic phase is preferred, at intermediate temperatures (between ∼1200 °C and ∼2400 °C) the tetragonal phase is the most stable one, while the cubic phase is favored at high temperatures until melting occurs (above ∼2700 °C).[56,61,68] For the use as a structural ceramic, the martensitic (i.e., diffusionless) t→m phase transformation is particularly problematic, since it is accompanied by a 8 to 16 % shear strain and a 3 to 5 % volume expansion.[56,68,70] In high temperature environments, this usually causes stress-induced disintegration, which eventually leads to material failure. To overcome the drawback of
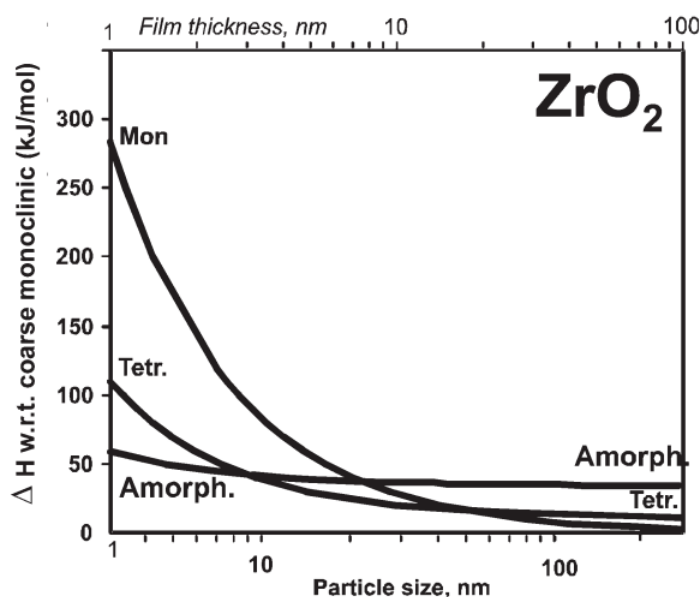
Figure 6: Enthalpy crossovers in zirconia. Excess enthalpy ΔH of nanophase zirconia with respect to (w.r.t.) coarse monoclinic zirconia, as a function of the particle (grain) size for amorphous, tetragonal and monoclinic zirconia, determined by high temperature oxide melt solution calorimetry. Energy crossovers in the nanometer region result in a stability reversal of the monoclinic and tetragonal phases compared to coarse-grained zirconia. Reprinted with permission from reference [71].

the destructive phase transformation, various ways of stabilization have been developed and some are widely used today. These concepts will be addressed in more detail later in this chapter.

The crystal phase behavior discussed above describes the situation in bulk zirconia. However, when dealing with nanostructured zirconia, another effect comes into play, namely the size effect. Recent calorimetric studies have found that the grain size of nanocrystalline zirconia has a large impact on the thermodynamically preferred crystal phase due to differing phase-specific surface energies.[71,77] By comparing excess enthalpies of amorphous, tetragonal and monoclinic zirconia of varying grain sizes, it was shown that the surface enthalpies of the three modifications have crossovers depending on the grain size, as shown in Figure 6. Therefore, fine-grained zirconia with an average grain size below ∼9 nm is most stable in the amorphous form, while the tetragonal modification is most stable at average grain sizes between ∼9 nm and ∼50 nm. For coarse-grained zirconia with grain sizes above ∼50 nm, the monoclinic phase is most stable at room temperature, which is in agreement with the observations made for bulk zirconia. To date, several numbers were suggested for the critical grain size, in other words, the grain size below which the tetragonal phase is more stable than the monoclinic phase at room temperature, as shown in Table 4. However, it

Table 4: Literature values for the critical grain size of zirconia. The critical grain size in zirconia denotes the specific grain size below which it is more stable in the tetragonal than the monoclinic phase at room temperature. Different experimental methods were used for the fabrication and the size determination.

authors	critical grain size
Bailey et al.[72]	9.7 nm
Mitsuhashi et al.[73]	10 nm
Garvie et al.[74]	10 nm
Chraska et al.[75]	18 nm
Shukla et al.[76]	15 to 45 nm
Navrotski et al.[71]	∼50 nm

should be noted that these values were obtained by different analytic methods and are based on samples prepared using various approaches. Although the correct value for the critical grain size is still subject to discussion, there seems to be a consent that a threshold exists in the low nanometer regime. Below this threshold, nanosized zirconia is stabilized in the tetragonal phase at ambient conditions.

In practice, crystal structures are routinely investigated using X-ray diffraction (XRD). In the context of nanocrystalline materials, it is worthwhile considering some aspects affecting the characterization via XRD. In nanosized domains, intense line broadening occurs due to the limited number of crystal planes and incomplete destructive interference at off-Bragg angles. This results in an overall lower signal-to-noise ratio, thus compromising the quality of the obtained data. It becomes particularly problematic when the differentiation of neighboring signals is required. In the case of zirconia, this affects especially the distinction between the tetragonal and cubic phases due to the high similarity of their lattice constants, as shown in Table 3. However, as discussed earlier in this section, the phase change that is mostly responsible for material failure is the t→m transition. It was therefore found sufficient for the purpose of the studies in this dissertation to consider tetragonal and cubic as one phase in the characterization and focus on its interplay with the monoclinic phase. Besides this difficulty, the size-induced line broadening can be advantageous in terms of additional information, namely the crystallite size. This value can be extracted from the XRD data, using either the Scherrer equation or the Rietveld method,[78,79] and used to investigate the effect of grain coarsening or grain growth, which will be addressed in the following.
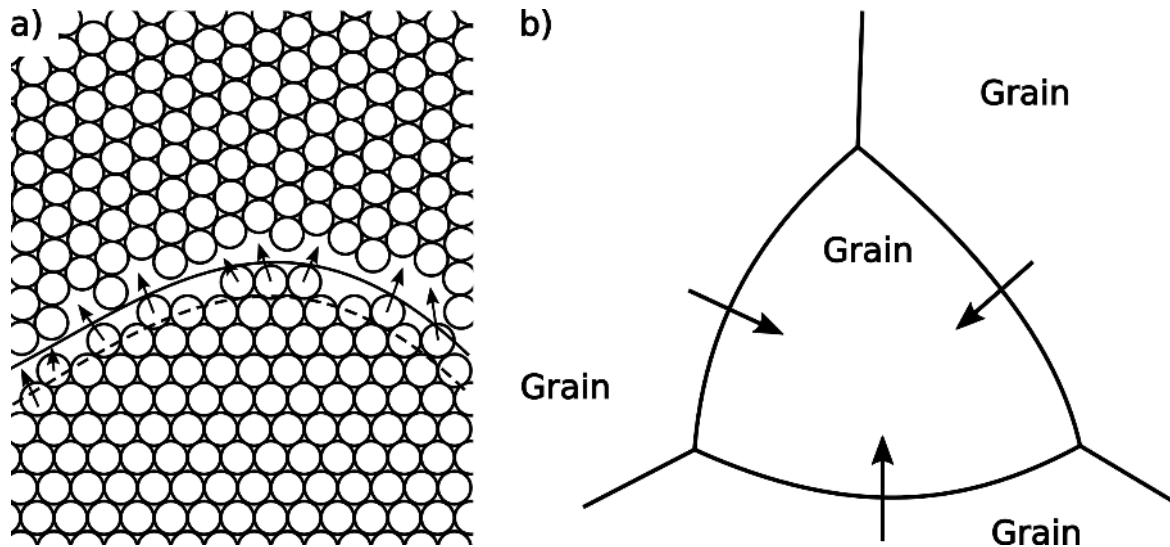
Figure 7: Grain growth. Schematic illustration of grain boundary migration in a two-dimensional polycrystalline material. **a)** The grain boundary moves by rearrangement of individual interface atoms. **b)** The migration is usually directed towards the center of curvature. Adapted and reprinted with permission from reference [80].

3.2.2   Grain Growth

From an engineering perspective, one of the most interesting properties of zirconia is its microstructure. Much like metals, ceramic materials often consist of a large number of grains, separated by grain-grain interfaces, commonly referred to as grain boundaries. At high temperatures, sintering occurs, which is often accompanied by coarsening of the microstructure.[80] Specifically, the average grain size increases as the overall number of grains decreases. This phenomenon is known as *grain growth* or *grain coarsening*. The change in grain size is the result of the migration of individual grain boundaries through the material. On the atomic scale, it can be considered as a successive reorientation of interface atoms from the crystal constellation of a shrinking grain to that of a neighboring growing grain. This mechanism is illustrated in Figure 7. As a result, the grain boundary is displaced in the opposite direction of the atomic movement. Grain boundary migration usually occurs towards the center of curvature.[80] The driving force behind this mechanism is the minimization of the total area of grain-grain interfaces. Since boundary atoms have a higher energy than inner atoms, this minimization consequently reduces the free energy of the material. The theoretical grain boundary mobility M is a temperature-dependent entity and can be

approximated by:[81]

$$M = \frac{D\Omega}{\delta k_B T}, \qquad \text{with} \qquad D = D_0 \exp\left(-\frac{E_A}{k_B T}\right) \tag{1}$$

In this equation, D is the grain boundary diffusion coefficient, Ω is the atomic volume, δ is the grain boundary thickness, k_B is the Boltzmann constant, and T is the absolute temperature. In the Arrhenius term, D_0 denotes a pre-exponential factor and E_A is the activation energy. From this model, it becomes clear that the mobility of grain boundaries is positively correlated with the temperature, hence grain growth is increasingly observed at higher temperature. However, pores, solutes, and inclusions have a significant impact on the grain boundary mobility, too.[81]

3.2.3   Doping and Mixed Oxides

The two effects discussed above, i.e., phase transformation and grain growth, render bare zirconia unsuitable for many high temperature applications. Therefore, potential ways of structural stabilization have been a matter of intensive research. In this context, the addition of specific other metal oxides in small amounts, often referred to as *doping*, has proven to be very effective. The most prominent example is yttria-stabilized zirconia (YSZ). Here, a significant amount of yttrium oxide (yttria, Y_2O_3), usually in the range of 4 to 18 mol% $\left((YO_{1.5})_x(ZrO_2)_{1-x}\right)$, is incorporated in the parent zirconia structure, affecting not only the stability of crystal phases but also other properties, e.g., ionic and electrical conductivity.[54,71,82] Depending on the yttria amount, the high temperature tetragonal or cubic phase is stabilized at otherwise untypically low temperatures, thus preventing the destructive transformation to the monoclinic phase during thermal cycling.

On the atomic level, some Zr^{4+} ions are replaced by the slightly larger Y^{3+} ions, as illustrated in Figure 8. Due to the lower valence of the yttrium ion, one oxygen vacancy is created for every two zirconium ions replaced, in order to maintain electroneutrality. Both foreign ions and oxygen vacancies have a significant impact on the surroundings of neighboring atoms in the crystal structure. However, a number of studies suggest that the lattice distortions caused by oxygen vacancies play a larger role in the stabilization of high temperature tetragonal and cubic phases than the dopant ions.[83–85] The YSZ phase diagram in Figure 9 provides a good overview of the phase compositions as a function of temperature and yttria content. It shows that an yttria fraction of $\sim$3 mol% or higher stabilizes the tetragonal or cubic phase at least partially at lower temperatures, while an yttria fraction of $\sim$18 mol% or higher fully stabilizes the cubic
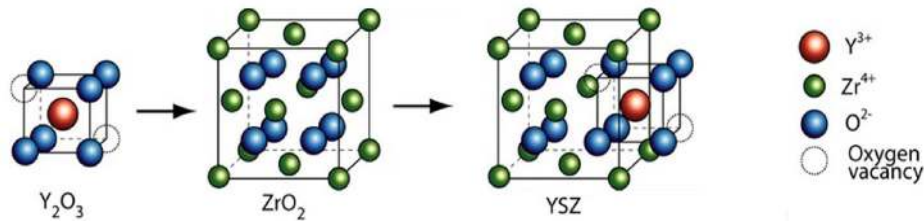
Figure 8: Schematics of oxygen vacancy formation in cubic YSZ. The difference in valence between yttrium and zirconium creates oxygen vacancies, which affect the phase stability of the parent zirconia lattice. Reprinted with permission from reference [87].

phase at all temperatures. Albeit full phase stabilization is generally desirable, higher amounts of yttria lead to various drawbacks, e.g., higher ionic conductivity and mass transport.[53,86] The latter particularly facilitates grain growth, an unfavorable effect as explained in the previous section.

Although zirconia possesses an appreciable solubility for yttrium and several other cations, segregation of the solute upon annealing occurs to some extent.[89,90] This phenomenon has been observed in several ceramic oxides and is commonly explained by the so-called space charge theory, which was earlier demonstrated for alkali halides.[91–93] It is argued that small defects in ionic crystals cause a spatial separation of charges. In thermally equilibrated polycrystalline zirconia, oxygen vacancies are predominantly found at the grain boundaries due to a lower formation energy of anion than of cation vacancies.[94] These defects create a net positive charge, which promotes the formation of zirconium vacancies in close proximity for reasons of electroneutrality. This region is considered a negative space charge cloud surrounding the (positively charged) grain boundary. Hence, positively charged dopant ions are drawn towards the surface of the crystallite, i.e., the grain boundary in a polycrystal. When grain growth occurs during annealing, these solute ions need to be dragged along with the migrating grain boundary, which effectively impedes its progression. This phenomenon is commonly called *solute drag effect*. The ability of a dopant to attenuate grain growth depends on its charge and ionic radius. Studies have shown that those with larger ionic radii and lower charge are more effective inhibitors in zirconia.[89,95] The aforementioned dopant segregation creates domains with high and domains with low dopant concentrations. This ultimately results in the formation of phase mixtures, as also indicated in Figure 9. Beyond YSZ, several other zirconia-based mixed oxides have been proposed, fabricated, and investigated over the past decades. The zirconia-alumina binary system is one example, combining two basic ceramics in a composite material. Alumina, most commonly present in the α-Al_2O_3 modification, is widely used for various applications,
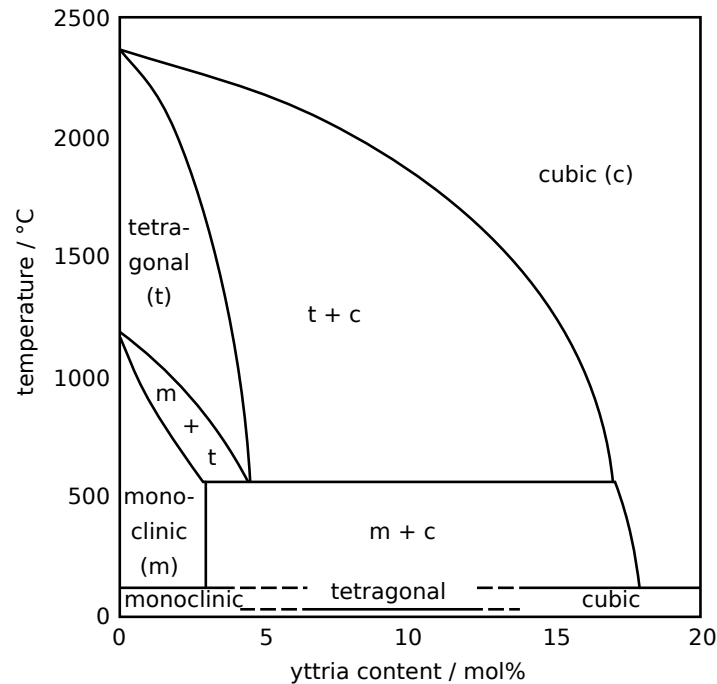
Figure 9: YSZ equilibrium phase diagram. Already small yttria contents stabilize the tetragonal and cubic phases at lower temperature. Adapted and reprinted with permission from reference [88].

e.g., refractories, abrasives, insulators, household ceramics, and catalyst materials. Growing interest in zirconia-alumina composites was initiated by the first significant insights reported by Claussen et al.,[96] who found an increased fracture toughness for alumina containing 15 vol% of unstabilized zirconia particles. They observed that the particles provoke microcracks during the t→m phase transformation, thus limiting the propagation of large cracks inside the composite material. Similar effects were observed for multiphase bare zirconia.[97] In the following years, Lange contributed significantly to the understanding of the strengthening effect of alumina in multi-component ceramic materials with his proposed model of *transformation toughening*.[70] He postulated that alloying oxides lower the martensitic phase transformation temperature and cause a preservation of the tetragonal phase by spatial constraint of the crystalline domains via one of two ways: a) In a single-phase polycrystal, neighboring grains with different orientations constrain the anisotropic strain of one another; b) The transforming phase is constrained by a second-phase matrix. Furthermore, microcracking and twinning would compensate strain caused by the transformation. These theoretical considerations were experimentally demonstrated for alumina-YSZ composites with varying compositions, showing significant toughening when t-ZrO_2 is present.[98] The author showed that alumina stabilizes the tetragonal zirconia phase in yttria-stabilized

as well as in undoped zirconia, and that a constraining alumina matrix increases the critical grain size due to the higher elastic modulus. Similar observations were made by Tsukuma et al.[99] who investigated the bending strength and fracture toughness of hot-pressed alumina-YSZ ceramics with varying alumina and yttria content. They found that alumina additions effectively strengthened the YSZ ceramics with a maximum bending strength at 20 vol% alumina, virtually independent of the yttria content. The effect was assumed to be due to reduced crack initiation. A microstructural study by Rajendran et al.[100] examining the effect of alumina addition on the microstructure and grain boundary resistivity of hot-pressed bulk YSZ revealed that the stress-induced t→m transformation is attenuated with increasing alumina content. Furthermore, it was observed that the average grain size of the sintered specimens decreased from 0 wt% to 30 wt% alumina. In agreement with other studies, improved fracture strength was observed for these materials in a later work.[101]

The materials in the aforementioned studies were predominantly composite ceramics consisting of two or more distinguishable components, e.g., zirconia and alumina. In thermodynamic equilibrium, alumina is hardly soluble in zirconia as recent studies have shown: Stough et al.[102] examined the solid solubility of alumina in cubic YSZ single crystals and found values as low as 0.2 to 0.3 wt% at 1200 to 1600 °C. Chraska et al.[103] prepared alumina-zirconia coatings by plasma-spray and obtained supersaturated solid solutions with large variations in chemical composition. Upon short annealing they observed crystallization of very small (∼13 nm) crystallites embedded in a fine inter-crystallite network, suggesting phase separation due to insolubility. An equilibrium phase diagram for the zirconia-alumina system is shown in Figure 10. Here, the mutual solubility in equilibrium is limited to a narrow region with compositions containing only very small alumina fractions. However, metastable (supersaturated) versions of solid solutions comparable to YSZ have been reported. Ishida et al.[104] produced hot-pressed bulk ZrO_2-Al_2O_3 solid solutions with alumina contents of up to 40 mol% from chloride precursors and examined their microstructural and mechanical properties. They found that the cubic and tetragonal phases were increasingly stabilized by alumina addition, while the m-ZrO_2 grain size decreased significantly. Furthermore, α-alumina crystallized at temperatures above 1200 °C due to phase decomposition and mesosized inter-grain α-alumina domains were observed. Nazeri et al.[105] were the first to use the sol-gel method to synthesize zirconia-alumina thin films with alumina contents up to 38 mol%. The as-prepared amorphous solids containing 7 mol% alumina crystallized in the cubic phase upon annealing at ∼600 °C. Here again, the crystallite size decreased with increasing alumina content. The authors pointed out the insolubility
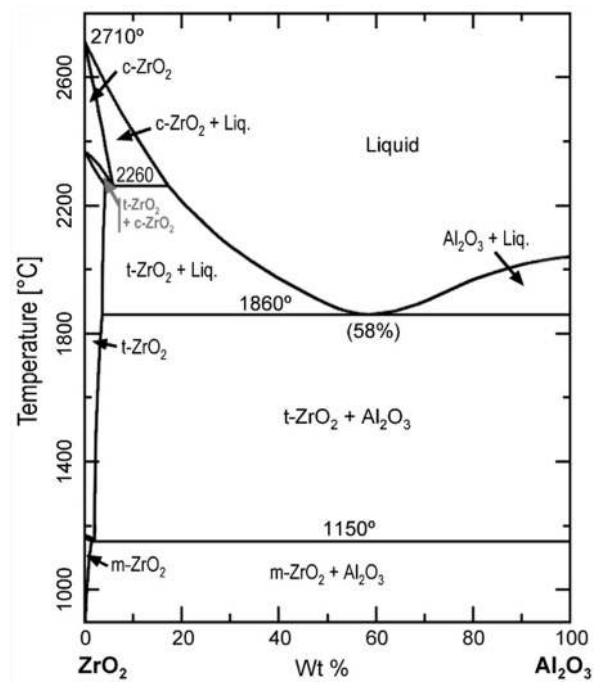
Figure 10: Zirconia-alumina equilibrium phase diagram. The two oxides are almost insoluble in thermodynamic equilibrium, only at very low alumina contents, stable solid solutions are formed. Adapted and reprinted with permission from reference [103].

of alumina in zirconia and argued that the stabilization is caused by the *constraint effect*, as proposed by Lange (see preceding paragraph). Similarly, Klimova et al.[106] prepared alumina-zirconia mixed oxides by a sol-gel method and obtained alumina containing well-dispersed zirconia. They showed that the presence of alumina delays the crystallization of zirconia upon calcination and that it stabilizes the tetragonal phase at low, and the cubic phase at higher mole fractions, also quoting the inclusion size effect proposed by Lange.

Srdić et al.[107] were able to fabricate alumina-doped nanocrystalline zirconia, i.e., solid solutions of thermodynamically insoluble phases, by chemical vapor synthesis. During calcination they observed segregation on an ultrafine scale and found that Al atoms are randomly distributed at lower alumina contents. On the contrary, small alumina clusters formed at higher molar ratios, which suppressed grain growth more effectively. They consequently proposed a microstructural model for different grain growth mechanisms, depending on the level of alumina doping and the current stage of sintering, as schematically illustrated in Figure 11. In all cases, the porosity of as-prepared samples is reduced during the early stage of sintering by particle rearrangement. In pure zirconia, grains grow unimpededly by atom propagation along
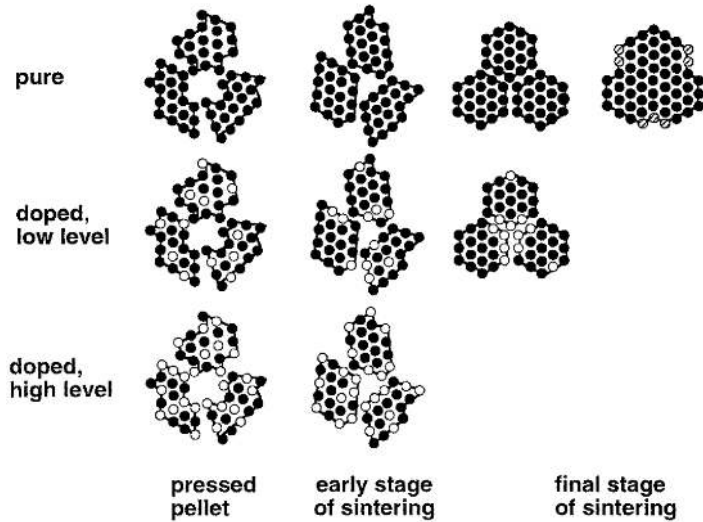
Figure 11: Model for sintering of alumina-doped zirconia. Schematic illustration of a microstructural sintering model for high-, low-level alumina-doped, and pure nanocrystalline zirconia. Grain boundaries are represented by lines, solid and open circles indicate Zr and Al atoms, respectively. Crosshatched circles represent Zr atoms that have moved along the grain boundaries. Reprinted with permission from reference [107].

the grain boundaries during the late stage of sintering. When doped with small amounts of alumina, Al atoms move towards the particle interfaces during the early stage where they subsequently limit grain growth during the final stage of sintering. When doped with larger amounts of alumina, the grain surfaces of the as-prepared material already have an alumina similarity, which is further amplified by segregation in the early stage of sintering. Here, the mobility of atoms in the now alumina-dominated grain interfaces is very low. Therefore, grain growth is mostly suppressed and a fine-grained porous material is retained. The model is based on considerations by Balmer et al.,[108] who investigated zirconia-alumina composites prepared by spray pyrolysis using ^{27}Al nuclear magnetic resonance spectroscopy. The metastable crystalline materials contained 8 to 57 mol% $AlO_{1.5}$ and the aluminum ions had 4-, 5-, and 6-fold coordinations. The authors concluded that larger alumina clusters than expected had formed, based on the increasing fractions of low-coordinated Al^{3+} ions they observed. Therefore, it was reasoned that random solid solutions form at low alumina contents (≤ 10 mol%), whereas aluminum-rich clusters dominate at higher alumina contents. Alumina accumulation upon sintering was also observed for polycrystalline YSZ doped with small amounts of alumina by Matsui et al.,[109] who found segregated Al^{3+} and Y^{3+} ions at the grain boundaries in $\sim$6 nm and $\sim$10 nm wide areas, respectively. While the alumina addition accelerated sintering significantly, it also enhanced grain growth at temperatures above

1500 °C and increased the cubic phase fraction compared to pure YSZ.

Recently, zirconia-alumina composites have also been studied in the context of TBC applications. Keyvani et al.[110] plasma-sprayed alumina-doped YSZ on typical Ni-superalloy substrates, both blank and precoated with a conventional YSZ TBC and investigated their cyclic oxidation behavior. For both systems, an improved durability towards oxidation at 1100 °C was obtained, presumably by attenuating the oxygen diffusion. Zhu et al.[111] compared alumina-YSZ and a conventional YSZ TBC with respect to their microstructure and oxidation behavior. They concluded that the addition of alumina can cause partial sealing of surface cracks in YSZ coatings and promotes the stabilization of the metastable tetragonal zirconia phase during oxidation.

3.3   Zirconia Meso- and Microparticles

The fabrication of particulate zirconia has received noticeable attention in the scientific community for quite some time. In the early stages, researchers were interested in fine-grained ceramics due to improved sintering characteristics for engineering applications.[112–114] However, with a considerably increasing relevance of nano- and micrometer-sized ceramic particles for modern materials design, the number of scientific studies on zirconia particle synthesis has risen significantly over the past three decades.[115] Meanwhile, various approaches of nano- and microparticle synthesis have been reported. In early works by Matijević et al., the synthesis of micrometer-sized zirconia spheres by simple ageing of a $Zr(SO_4)_4$ solution at elevated temperature was achieved.[116,117] This laid the foundation for several studies based on zirconia powder syntheses using salts as precursors.[118–124] Several years later, more complex methods have been proposed, such as spray pyrolysis,[125,126] solvothermal,[127,128] and template-based methods.[129–133] However, one of the most promising and probably most intensely studied approaches is the sol-gel synthesis. In the context of this dissertation, the sol-gel method is the most relevant one and will therefore be covered in more detail in the following section.

3.3.1   The Sol-Gel Synthesis

The fabrication of spherical ceramic particles by the sol-gel approach was first reported for SiO_2 in a widely renowned pioneer study by Stöber et al.[134] half a century ago. It was subsequently adapted and transferred to various metal oxides, e.g., TiO_2[135] and ZrO_2.[114] The rather simple chemistry behind it is illustrated in Figure 12 for the synthesis of zirconia via the sol-gel route. Here, zirconia alkoxides serve as precursors
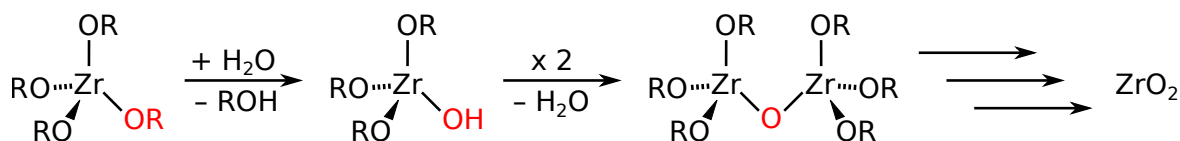
Figure 12: Reaction scheme for the zirconia synthesis via the sol-gel route. First, a zirconium alkoxide precursor is hydrolyzed by water, replacing one or several alkoxide ligands by hydroxyl groups. Second, two hydrolyzed precursor molecules condensate, releasing a water (or alcohol) molecule. Multiple repetitions of this hydrolysis and polycondensation result in the formation of a growing zirconia network.

and react with water in an alcoholic solvent at slightly elevated temperatures. In a first step, one or several alkoxide ligands are hydrolyzed and replaced by a hydroxyl group. In a second step, two hydrolyzed precursor molecules undergo a condensation reaction releasing a water or alcohol molecule. Here, a Zr–O–Zr bridge is formed, which represents a subunit of the final oxide. The latter is ultimately obtained by repeated hydrolysis and polycondensation. Although this basic mechanism suggests otherwise, sol-gel is a complicated technique. It is very sensitive to reaction conditions, reagent concentrations, and the presence of additional substances. Conversely, a variety of microscopic architectures can be achieved, including macromolecular networks and gels, as well as defined particles of various size and shape. Particle growth by sol-gel is particularly challenging and remained little understood until the first works of Fegley et al.[114,136] initiated a series of investigative studies into this method. They reported the first sol-gel approaches for ZrO_2, SiO_2, TiO_2, and Al_2O_3 mesosized powders, i.e. with a particle sizes in-between the nano- and micro-regimes, as well as improvements to the original protocol, yielding spherical, non-agglomerated mesoparticles. Only one year later, a study by Uchiyama et al.[137] demonstrated the synthesis of YSZ particles by a similar route and evaluated the effects of reaction conditions, e.g., ageing time, temperature, and water concentration, on the particle morphology. They also suggested that the duration, until the solution becomes turbid after initiation of the reaction, is an adequate measure for the precipitation rate. This value has by now been widely accepted as a semi-quantitative indicator for the hydrolysis rate and is commonly called *induction time*. In a comprehensive study on the growth mechanism by Ogihara et al.[138] it was concluded that the particle growth proceeds via a primary particle nucleation step followed by polynuclear LaMer-type growth of individual particles.[139] Although this theory was strengthened by other studies,[140,141] Ogihara et al. also considered an alternative growth mechanism by agglomeration of primary particles, as schematically illustrated in Figure 13. This assumption was later also shared by Lee et al.[142] in the context of a salt-based particle synthesis.
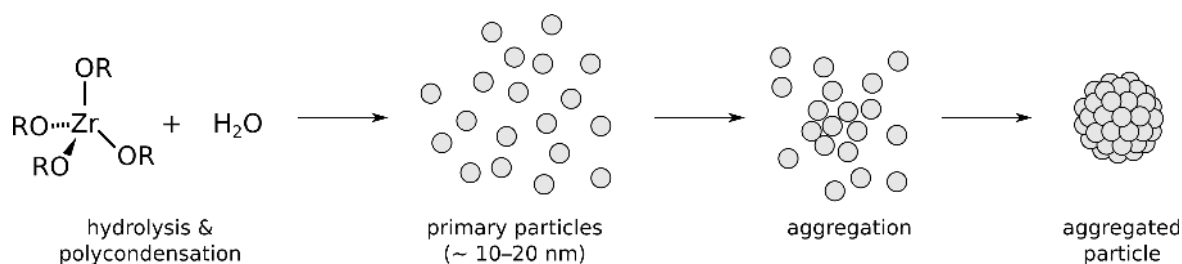
Figure 13: Zirconia particle growth by aggregation. Schematic illustration of a possible growth mechanism based on aggregation of small primary particles. Licensed under Creative Commons, adapted and reprinted from reference [143].

A significant improvement of the method was contributed by Lerot et al.[144] with the addition of carboxylic acids as stabilizing agents. By this means, a higher degree of control over the uniformity and size of the final particles was achieved. The authors conducted several experimental series with variations in the acid chain length and alcoholic solvent used. Based on their findings, they suggested that the carboxylic acids react with the zirconium alkoxide precursors to form carboxy-alkoxide derivatives and proposed the formation of micellar structures of these species as a tentative mechanistic explanation. They likewise postulated an aggregation-based mechanism for particle growth. In a mechanistic study, Van Cantfort et al.[145] considered a competition between the two mechanisms, i.e., LaMer-type and aggregation-based particle growth, based on their findings. The aggregation-based mechanism has since been discussed intensely in the literature. It has been the preferred model to explain the growth of sol-gel derived zirconia particles in more recent publications,[146,147] which also laid the foundation for today's state-of-the-art sol-gel synthesis of zirconia meso- and microparticles.

Yan et al.[146] reported the successful synthesis of submicron- and micron-sized monodisperse, spherical, and nonporous zirconia particles, stabilized by organic acids in anhydrous butanol. They investigated the influence of various experimental parameters, e.g., water concentration, acid chain length, ageing time, temperature, and extent of stirring, on the particle size, size distribution, and degree of aggregation. Specifically, they found that large particles with diameters of $\sim$4 μm were obtained by extended stirring and that gentle rotation during ageing prevented a bimodal size distribution caused by secondary nucleation. At about the same time, Widoniak et al.[147] reported a protocol for the fabrication of monodisperse spherical zirconia particles in the meso- and low micron size range. Herein, they used different alkali halide salts or polymers as stabilizers and varying alcoholic solvents. They concluded that the final particle size can be adjusted by addition of a suitable salt or polymer, although stabilization by
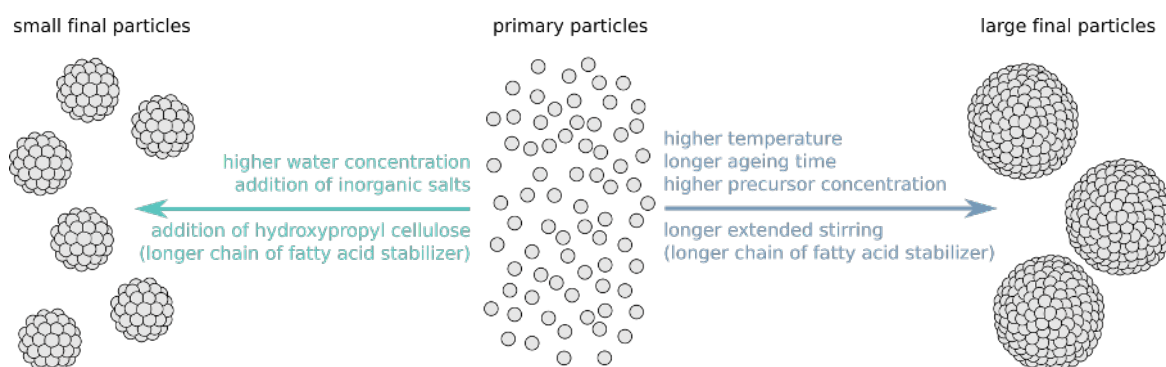
Figure 14: Impact of synthesis parameters on zirconia particle size. Various factors influence the final particle size in the sol-gel synthesis of zirconia particles, as reported in the literature. The aggregation of primary particles can be adjusted in favor of smaller (left) or larger (right) particles by choice of the stabilizer, addition of certain substances, or variation of the reaction conditions. For the fatty acid chain length, contradictory results have been reported. Adapted from references [94] and [23].

polymers seemed to result in broader size distributions. It was also found that higher water concentrations yielded smaller particles, while higher precursor concentrations yielded larger particles.

Very recently, further improvements of these methods were demonstrated by Leib et al.,[148] who studied in depth the effect of longer fatty acids, varying zirconia precursors, and different solvents on the particle morphology. Subsequently, their improved protocol was adapted for the synthesis of analogue YSZ particles for the potential use in high temperature applications.[8] Here, the authors observed shorter induction times compared to the synthesis of equivalent undoped zirconia particles, which they explained by a faster hydrolysis of the admixed yttria precursor due to its higher reactivity. It was argued that yttrium *iso*-propoxide possesses fewer organic ligands than zirconium *n*-propoxide and a more electronegative metal ion, both rendering it more reactive and susceptible to nucleophilic attacks. Overall, a significant number of studies have contributed to a general understanding of the synthesis parameters influencing the morphological characteristics of sol-gel derived zirconia meso- and microparticles. Most of the findings are in good agreement among different research groups, a selection of parameters and their effects on the particle size are summarized in Figure 14. The final particle diameter can be influenced by the variation of reaction parameters, e.g., reagent concentrations, temperature, and ageing time. Furthermore, the addition of large polymers, such as hydroxypropyl cellulose (HPC), can serve as a tool to reduce the particle size, as some studies on nanocrystalline ceramics by Jean and Ring have indicated.[149–151] Shukla et al.[152] argued that HPC adsorbs on the surface of primary nanoparticles providing steric hindrance of particle aggregation. Moon et

al.[123] also referred to Jean and Ring pointing out that HPC provides thermodynamic rather than kinetic stability, as in electrostatic stabilization, and that the polymer molecules do not act as heterogeneous nucleation sites. In their study, they showed that the employment of HPC can be used to reduce the size of spherical zirconia mesoparticles significantly, although the size distribution appeared to increase when exceeding a certain HPC concentration.

3.3.2   Thermal Stability and Particle Doping

The crystallization behavior of bulk zirconia under exposure to high temperatures was discussed in Section 3.2.1. In contrast, it was observed that fine-grained zirconia behaves differently. When synthesized at moderate temperatures, it is often obtained in an amorphous state.[76,123,144,147,148,153] Furthermore, several studies have shown that particulate zirconia tends to crystallize in the tetragonal[76,128,147,148,153] or cubic[128,144] phase first, before it transitions to the monoclinic phase during annealing at temperatures between 250 and 600 °C. The typical martensitic phase transformation of zirconia was observed after annealing at temperatures between 450 and 1000 °C, depending on the specific material and its preparation method. The anomaly of tetragonal crystallization at low temperatures was addressed by several groups: Garvie et al.[74,154,155] found in their studies that the amorphous zirconia exhibited an average grain size smaller than the critical grain size (see Table 4), which favored crystallization in the tetragonal phase due to lower overall grain boundary energy.[71] In some early works by Livage et al.[156] and Keramidas et al.[153] it was shown using XRD and/or Raman spectroscopy that the atomic arrangement in amorphous zirconia is not random but shows some characteristic similarity to the tetragonal crystal structure. However, Zhang et al.[157] argued that the local structure of amorphous zirconia resembles the short-range atomic order of cubic zirconia. These results suggest that the crystallization of the tetragonal (or cubic) phase from amorphous zirconia could be induced by the high similarity of the atomic arrangements. It has been discussed controversely in the literature, whether the subsequent martensitic phase transformation to the monoclinic polymorph occurs only during cooling or during heating and cooling,[158–161] although more recent results of extensive in situ experiments by Leib et al. favor the latter.[148]

For salt-based and sol-gel zirconia particle syntheses, several studies have reported a porosity of the as-prepared particles to some extent.[63,65,119,140,144,146] However, in most cases the particles densified completely or almost completely during annealing at temperatures between 450 and 750 °C.[63,144,146,148] This densification was also observed

in the form of significant particle shrinkage.[148] Comparative annealing experiments with zirconia particles of different sizes showed that larger particles are more stable against disintegration during annealing.[148] In the corresponding study, the grain size evolution as a function of the annealing temperature was also investigated. The authors found that lower crystallization temperatures led to smaller initial grain sizes and an improved thermal stability. As expected, a successive grain growth could be observed and monitored by electron microscopy, which was assumed to be partly responsible for particle disintegration.

In Section 3.2.3, high temperature stabilization of bulk zirconia by yttria-doping was discussed. Concerning the thermal stability of fine-grained zirconia particles, only a small number of publications existed until a few years ago, mainly dealing with particles in the nanometer scale.[127,152,162–164] For zirconia meso- and microparticles, Leib et al. were the first to report a comprehensive and systematic series of studies to gain an in-depth understanding of the effect of doping on the high temperature behavior.[8,148,165] Initially, the authors demonstrated a synthetic route to obtain monodisperse spherical YSZ particles with different sizes and compared their thermal stability against disintegration to that of similar-sized undoped zirconia particles.[148] They could show that the martensitic phase transformation was suppressed in the YSZ species and thus significantly smaller grains were observed by electron microscopy. Subsequently, a screening study was reported, investigating the thermal stability of YSZ particles as a function of the yttria content (0 to 18 mol%).[8] Here, it was found that the inhibition of grain growth and particle disintegration varied for different yttria-doping levels with an optimum stabilization effect for 8 to 10 mol% yttria. Furthermore, dopant segregation into Y-lean and Y-rich domains was observed after prolonged annealing. Finally, Leib et al. demonstrated a grain growth attenuating effect for zirconia and YSZ particles by La- and Gd-doping.[165] For La/Y- and Gd/Y-codoped particles, very high thermal stabilities up to 1200 °C were achieved.

While there has been little research on zirconia particles doped with other metal oxides,[166] no systematic experimental series on sol-gel derived alumina-doped zirconia particles has been published. The first study was therefore reported recently by our group,[143] which was conducted in the context of my doctorate studies.

3.4 Metal-Ceramic Composites

With recent progress in the field of nanoscience and colloidal synthesis, a growing number of studies have approached more complex material combinations and geome-

Figure 15: The Lycurgus cup. Ancient artifact from the late Roman period (approx. 4th century AD) in the British Museum. Fine gold and silver nanoparticles incorporated in the glassware create different color impressions for transmitted (left) and reflected (right) light due to surface plasmon resonance. Licensed under Creative Commons, reprinted from reference [173].

tries on the nanoscale. One example are metal-ceramic hybrid core@shell particles, consisting of a ceramic core particle and a surrounding metal nanoshell. They are of particular interest due to their unique and tunable optical and electronic properties. Therefore, they are considered with respect to a wide range of potential applications in various fields, e.g., biological imaging and therapy,[167,168] immunoassays,[169] surface enhanced spectroscopy,[170] optical metamaterials,[36] sensors,[170] fuel cells,[171] and catalysts.[170,172] Gold nanoshells (GNSs) are often obtained by using gold nanoparticles (GNPs) as seeding nuclei. Both nanomaterials exhibit some remarkable optical properties that differ strongly from those of bulk gold. In addition, metal-ceramic composites may be of considerable use to other disciplines, e.g., for catalytic applications. In this section, the unique optical properties of GNPs and GNSs, relevant synthetic approaches for both nanostructures, and prospects of metal-ceramic composite particles in catalysis will be reviewed.

3.4.1 Optical Properties of Nanosized Gold

Gold nanoparticles, and metal nanoparticles in general, have been used for centuries due to their unique optical properties, e.g. for the coloration of glassware, as archaeological findings like the Lycurgus cup (see Figure 15) impressively demonstrate. Their strong optical response in the visible spectral region is caused by a phenomenon called surface
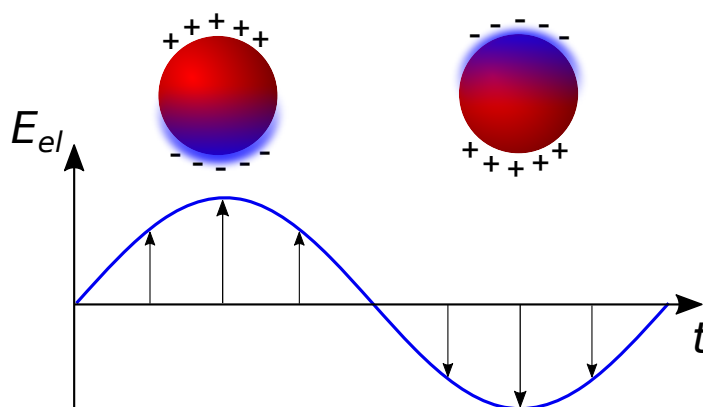
Figure 16: The Mie theory of surface plasmon resonance (SPR). The surface electrons in a metallic nanoparticle are excited to a collective oscillation by the alternating electric field of incident light in the visible range. The energy of this excitation for isolated particles depends on the particle size and shape. Reprinted from reference [174].

plasmon resonance (SPR). Here, conduction band electrons in nanometer-sized metallic particles collectively oscillate against the rigid atomic cores, as schematically illustrated in Figure 16. This can be described by the classical Mie theory.[175] The resonant frequency of the SPR, and hence its position in the electromagnetic spectrum, is – to some extent – sensitive to the particle size, dielectric environment, and the inter-particle distance. When particles grow or coalesce to form larger particles, a red-shift of the plasmon band is observed. A similar effect is caused by inter-particle SPR coupling, when particles are brought in very close proximity. Therefore, the characteristic SPR band in the absorption spectrum of visible light can provide valuable information about particle size, shape, and/or inter-particle distance.

Similarly to gold nanoparticles, gold nanoshells exhibit surface plasmon resonance when irradiated with light of its resonance frequency.[176] However, the different geometry of the metallic component results in strongly deviating optical properties. The SPR band position of solid metal nanoparticles can only be tuned in a very narrow spectral region by adjusting the particle size and shape. In contrast, the SPR energy of metal nanoshells is very sensitive to the inner and outer radius and can be tuned over a wide range across the entire visible and infrared regime.[177] This gives rise to the potential use of GNSs in advanced optical materials. For this purpose, however, a high degree of monodispersity and accurate control of the precise dimensions on the nanoscale are required.

3.4.2   Gold Nanoparticle and Nanoshell Synthesis

Over the past decades, several protocols have been proposed for the synthesis of spherical GNPs in the literature. Most of them are based on the reduction of gold salts in the presence of stabilizing agents to control colloidal growth and avoid coalescence. Brust et al.[178] and subsequently Leff et al.[179] demonstrated a two-phase synthesis of GNPs using sodium borohydride as reducing agent and tetraoctylammoniumbromide as phase transfer agent. Stabilization of the colloids is provided by an alkanethiol or alkaneamine, respectively, yielding particle sizes of 1 to 5 nm. A well-known method for GNP synthesis in an aqueous medium was previously reported by Turkevich et al.,[180] using sodium citrate as both reducing agent and stabilizing ligand. This procedure has since been adapted, optimized, and revised by many research groups.[181–184] Consequently, highly monodisperse particles of 9 to 120 nm in nanomolar concentrations can be obtained.[181] Particle sizes of up to 300 nm are accessible by a similar approach employing seeded growth.[185] Protocols for the synthesis of smaller gold colloids in aqueous solution were also reported,[186] though the obtained colloids are likely to consist of at least a fraction of gold sulfide rather than pure gold due to the use of thiocyanate. The method used in this dissertation originates from another work by Duff et al.[187] that yields very small hydrophilic spherical GNPs in the size range of 1 to 2 nm. Here, in a one-pot synthesis, tetrachloroauric(III) acid ($HAuCl_4$) is reduced by tetrakis(hydroxymethyl)phosphonium chloride (THPC) in an alkaline aqueous solution. THPC acts as both reducing agent and stabilizing ligand. Despite the relatively broad size distribution, particles of this small size are of significant interest for catalytic applications and as nucleation sites for nanoshell growth.[188,189]

In contrast to colloidal nanoparticles, gold nanoshells cannot be synthesized by spontaneous nucleation in solution and must be deposited on a supporting template. In the literature, various templates have been used, e.g., polyaniline nanocolumns,[191] polystyrene latex beads,[167] and silica nanospheres. The well-known Stöber method for the synthesis of highly monodisperse spherical silica meso- and microparticles has made this material by far the most popular nanoshell template.[134] Oldenburg et al. contributed to the increasing attention for gold nanoshells with their pioneering work on the controlled deposition of GNSs onto silica nanospheres,[189] using a multi-step procedure, as schematically illustrated in Figure 17.

Here, monodisperse silica spheres are fabricated by the Stöber method and surface-functionalized with amine groups. GNPs obtained by the Duff method are subsequently immobilized on the functionalized surface and serve as nucleation seeds for a gold
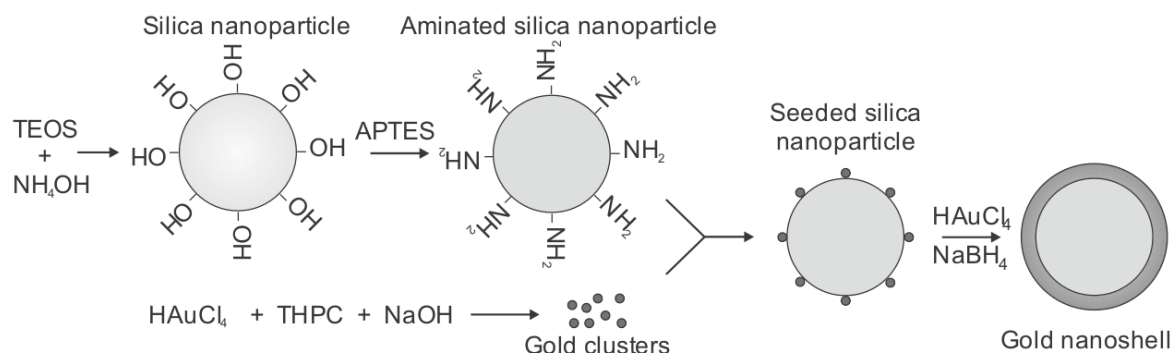
Figure 17: Gold nanoshell deposition onto silica nanospheres. Popular multi-step method by Oldenburg et al.[189] via immobilization of small gold nanoparticles onto surface-functionalized silica spheres and subsequent seed-mediated gold deposition by reduction. Tetraethyl orthosilicate (TEOS) and 3-aminopropyl triethoxysilane serve as silica precursors, while tetrakis(hydroxymethyl)phosphonium chloride (THPC) functions as reducing agent and stabilizing ligand. Reprinted with permission from reference [190].

nanoshell, which is grown by continuous reduction of ionic gold using sodium boro-hydride as reducing agent. It should be noted, that an aged mixture of chloroauric acid and potassium carbonate, often referred to as *K-gold*,[192] is used as the gold precursor. At the elevated pH caused by the carbonate, chloride ligands are exchanged by hydroxide ligands, ultimately forming the desired $[Au(OH)_4]^-$ complex. This species is known to have a lower tendency for secondary nucleation in solution than the chloride containing complexes $[AuCl_x(OH)_{4-x}]^-$.[190] Several groups have adapted this method by using other reducing agents, e.g., hydroxylamine,[193] formaldehyde,[169,194] sodium citrate,[195] hydrogen peroxide,[196] or carbon monoxide.[197,198] Ascorbic acid has also been employed recently as a reducing agent in a similar context, namely the deposition of platinum nanoshells.[198,199] Here, it enabled a good control over thickness and mor-phology of the growing shell, rendering it also a reducing agent worth contemplating for GNS deposition. Although less laborious and time-consuming synthesis protocols for GNSs have been proposed,[200–202] the multi-step syntheses based on the method by Oldenburg et al. remain the most reliable and commonly used methods, to date.

3.4.3 Zirconia-Gold Composite Preparation

While silica-gold composites have been studied primarily in the context of gold nano-shells, nanoscale combinations of gold with various metal oxides have attracted growing interest for its potential use as a catalyst material. This strategy is increasingly pursued, because the oxide supports can be easily obtained with a high specific surface area and are able to stabilize gold nanoparticles, thus maintaining their high surface to volume ratio.[203] Supported nanoparticulate gold catalysts show favorable activities at

relatively low temperatures $<100\,°C$ and are already used in sensing and air quality control.[204] Moreover, the interaction of dispersed GNPs and metal oxide support at the material interface can enhance the catalytic performance.[205] It was assumed that the gold-oxide interface activates at least one of the reactants involved,[204,206] although the mechanisms underlying this interaction are not yet fully understood.

In terms of synthesis routes, various approaches have been applied to deposit nanoscale gold onto oxide supports, e.g., co-precipitation, deposition precipitation, and immobilization of colloidal gold.[204,206] Precipitation techniques are facile and have been widely described in the literature for the loading of gold onto various support materials, e.g., titania,[207–210] alumina,[209] ceria and ceria/zirconia,[211–213] magnetite,[214–216] and several more.[206,214]

Furthermore, a number of research groups have recently focused on zirconia-supported dispersed gold for the catalysis of various reactions, e.g., the water-gas shift reaction, selective hydrogenation and dehydrogenation, and various oxidation reactions.[217–221] Idakiev et al. reported the synthesis of nanosized gold on a mesoporous zirconia support by deposition-precipitation.[217] Independently, He et al. and Menegazzo et al. followed similar approaches, but using nanoparticulate zirconia as a support.[218,219] Significantly smaller gold nanoclusters supported on multi-phase porous zirconia were prepared by Bi et al., who additionally showed that the zirconia crystal phase had a significant impact on the catalytic behavior.[220,221] Although the deposition precipitation is by far the most commonly used method, loading of dispersed gold was also achieved by the immobilization of previously prepared GNPs on various ceramic supports, e.g., titania, alumina, and zirconia.[222] Despite higher costs and efforts, this technique offers some attractive advantages over the more common methods, in particular a controlled GNP size, independent of the support material.

The studies presented above demonstrate the fabrication of various oxide-supported dispersed gold composite materials. However, none of the respective materials have a uniform and adjustable support morphology, nor a defined homogeneity and surface coverage of the gold loading. This is a plausible consequence of the deposition precipitation method which was used in most works, albeit the reported immobilization of GNPs yielded only slightly higher control over the product morphology. Although well-defined zirconia meso- and microparticles of varying sizes have been made widely available by intensive research progress in recent years, they have not been considered as gold catalyst supports so far. Nonetheless, they could be of substantial interest in this context for two reasons: firstly, particles of defined size and shape enable a facile and clean removal of the catalyst from the reaction mixture in liquid phase

reactors; secondly, they provide a well-defined morphology that is required in order to reliably study the characteristics of the fabrication process and the catalytic activity. Furthermore, GNP immobilization has not received much attention and the parameters affecting the success of this gold loading technique are yet unknown. In addition, no studies on the controlled growth of zirconia-supported GNPs by seeded reduction have been reported. Finally, monosized spherical zirconia particles homogeneously and densely covered with small GNPs are likely to be an appropriate starting material for the deposition of GNSs by seeded reduction to obtain zirconia@gold core@shell particles. A deeper understanding of these aspects can give rise to a set of synthetic tools for the precise design of novel catalytic or photonic functional materials and will be addressed in the course of this dissertation.

4   Objectives

The first part of this dissertation is dedicated to alumina-doped and alumina/yttria-codoped zirconia particles. the first objective was to synthesize alumina-doped zirconia mesoparticles and characterize their high temperature stability. Therefore, a known synthesis protocol for yttria-doped zirconia mesoparticles was adapted for the preparation of alumina-doped zirconia particles. Here, particles with varying alumina contents but similar size in the low submicron range were set to be fabricated. The samples were expected to show different behaviors when exposed to temperatures between 800 and 1200 °C with respect to changes in their morphology, micro-, and crystal structure. Thermal stability and integrity of the particle shape was of major concern for potential high temperature applications, such as high temperature resistive structural coloration. Second, a similar study was performed with the goal to synthesize and characterize alumina/yttria-codoped zirconia mesoparticles using an equivalent protocol and similar analytic methods. Here, the comparison with respective mono-doped species is of particular interest. Changes in the precursor composition are known to have a great impact on their preparation via the sol-gel particle synthesis. Therefore, the precise control over size, size distribution, and morphology of the final products were suspected to pose a major challenge.

In the second part, composite particle systems are of predominant interest. More precisely, core@shell particles with a ceramic core and a metallic shell were supposed to be synthesized. They were set to be characterized with respect to the accomplishment of a closed gold nanoshell with a homogeneous thickness. In a first study, the conventional material system silica@gold was chosen and the optimization of the synthesis by employment of an alternative reducing agent was explored. Moreover, the deposition of an outer silica shell and the investigation of the long-term stability of the shell morphology were aspects of particular interest. In a further study, the established protocol for the synthesis of gold nanoshells was adapted for their deposition onto zirconia mesoparticles, a method that has not yet been reported in the literature. Therefore, it was decided to use a particle sample from the first study (see previous paragraph) as starting material and to immobilize small GNPs on the particle surface. Here, the replacement of the coupling agent from the silica@gold synthesis with a suitable alternative is a key challenge. For this purpose, a novel approach based on chemisorption instead of covalent coupling was investigated. Finally, the reductive deposition of additional gold by seeded growth was pursued in order to establish a synthetic method for the synthesis of zirconia@gold core@shell particles.

5 Results and Discussion

In this chapter, the results of the experimental studies of this dissertation are presented and discussed. It is divided thematically into two parts, representing the different particle systems: On the one hand alumina- and alumina/yttria-doped zirconia particles (Sections 5.1 and 5.2), on the other hand metal-ceramic composite particles (Sections 5.3 and 5.4). Experimental details and further tabulated or illustrated data are provided in the Experimental Section, additional material can be found in the Appendix. It should be noted that dopant contents are consistently defined as molar cation contents, i.e. the molar fraction of dopant ions relative to the sum of all cations, for example $(AlO_{1.5})_x(ZrO_2)_{1-x}$ for alumina-doped zirconia, with x being the molar dopant fraction.

5.1 Alumina-Doped Zirconia Particles

As elaborated in detail in Section 3.2.3, the effect of alumina-doping in zirconia has only been studied sparsely compared to more common dopants, e.g., yttria. A number of studies have investigated the zirconia-alumina system as bulk material, however, no attention has yet been drawn towards the effect of alumina-doping in the particular case of sol-gel-derived zirconia meso- and microparticles. In this study, alumina-doped zirconia particles with average diameters of $\sim$300 nm were synthesized and characterized and their high temperature stability up to 1200 °C was examined. The results are presented here, whereby a major part of them were published recently.[143] The reported findings were mostly elaborated in collaboration with Mr. Sebastian Döring, whom I advised during my doctorate studies while he was conducting his master thesis project.[223] Herein, I provided the conceptualization and guidance of the study and was substantially involved in the sample preparation and characterization. I conducted the acquisition, curation, visualization, and interpretation of data as well as parts of the analytic characterization. The focused ion beam preparation and the energy-dispersive X-ray (EDX) spectroscopy mapping of selected samples were performed by Dr. Tobias Krekeler as part of the SFB 986 collaboration with the group of Dr. Martin Ritter at the Hamburg University of Technology (TUHH).

5.1.1 Particle Synthesis

Numerous synthetic approaches for the precise fabrication of monodisperse, spherical zirconia particles have been proposed in the literature. As discussed in Section 3.3.1, a large number of publications have contributed to the development of well-controllable
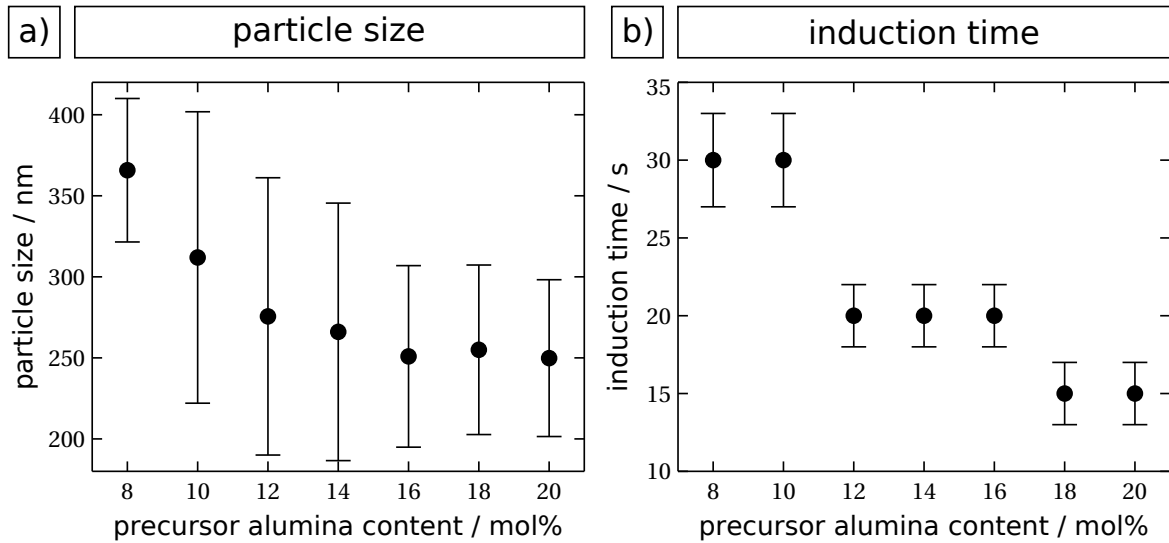
Figure 18: Characterization results for as-synthesized zirconia mesoparticles with varying alumina contents at otherwise identical synthesis conditions. (a) Average particle diameter as evaluated from TEM micrographs, error bars indicate standard deviations. (b) Observed induction times during syntheses, error bars indicate the determination uncertainties of the precise moment of induction.

preparation techniques for zirconia particles of varying sizes in the meso- and micrometer regime via the sol-gel route. Furthermore, doping of such particles with foreign metals, such as Y, La, and Gd, was achieved by co-precipitation of the equivalent precursors during the synthesis.[148] In this dissertation, previously developed approaches for the preparation of zirconia particles via the sol-gel route were adapted.[8,148,165] Analogously to the Y-, La-, and Gd-doping in these works, here, alumina-doping was achieved by using a precursor mixture of zirconium n-propoxide and aluminum iso-propoxide with varying molar ratios.

In a preliminary study, mesoparticles with alumina contents of 8 to 20 mol%, based on the precursor molar ratio, were synthesized at otherwise constant conditions. In contrast to previous protocols,[8,147,148,165] hydroxypropyl cellulose (HPC) was used in addition to eicosanoic acid to stabilize the growing particles. The purified samples were characterized using transmission electron microscopy (TEM) and the average particle diameters were determined statistically (for details see Section 8.2). In addition, the induction times were recorded by observing the onset of turbidity. The results are shown in Figure 18. In general, the use of HPC enabled the reduction of the final particle size compared to previous protocols to the low submicrometer regime due to the effects discussed in Section 3.3.1. With respect to increasing alumina contents in the precursor mixture, a decrease in both particle size and induction time is observed.

This indicates a higher hydrolysis rate which is attributed to the higher reactivity of aluminum *iso*-propoxide compared to zirconium *n*-propoxide, as similarly argued in a previous work for yttrium *iso*-propoxide.[8] Herein, the correlation is explained by a lower number of alcoholate ligands and less sterical hindrance compared to the zirconia precursor. In addition, one can argue that aluminum is a hard Lewis acid according to the concept of hard and soft acids and bases (HSAB). It is therefore expected to be more susceptible to a nucleophilic attack by a hard base during hydrolysis, in this case water.

It was recently shown that the thermal stability of zirconia particles depends significantly on the particle size,[148] whereby larger particles tend to have a higher stability. For a systematic investigation of the impact of alumina-doping on the high temperature stability of zirconia particles it is therefore crucial to use particles with similar size. In a subsequent series of experiments it was therefore intended to obtain similar-sized particles with varying amounts of alumina. Here, the strategy was to compensate the effect of the precursor reactivity on the particle size by variation of one or more synthesis parameters, as illustrated in Figure 14. More specific, the stabilizer composition (HPC/eicosanoic acid ratio) and the water content were adjusted to yield similar-sized particles with alumina contents ranging from 0 to $50 \, \text{mol}\%$ (samples are referred to as A0 to A50, with the number indicating the target alumina content). By this means, $(300 \pm 30) \, \text{nm}$ sized particles could be successfully fabricated, as determined by TEM and illustrated in Figure 19b. In addition, the samples were characterized by complementary analytic techniques, i.e., EDX (with TEM) and inductively-coupled plasma optical emission spectroscopy (ICP-OES). The characterization results for as-prepared particles are summarized in Table 5 and illustrated in Figure 19. A full set of transmission electron micrographs is provided in the Appendix (Figures 41, 42, and 43).

The elemental analysis clearly shows that the alumina content can be adjusted precisely by the molar ratio of the zirconia- and alumina-precursors in the reaction mixture (Figure 19a). While EDX was performed on random single particles, ICP-OES measurements represent an averaged value for a large number of particles. The results obtained with both methods show good agreement with the precursor molar ratio. This confirms, that the intended composition is achieved accurately on the one hand and homogeneously between several particles of the same sample on the other hand. Moreover, all samples could be prepared with a similar particle size of $\sim$300 nm and relative size distributions of 10 to 15 % (Figure 19b). This was achieved by varying the stabilizer composition and total stabilizer amount (Figure 19c). In particular, the
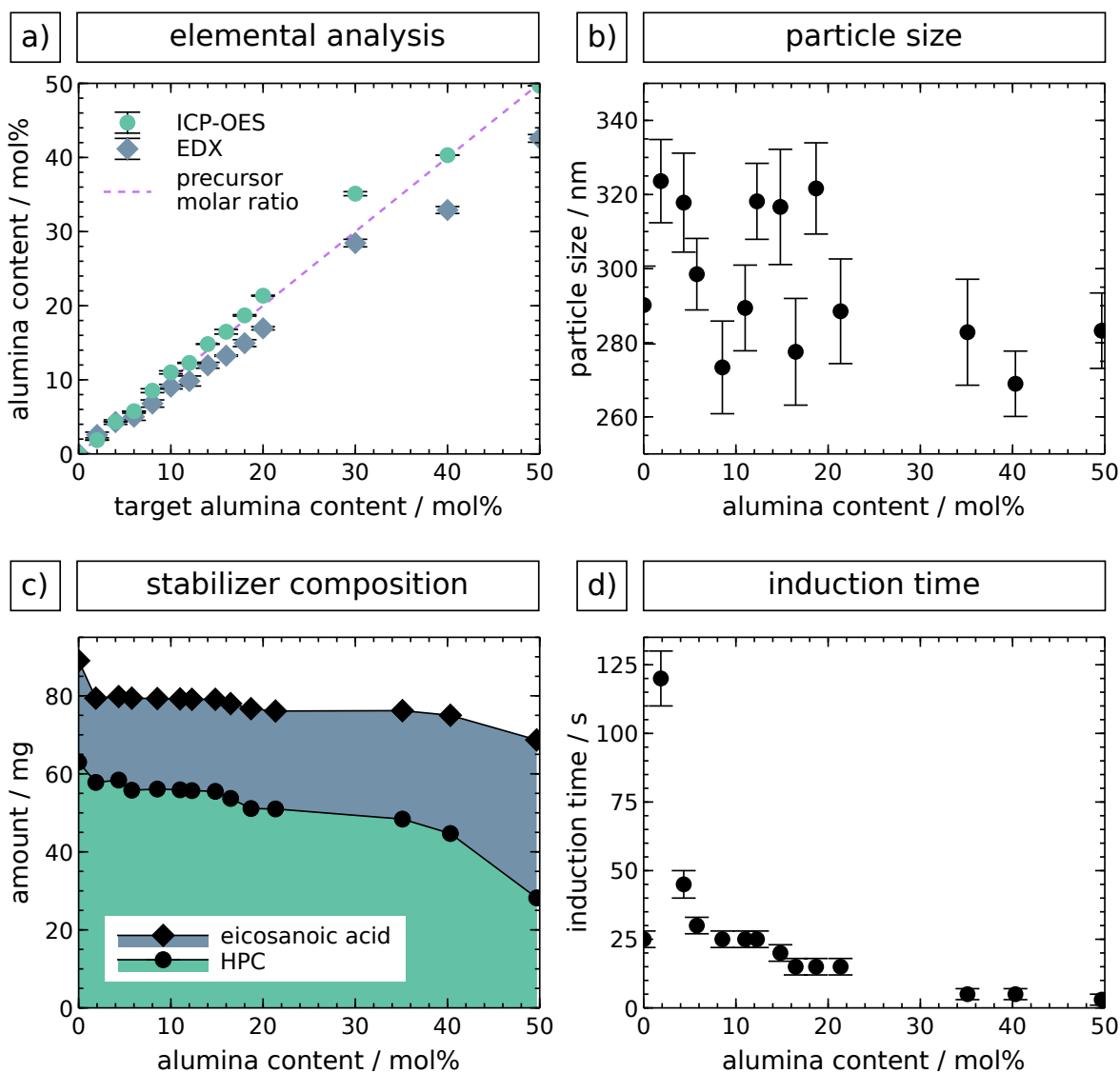
Figure 19: Characterization of as-synthesized zirconia particles with varying alumina contents. **(a)** Elemental analysis using EDX (with TEM) and ICP-OES. **(b)** Average particle diameter as evaluated from TEM micrographs. **(c)** Stabilizer composition, consisting of hydroxypropyl cellulose (HPC) and eicosanoic acid, per 45 mL solvent. **(d)** Observed induction times during the syntheses. Error bars represent standard deviations (a,b) and the determination uncertainties of the precise moment of induction (d). Licensed under Creative Commons, reprinted from reference [143].

Table 5: TEM, EDX, and ICP-OES characterization results for as-synthesized alumina-doped zirconia particles. The theoretical alumina contents are indicated by the sample names and correspond to the precursor molar ratios Al/(Zr+Al) used. Mean diameters were obtained from the specified number of particles n for each sample and calculated using the projection area of each particle. EDX data were obtained from individual particles, OES data represent averaged values for a large number of particles. Given uncertainties indicate the standard deviations of multiple measurements. Licensed under Creative Commons, reprinted from reference [143].

		TEM	EDX	OES
sample	n	d / nm	alumina content / mol%	
A0	114	290.2 ± 30.6 (10.5%)	-	-
A2	108	323.6 ± 36.3 (11.2%)	2.5 ± 0.38	1.86 ± 0.01
A4	157	317.8 ± 42.4 (13.4%)	4.2 ± 0.31	4.34 ± 0.04
A6	124	298.5 ± 28.8 (9.7%)	5.1 ± 0.48	5.76 ± 0.01
A8	112	278.9 ± 32.0 (11.5%)	6.8 ± 0.49	8.53 ± 0.26
A10	164	289.4 ± 33.4 (11.6%)	9.1 ± 0.31	11.00 ± 0.21
A12	109	318.3 ± 32.6 (10.3%)	10.1 ± 0.68	12.28 ± 0.06
A14	114	316.7 ± 49.2 (15.6%)	12.0 ± 0.39	14.82 ± 0.04
A16	117	277.6 ± 40.0 (14.4%)	14.4 ± 0.09	16.48 ± 0.31
A18	107	321.6 ± 39.6 (12.3%)	15.0 ± 0.47	18.69 ± 0.10
A20	127	288.5 ± 40.7 (14.1%)	16.9 ± 0.22	21.35 ± 0.06
A30	100	282.8 ± 40.5 (14.3%)	28.5 ± 0.51	35.11 ± 0.27
A40	124	268.9 ± 23.7 (8.8%)	33.1 ± 0.47	40.31 ± 0.02
A50	142	283.3 ± 28.9 (10.2%)	42.6 ± 0.52	49.67 ± 0.02
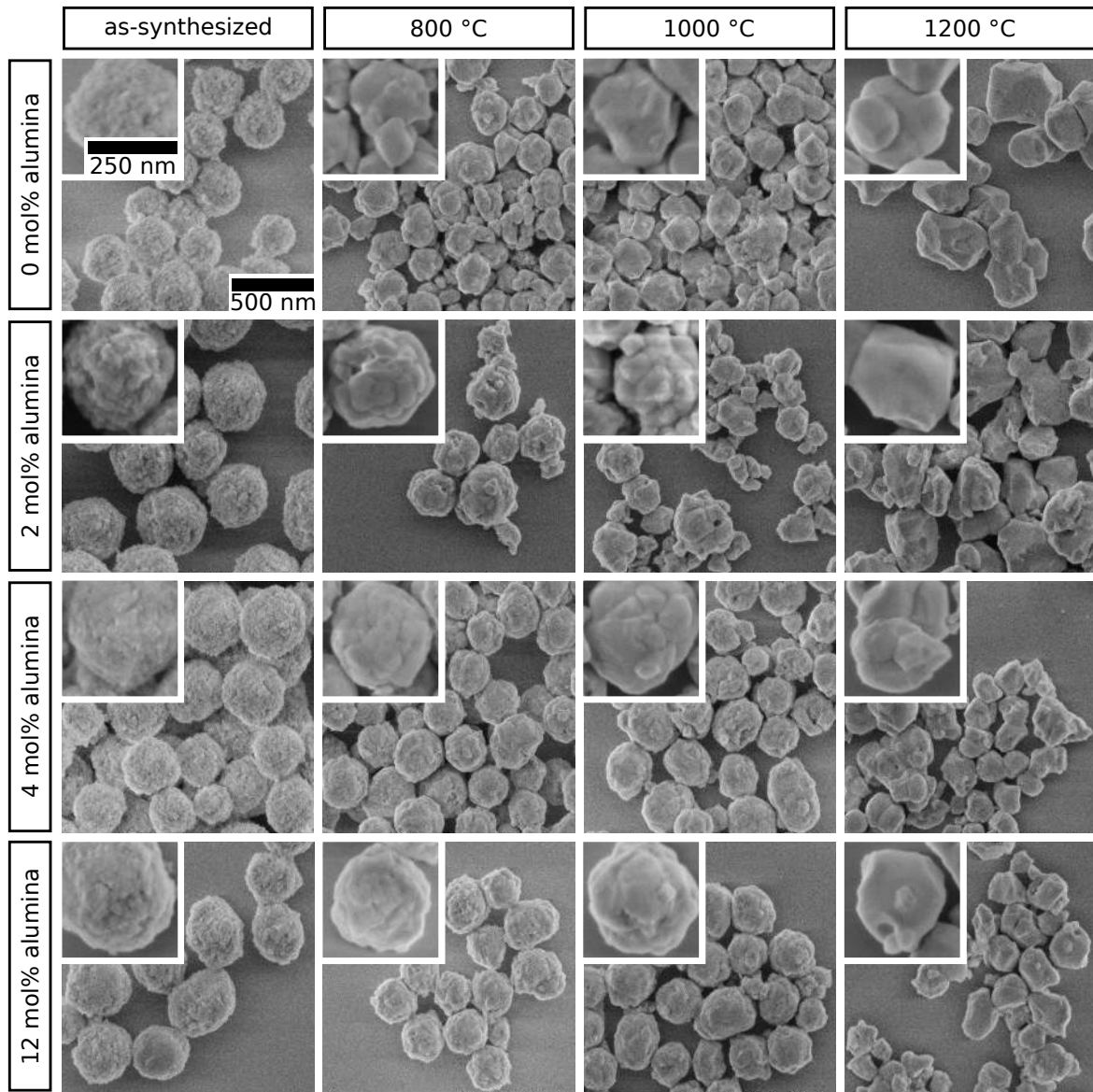
Figure 20: SEM analysis of selected alumina-doped zirconia particle samples. Representative micrographs of as-synthesized and annealed particle samples with different alumina contents are depicted. They show different degrees of structural disintegration after annealing at 800, 1000, and 1200 °C for 3 h. Higher alumina contents evidently stabilize the particles against thermally induced material failure. Licensed under Creative Commons, reprinted from reference [143].

amount of HPC was reduced with increasing alumina content in order to compensate for the size reducing effect caused by a larger alumina-precursor fraction in the reagent mixture. The induction times decreased drastically with increasing alumina content (Figure 19d). As discussed above, this can be attributed to the higher reactivity of the alumina precursor compared to that of the zirconia precursor.

5.1.2   Thermal Stability

In the next step, the thermal stability of the obtained particles was studied, i.e., the ability to maintain their size and spherical shape after annealing at high temperatures. This is particularly relevant with regard to their suitability for potential high temperature applications. Therefore, they were annealed at 800 °C, 1000 °C and 1200 °C for 3 h and subsequently characterized by TEM and SEM. TEM characterization was conducted for all samples. The results are provided in the Appendix (Figures 41, 42, and 43). Only selected samples were examined using SEM, representative micrographs are depicted in Figure 20. A qualitative comparison of the particle morphologies displayed here indicates a significant effect by alumina doping. The undoped particles already showed complete structural failure after annealing at 800 °C, while particles with only 2 mol% alumina had merely partly disintegrated. However, the samples with 4 mol% and 12 mol% alumina fully maintained their structural integrity after annealing at 800 °C. This is also observed after annealing at 1000 °C, although some grain coarsening occurred. In contrast, particles of all samples are mostly disintegrated after annealing at 1200 °C, independent of the alumina content.

X-ray diffraction (XRD) patterns were recorded for powder specimens of all annealed samples in order to gain insights into the crystal structures. The complete set of obtained diffractograms is provided in the Appendix (Figure 44), those for the selected samples are depicted in Figure 21. As reasoned in Section 3.2.1, the tetragonal and cubic crystal phases were considered as one phase in this work, hence referred to as 'tetragonal/cubic'. All observed peaks in the diffractograms correspond to either the monoclinic (m) or the tetragonal/cubic (t/c) zirconia phases, characteristic signals are marked accordingly. Peaks corresponding to crystalline alumina were not observed. This is suggests that the dopant is either present as a solid solute in the parent zirconia structure or in crystalline domains that are to small in size to cause detectable signals in XRD. The data show that the t/c phase is increasingly stabilized by higher alumina contents after annealing at 800 °C and 1000 °C. Material failure in zirconia at high temperatures is often caused by the destructive phase transformation from the
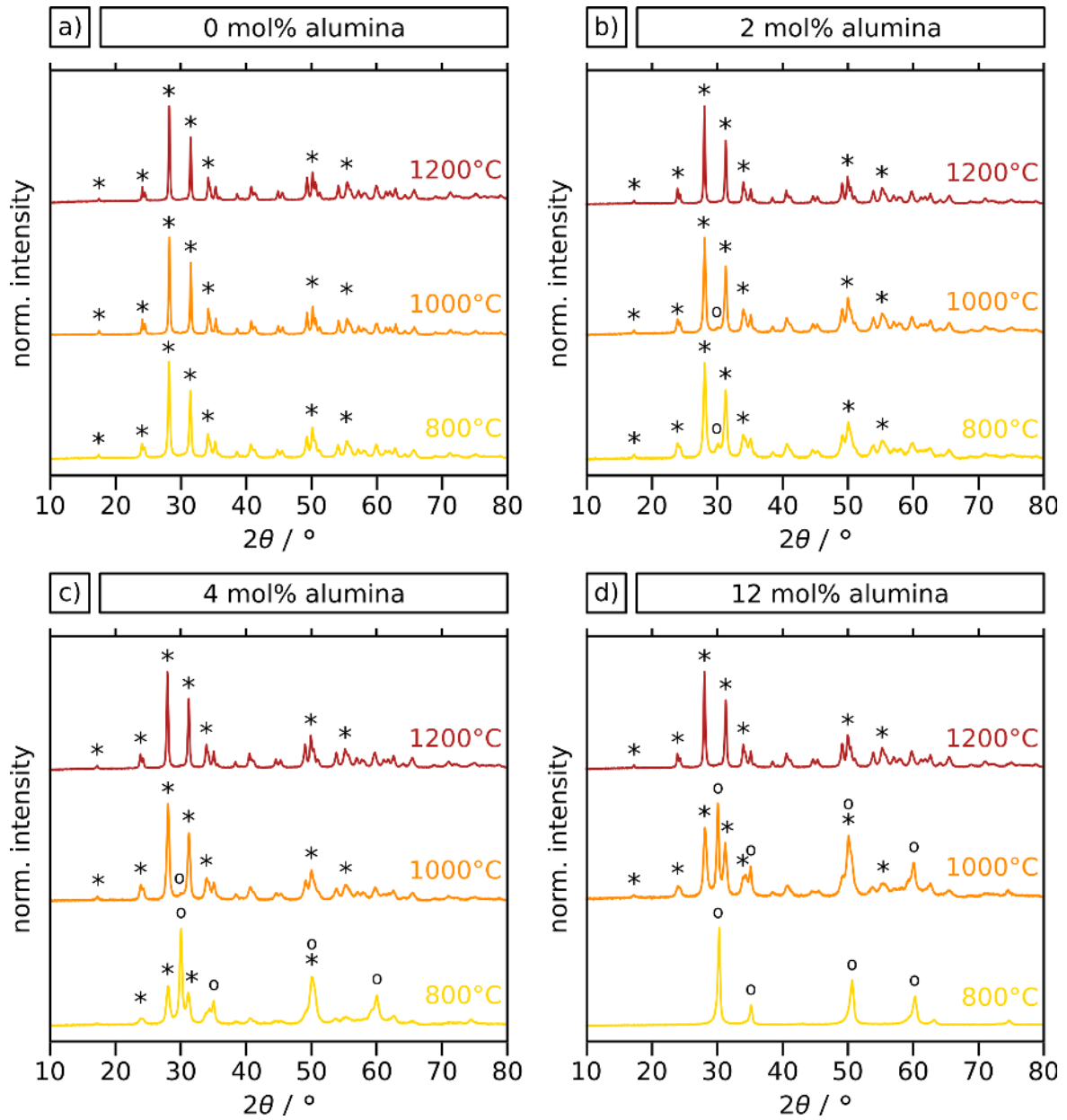
Figure 21: XRD patterns of selected alumina-doped zirconia particles after annealing at different temperatures. The samples containing varying amounts of alumina were annealed at 800, 1000, and 1200 °C for 3 h and analyzed ex situ. Characteristic peaks of the monoclinic ($*$) and the tetragonal/cubic ($\circ$) zirconia phases are annotated accordingly. Licensed under Creative Commons, reprinted from reference [143].
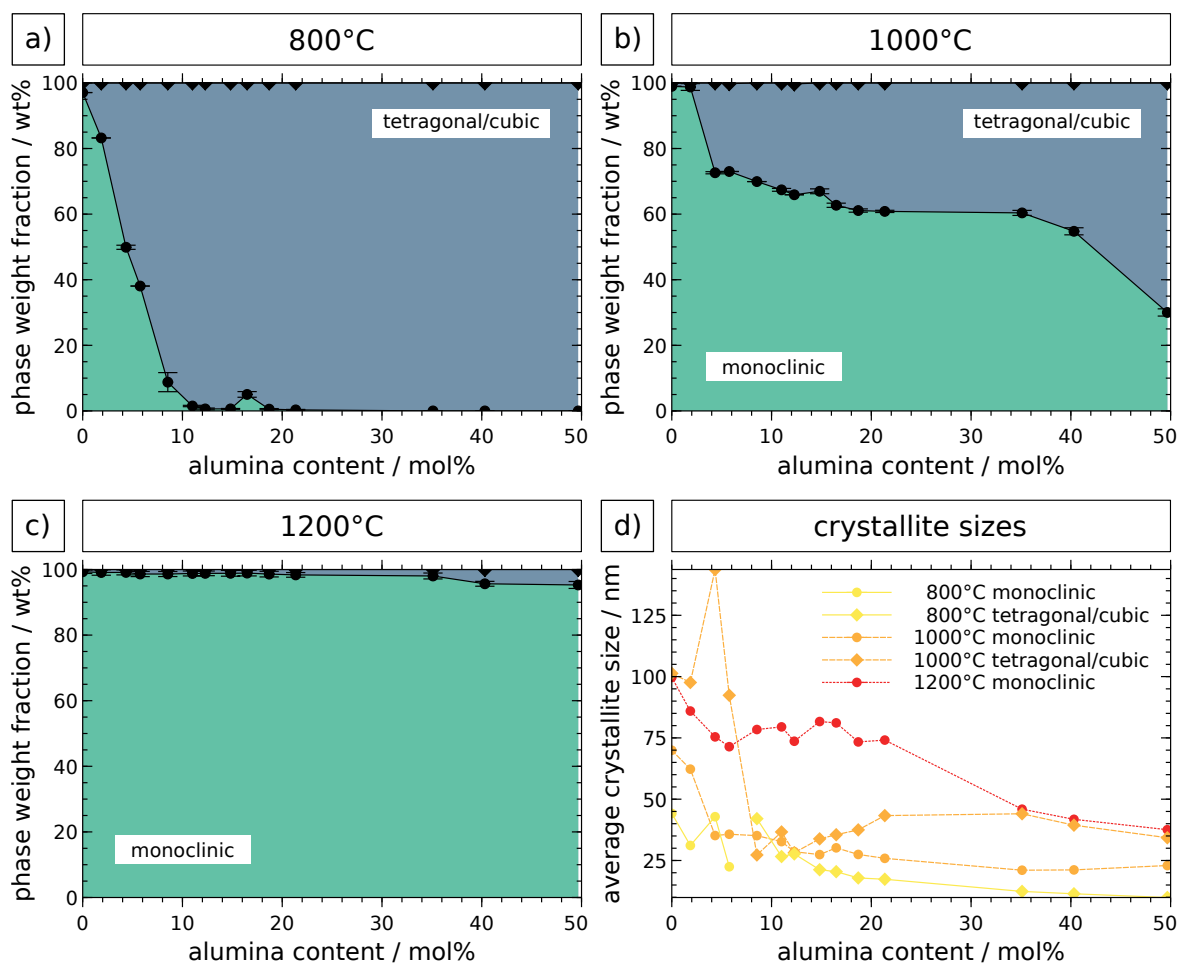
Figure 22: Quantitative phase analysis and crystallite sizes of annealed alumina-doped zirconia particles with varying alumina contents. The samples were annealed at **(a)** 800 °C, **(b)** 1000 °C, and **(c)** 1200 °C, phase weight fractions of the monoclinic and tetragonal/cubic phases were extracted from XRD data using Rietveld refinement. **(d)** Monoclinic and tetragonal/cubic crystallite sizes obtained from the same data, displaying only phases with a minimum weight fraction of 10 wt%. Licensed under Creative Commons, reprinted from reference [143].

metastable tetragonal to the monoclinic polymorph, as elaborated in Section 3.2.1. The
XRD patterns were, thus, in good agreement with the particle disintegration trends
observed by SEM (see Figure 20).

The relative amount of tetragonal zirconia after annealing can therefore serve as an
indicator for the stabilizing effect of the respective alumina content. All XRD data were,
thus, evaluated by Rietveld refinement for quantification of the crystal phase fractions
for all samples. The results are shown in Figure 22 (a–c). The samples annealed at
$800\,°C$ and $1000\,°C$ clearly show a strong correlation between the alumina content and
the stabilization of the tetragonal/cubic phase. Being more specific, the monoclinic
phase fraction after annealing at $800\,°C$ is reduced significantly by the addition of
alumina up to an alumina content of $12\,mol\%$. Above that, the tetragonal/cubic phase
is completely stabilized, almost no significant monoclinic fraction is detected. A similar
trend is observed for the samples annealed at $1000\,°C$. However, complete stabilization
at this temperature is not achieved, even with the highest alumina content in this study,
i.e., $50\,mol\%$. After annealing at $1200\,°C$, all samples have practically transitioned
to the monoclinic phase. Nonetheless, a small but significant tetragonal/cubic phase
fraction remained for samples with higher alumina contents, namely $\geq40\,mol\%$.

5.1.3   Microstructural Analysis

Using the Rietveld analysis data, average crystallite sizes were extracted in order to
study the influence of alumina-doping on the zirconia grain sizes. Besides the marten-
sitic phase transformation, grain growth represents another important mechanism for
structural destabilization of zirconia at high temperatures, as explained in Section 3.2.2.
The Rietveld method was used to obtain separate crystallite sizes for each individual
phase. These findings for the alumina-doped zirconia particle samples are illustrated
in Figure 22d. Here, data from phases with a relative phase fraction of $<10\,\%$ were
excluded due to insufficient peak intensity for reliable Rietveld fitting. Based on the
visualized results it is clearly visible that grain growth is generally more pronounced
in samples that were annealed at higher temperatures. No obvious trend for the
dependence of the grain size on the alumina content could be found. However, the
data indicate a certain tendency towards smaller grain sizes at higher alumina contents
for the t/c phase after annealing at $800\,°C$. Similarly, the monoclinic phase contains
smaller crystallites at higher alumina contents after annealing at $1000\,°C$ and $1200\,°C$.
Merely crystallites in the t/c phase after annealing at $1000\,°C$ show a slightly different
behavior: It is apparent that the grains of the t/c phase are larger than those in the
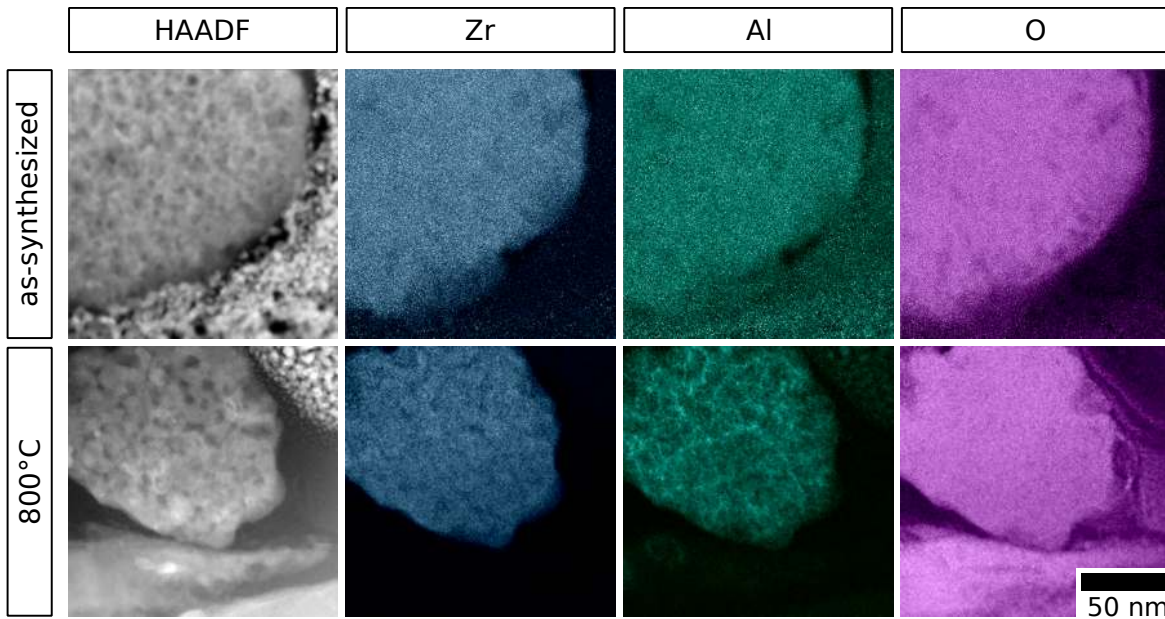
Figure 23: Element maps of as-prepared and annealed alumina-doped zirconia particles. The data were obtained by spatially resolved EDX analysis using STEM. Lamellae of deposited particle samples were prepared by focused ion beam thinning. The analyzed particles originate from the sample A20 with an alumina content of 20 mol% and represent the elemental spatial distribution before and after annealing at 800 °C for 3 h. Licensed under Creative Commons, reprinted from reference [143].

monoclinic phase of the same samples at low (<8 mol%) and again at higher alumina contents (>20 mol%). This contradicts the expectation based on previous findings, where smaller grains are preferably tetragonal and larger grains above a critical grain size tend to transition to the monoclinic phase.[71] The observations resemble those made in a study by Leib et al. concerning La-doped zirconia microparticles.[165] Here, two explanations were proposed: the formation of smaller monoclinic grains due to twinning during the phase transformation and a secondary grain formation at the grain-grain interfaces due to segregation into dopant-rich and dopant-lean regions. Both assumptions seem reasonable and would also be in good agreement with the findings of the study presented here.

In order to study the microstructural effect of alumina-doping on the properties of such particles in more detail, a selected sample pair containing 20 mol% alumina, as-synthesized and annealed at 800 °C, was investigated by spatially resolved elemental analysis. Cross-sectional cuts of one particle of each sample were prepared by focused ion beam (FIB) technique and analyzed by EDX elemental mapping using scanning transmission electron microscopy (STEM). The obtained element maps and the simultaneously recorded high-angle annular dark-field (HAADF) micrographs are

presented in Figure 23. A homogeneous spatial distribution of Zr, Al, and O across the entire particle cross-section is observed for the as-synthesized sample before annealing. Contrarily, segregation of alumina is found after annealing at 800 °C in a seemingly network-like manner. The Zr map shows a complementary distribution with rather weak signals in these Al-rich regions. A comparison with the HAADF micrograph reveals that the segregation appears to be located near the grain boundaries. These results are consistent with previous findings in various mixed Zr/Al oxide powders and zirconia materials doped with other metals.[107,224] With respect to the observations made regarding grain sizes of alumina-doped zirconia particles, these observations suggest that segregation of alumina at the grain-grain interfaces plays a key role in the inhibition of thermally induced grain growth. Grain boundary pinning can be considered as a possible mechanism underlying this process, as suggested elsewhere.[90] However, the presence of inter-grain alumina is difficult to prove with the methods that were available in this study. Amorphous phases are not detectable by XRD and crystalline alumina with dimensions of only a few nanometers will cause excessive line broadening due to the low number of diffraction planes. Such signals cannot be detected under the limited given characterization conditions. However, XRD analysis of a 20 mol% alumina-doped sample annealed at 1500 °C revealed the presence of crystalline alumina (see Appendix, Figure 45). This supports the hypothesis of alumina segregation and agrees with the poor solid solubility of alumina in zirconia reported in the literature.[102,103]

5.2   Alumina/Yttria-Doped Zirconia Particles

In the previous section it was demonstrated that the incorporation of alumina into sol-gel derived zirconia mesoparticles can enhance their thermal stability against disintegration by the inhibition of phase transformations and the retardation of grain growth. However, the extent of stabilization achieved by alumina-doping does not reach that of yttria-doping, the most common doping of zirconia. It was therefore decided to combine these two dopants and investigate the influence on phase and microstructural stability of the particles at high temperatures. In the study presented in this section, yttria-doped, alumina-doped, and yttria/alumina-codoped zirconia mesoparticles were synthesized by co-precipitation in a sol-gel synthesis, analogue to the previous section. The obtained particle samples were annealed at temperatures between 800 °C and 1400 °C. As-synthesized and annealed particles were characterized by TEM, SEM, XRD, and elemental analysis using EDX and OES. Most of this study was conducted
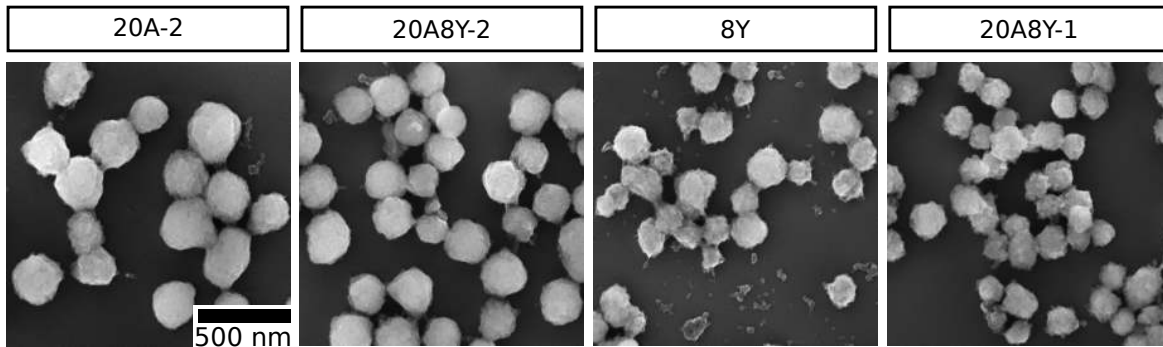
Figure 24: SEM characterization of selected as-synthesized mono- and codoped zirconia particles. The samples contained $20\,mol\%$ alumina (20A-2), $8\,mol\%$ yttria (8Y), or both $20\,mol\%$ alumina and $8\,mol\%$ yttria (20A8Y-1 and 20A8Y-2), based on the precursor composition. Adapted and reprinted from reference [225].

by Ms. Lea Klauke as part of her Bachelor thesis project under my supervision during my doctorate studies.[225] My contributions included conceptualization, data curation, formal analysis, methodology, data evaluation and interpretation, validation, and visualization as well as supervision of the experimental work.

5.2.1 Particle Synthesis

Doped zirconia microparticles were obtained following the same synthetic procedure as discussed in Section 5.1 and published recently.[143] Fixed values were chosen for the target alumina and/or yttria contents. The alumina content was set to $20\,mol\%$, because this amount proved to be well sufficient to significantly stabilize the tetragonal/cubic zirconia phase (see Section 5.1.2) and it is the only sample in the previous study that was investigated in detail using EDX mapping. For the yttria content, an amount of $8\,mol\%$ was chosen, as previous studies suggested this amount to be an optimum for the thermal stabilization of zirconia microparticles in the tetragonal phase.[137,148] The first goal was therefore the synthesis of respective particle samples with comparable average particle sizes and size distributions with the following target compositions: $(AlO_{1.5})_{0.2}(ZrO_2)_{0.8}$ (hence referred to as '20A'), $(YO_{1.5})_{0.08}(ZrO_2)_{0.92}$ ('8Y'), and $(AlO_{1.5})_{0.2}(YO_{1.5})_{0.08}(ZrO_2)_{0.72}$ ('20A8Y'). As shown at the beginning of the preceding section, the particle size of the final product is very sensitive to the amount of dopant precursor in the precursor mixture. It was therefore necessary to adjust the stabilizer composition for each synthesis individually in order to obtain samples with similar particle sizes. They were subsequently characterized by SEM, TEM, EDX, and elemental analysis. Representative SEM images of selected samples are shown in

Table 6: Summarized characterization data from electron microscopy and elemental analysis of as-synthesized alumina-doped, yttria-doped, and alumina/yttria-codoped zirconia particle samples. Average particle diameters d and relative standard deviations σ were determined by TEM. The complementary methods EDX and ICP-OES were used for elemental analysis of the cation compositions, given in mol%.

sample	TEM d / nm	σ / %	EDX Y	Al	Zr	OES Y	Al	Zr
20A-1	224.9	22.1	-	16.4	83.6	-	21.0	79.0
20A-2	235.5	24.6	-	16.3	83.7	-	22.6	77.4
20A8Y-2	215.9	19.5	14.8	15.2	70.0	9.6	20.0	70.4
8Y	177.1	19.7	16.1	-	83.9	10.7	-	89.3
20A8Y-1	182.1	15.3	15.5	15.4	69.1	10.2	21.1	68.7

Figure 24. TEM analysis was used to determine the average particle diameter and the size distribution, expressed by the relative standard deviation. Corresponding TEM images are depicted in Figure 25 (top row). Because the samples 8Y and 20A could not be obtained with similar particle sizes by adjustment of the stabilizer composition, 20Al8Y particles were synthesized in two sizes (by variation of the stabilizer composition), one each for comparison with every monodoped species. The size characteristics and elemental analysis of all particle samples are summarized in Table 6.

The TEM size analysis (see Section 8.2 for details) shows that there is a suitable analogue sample of codoped particles of similar average size for each monodoped sample, which enables the comparison of alumina/yttria-codoping with both monodoped species: 20A8Y-1 with 8Y, and 20A8Y-2 with 20A-1 and 20A-2. The sample 20A-2 is an upscaled reproduction of 20A-1 (factor 3) at identical reagent concentrations and synthesis conditions and with a very similar outcome. It underlines the good reproducibility and scalability of the particle synthesis and a high degree of control over the experimental procedure. Furthermore, the results of the elemental analysis (see Table 6) suggest a precise translation of the precursor molar ratios into the cation compositions of the final products. This tunability has been demonstrated in the previous section for monodoped zirconia particles and the applicability for codoped zirconia particles is shown here. The yittrium contents obtained by EDX seem significantly higher than expected. However, the evaluated signals of Y and Zr in EDX show a large overlap. The accuracy of their relative quantification by this method is therefore generally limited. Moreover, as elaborated in Section 5.1, OES values are expected to be more accurate and representative for the quantitative verification of

successful doping. The observed alumina and yttria contents agree well with the target compositions, solely the yttrium fraction in yttrium-containing samples is slightly higher than expected. A similar observation was also made in an earlier work, wherein it was attributed to the higher reactivity of the yttrium precursor.[8]

5.2.2 Thermal Stability

Analogously to the experiments described in the previous section, the codoped and monodoped zirconia particles were subjected to high temperature annealing experiments at 800, 1000, and 1200 °C and additionally at 1400 °C for 3 h in order to investigate the thermal stability. Here, the annealed particles were characterized qualitatively by TEM, representative micrographs are depicted in Figure 25. However, based on TEM no significant deviations between the different samples with respect to their particle morphology and structural disintegration after annealing could be observed. Therefore, ex situ XRD analysis was performed to examine the crystal phase compositions. The obtained diffractograms were evaluated quantitatively using Rietveld refinement to extract phase weight fractions and average crystallite sizes. The obtained original XRD diffractograms and the results of the Rietveld analysis are presented in Figure 26. Similarly to the previous section, tetragonal and cubic phase fractions could not be distinguished due to the high similarity of the crystal structure and significant line broadening and are therefore treated as one phase ('tetragonal/cubic').

The alumina-doped samples (20Al-1 and 20Al-2) show partial stabilization of the tetragonal/cubic zirconia phase against the martensitic phase transformation. Furthermore, a clear trend of increasing monoclinic weight fraction with higher annealing temperature is observed. This is in very good agreement with the results obtained for similar samples, as elaborated in the previous section and published recently.[143] Also a drastic increase in average monoclinic crystallite sizes is noticed as the temperature increases. It should be noted that crystallite sizes obtained from phases with a low weight fraction are inaccurate due to the low signal intensities in XRD. The observed trend fulfills the expectation, i.e., it indicates the typical enhancement of grain growth at higher annealing temperatures. When these findings are compared with the observations made for the analogue alumina/yttria-codoped sample (20Al8Y-2), significant differences are evident: The codoped samples contain almost no monoclinic zirconia after annealing up to 1000 °C and only a small fraction (∼5 wt%) after annealing at 1200 °C and 1400 °C. It is obvious that the codoping strongly suppresses the martensitic phase transformation in contrast to the alumina-monodoping. The observed phase fractions are in very good
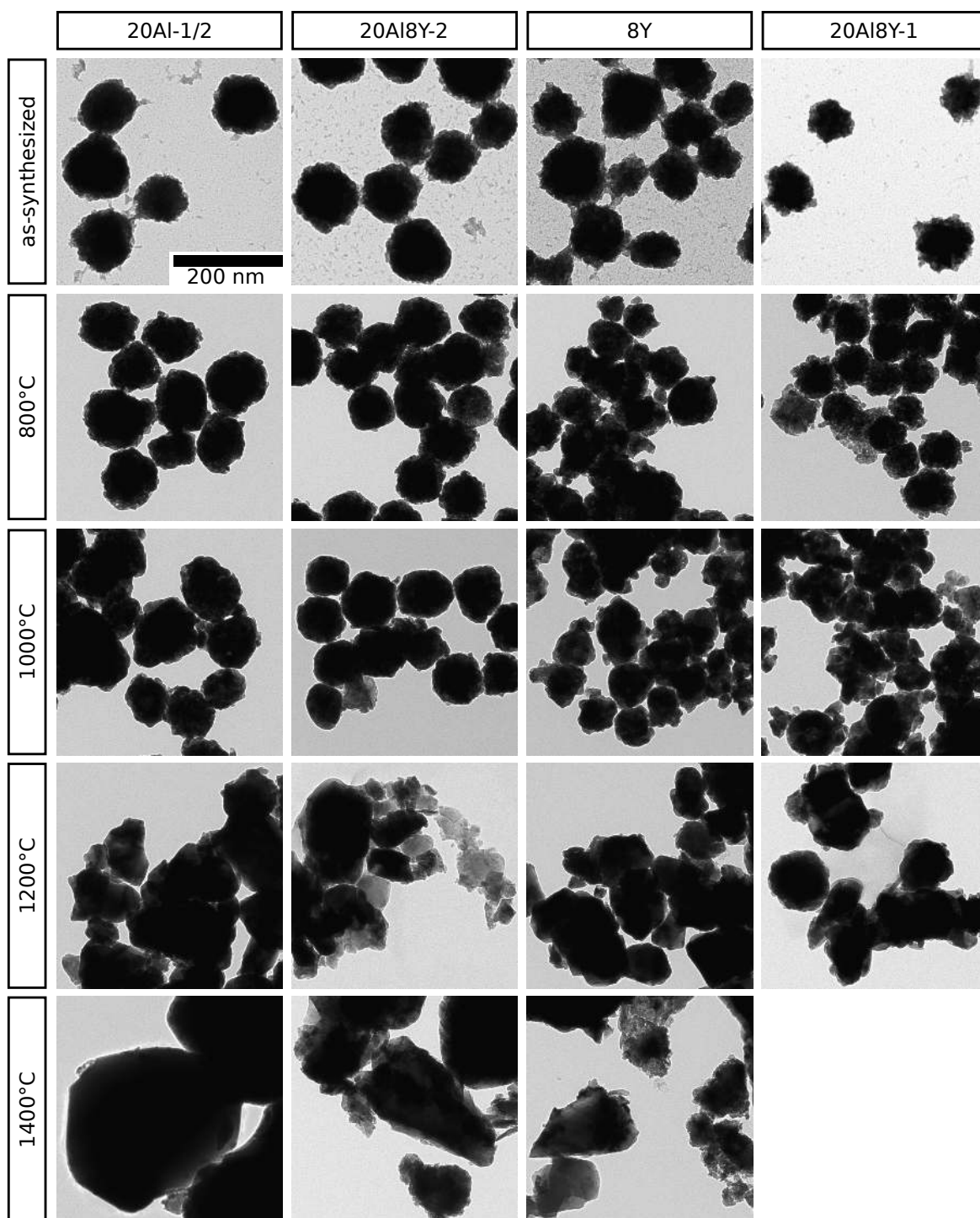
Figure 25: TEM micrographs of selected as-synthesized and annealed alumina-doped (20A-1/20A-2), yttria-doped (8Y), and alumina/yttria-codoped (20A8Y-1, 20A8Y-2) zirconia particle samples. Progressive particle disintegration is observed with increasing temperature. The sample 20Al8Y-1 could not be annealed at 1400 °C due to insufficient material quantity. Adapted and reprinted from reference [225].
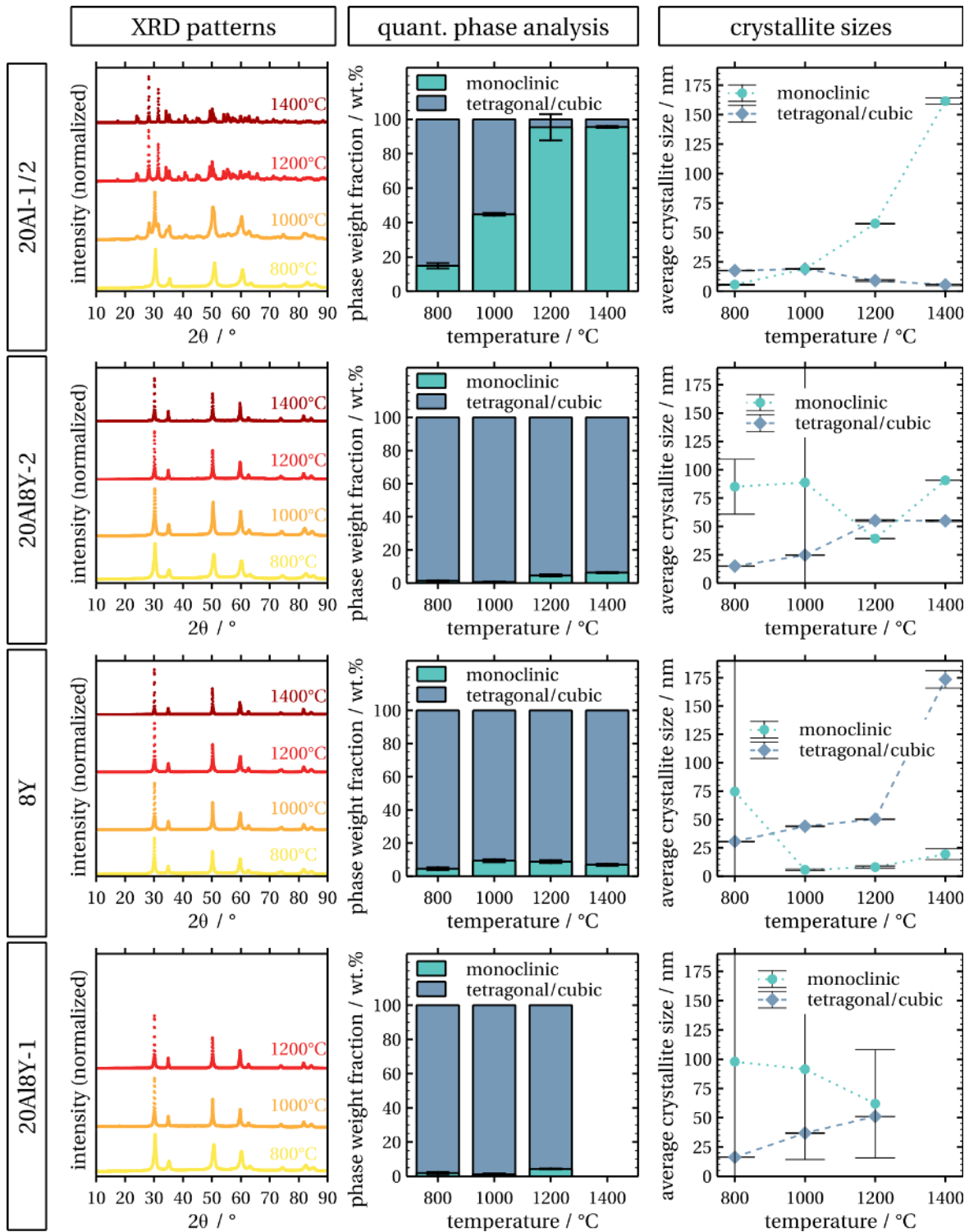
Figure 26: XRD patterns, quantitative phase analysis results, and average crystallite sizes of annealed alumina-doped, yttria-doped, and alumina/yttria-codoped zirconia particle samples. Rietveld analysis of the XRD patterns (left column) provided the data illustrated in the center and right column. The sample 20Al8Y-1 could not be annealed at 1400 °C due to insufficient material quantity. Note that crystallite sizes obtained from zirconia phases with very low weight fractions are considered inaccurate.
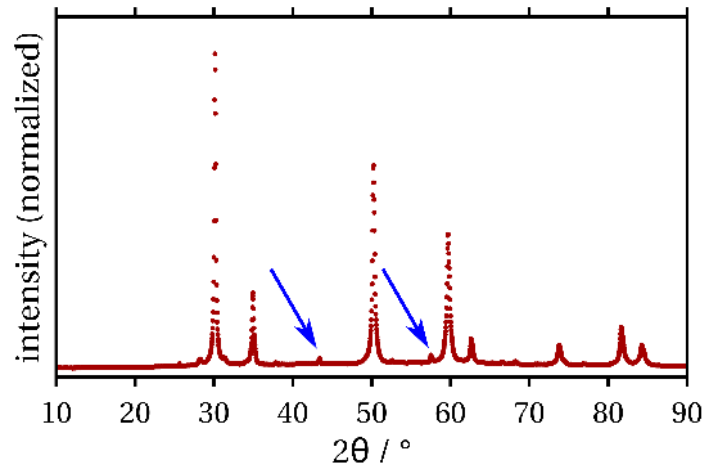
Figure 27: XRD pattern of alumina-doped zirconia particles (20Al8Y-2) after annealing at 1400 °C for 3 h. Besides the expected peaks of monoclinic zirconia, small characteristic signals of α-alumina (blue arrows) are observed after calcination.

agreement with the results for the alumina/yttria-codoped sample with smaller particle size (20AlY8-1). The yttria-monodoped sample (8Y) exhibits a high tetragonal phase fraction of 90 to 95 wt% across all temperatures. This was expected, since yttria in this concentration is known to stabilize tetragonal zirconia to a high extent.[8,137] While the phase stabilization does compare well to that of the alumina/yttria-codoped samples, a small deviation can be observed at lower temperatures (800 °C and 1000 °C). Here, the transition to the monoclinic phase may apparently be inhibited to a slightly higher degree by codoping with alumina/yttria.

With regard to crystallite sizes, all samples follow the general trend of larger crystallites after annealing at higher temperatures. However, an interesting observation is made after annealing at 1400 °C when comparing the yttria-doped (8Y) and alumina/yttria-codoped (20Al8Y-2) samples: Albeit the yttria-doping does stabilize the tetragonal/cubic phase mostly at this temperature, excessive grain growth occurs. In contrast, for the codoped sample no significant increase in average grain size is observed when comparing the values obtained after anneling at 1200 and 1400 °C. As found in the previous section, alumina tends to segregate near the grain boundaries upon annealing. It is therefore conceivable that alumina-rich regions form at the grain interfaces providing a more effective barrier against diffusion and mass transport than yttria alone does with its well-known solute drag effect (see Section 3.2.3). This assumption is supported by Goncalves et al., who observed reduced grain growth of zirconia when coated with alumina acting as a diffusion barrier.[226] Surface-coating of nanocrystalline zirconia with a thin layer of highly alumina-doped zirconia by Srdić et al. also confirmed this

hypothesis, as it resulted in significantly reduced grain coarsening.[227] Providing proof for the existence of such inter-grain alumina phases by the methods used in this work is very difficult, as discussed in the previous section. However, in one of the codoped samples (20Al8Y-2) annealed at 1400 °C, very small signals were detected that can be attributed to α-alumina, as shown in Figure 27. This indicates a phase separation, thus supporting the assumption of alumina formation and its role in grain growth inhibition. This effect might also be further promoted by a decreased solid solubility of alumina in zirconia at higher calcination temperatures, as reported by Srdić et al.[228]

5.3 Silica@Gold(@Silica) Composite Particles

In Section 3.4 it was elaborated that gold nanoshells deposited onto spherical ceramic particles have potential applications in various fields. For photonic materials, e.g., metasurfaces for TPV, the deposition of a second, outer ceramic shell is also of interest for optical tuning.[36] In order to obtain the expected and desired optical properties, well-defined particle and shell geometries are crucial. Here, submicrometer-sized core particles and a shell thickness in the nanometer region were chosen with respect to potential applications in opical metamaterials, e.g. for TPV. For zirconia, highly monodisperse spherical mesoparticles are yet unavailable by state-of-the-art synthetic protocols. Contrarily, the synthesis of spherical silica particles is very well understood and narrow size distributions can easily be obtained as well as substantial quantities. Therefore, the model system $SiO_2@Au@SiO_2$ was chosen for initial experiments with the goal to fabricate closed gold and silica shells with tunable thicknesses via a wet-chemical route. A recently published protocol for the preparation of the analogue $SiO_2@Pt@SiO_2$ particle system by Petrov et al.[199] served as a starting point and was adapted for gold shells. Compared to platinum nanoshells, gold nanoshells are expected to show improved optical properties with respect to damping of the plasmon resonance.[229] The multi-step preparation method is illustrated in Figure 28, it is based on previous protocols for gold and platinum nanoshells.[189,199] Preparative and analytic work presented in this chapter was conducted in parts in collaboration with my former colleague Dr. Alexey Petrov. FIB preparation and subsequent TEM characterization were performed by Mr. Andreas Kornowski.

5.3.1 GNP Immobilization

Spherical silica mesoparticles were provided by Dr. Alexey Petrov and had been obtained in the context of his dissertation using the Stöber method, followed by two

SiO$_2$ SiO$_2$-NH$_2$ SiO$_2$@GNP   SiO$_2$@Au   SiO$_2$@Au@SiO$_2$
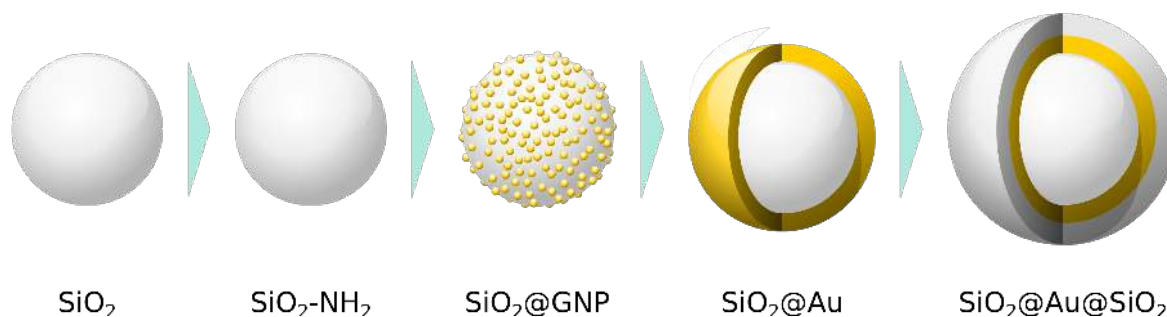
Figure 28: Synthesis strategy for SiO$_2$@Au@SiO$_2$ composite particles. The preparation comprises amino-functionalization of silica particles using 3-aminopropyl triethoxysilane (APTES), immobilization of small gold nanoparticles (GNPs), gold nanoshell deposition by reductive seeded growth, and silica encapsulation using tetraethyl orthosilicate (TEOS).
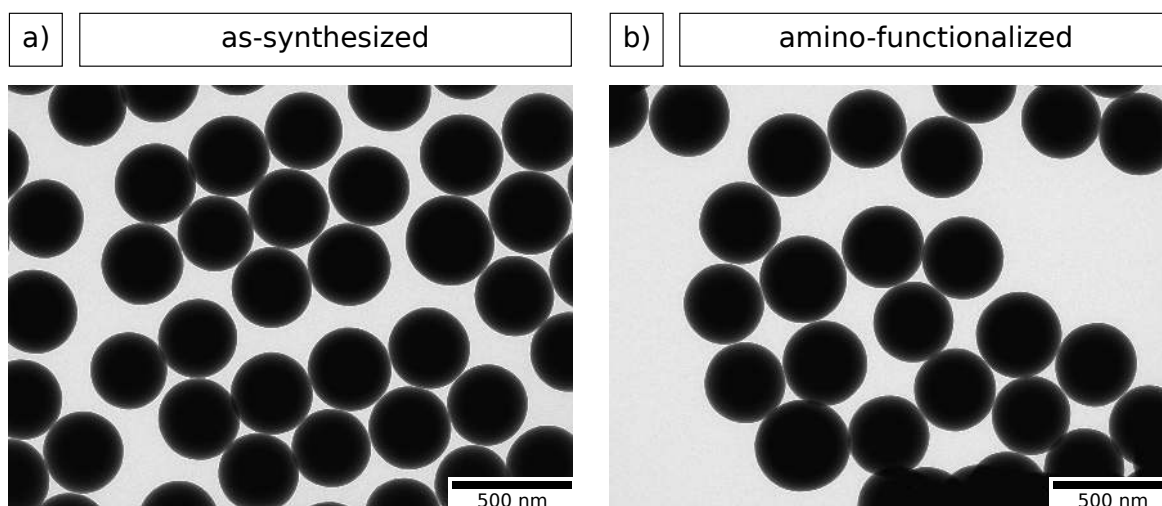
Figure 29: TEM analysis of silica particles. **(a)** As-prepared particles obtained via the Stöber process and two subsequent seeded growth steps. **(b)** The same particle sample after amino-functionalization using 3-aminopropyl triethoxysilane (APTES), which is accompanied by a measurable increase in particle size due to the deposition of a thin layer of amino-silica.
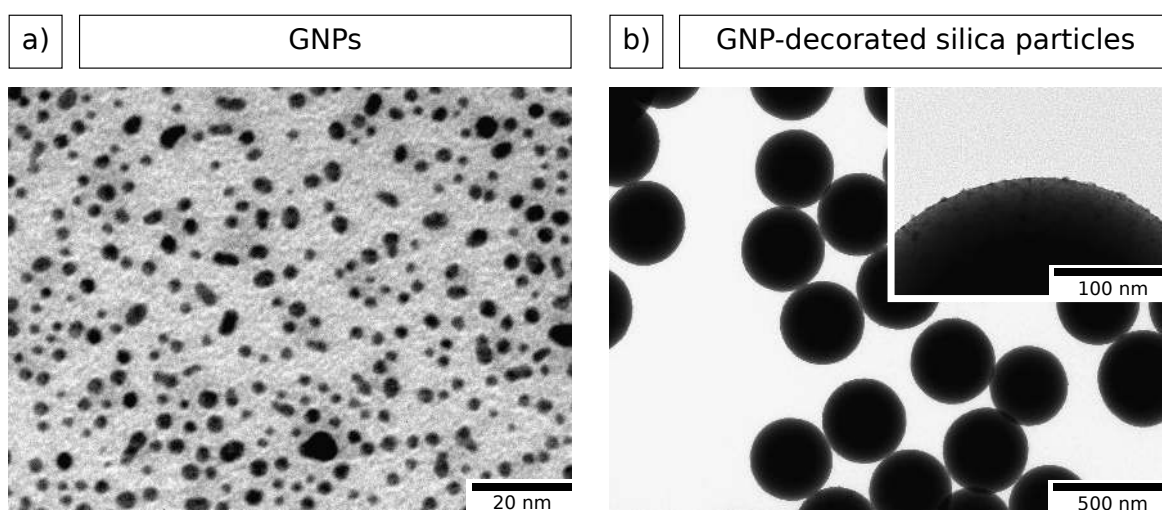
Figure 30: TEM analysis of GNPs before and after immobilization on silica particles. (a) As-prepared gold nanoparticles. **(b)** Amino-functionalized silica mesoparticles homogeneously decorated with surface-immobilized GNPs.

seeded growth steps.[134,230] Representative TEM images are shown in Figure 29. The highly monosdisperse and perfectly spherical as-prepared particles had an average diameter of 337 nm ($\pm 2.5\%$). Amino-functionalization was achieved by treatment with 3-aminopropyl triethoxysilane (APTES) in tetrahydrofuran (THF), and was accompanied by an increase in size to 347 nm ($\pm 2.9\%$) due to the deposition of a thin amino-silica layer by polycondensation. The functionalized particles were used as starting material for the experiments presented in this section.

A colloidal sol of small gold nanoparticles was synthesized by reduction of chloroauric acid in an aqueous solution containing sodium hydroxide following a protocol by Duff et al.[187] Here, tetrakis(hydroxypropyl)phosphonium chloride (THPC) served as both reducing and stabilizing agent. Using this method, small GNPs with an average diameter of (2.9 ± 1.0) nm were obtained in the form of a dark brown solution. Addition of a small amount of readily dispersed amino-functionalized silica particles to the as-prepared GNPs in combination with ultrasonication and subsequent stirring yielded a homogeneous coverage of the silica particle surface with immobilized GNPs. Representative TEM images of both are depicted in Figure 30. The purified particle suspension was further used for the deposition of a gold nanoshell.

5.3.2 Shell Deposition

The deposition of gold nanoshells was achieved by adapting a protocol for the synthesis of platinum nanoshells.[199] Herein, GNPs immobilized on silica nanospheres served as
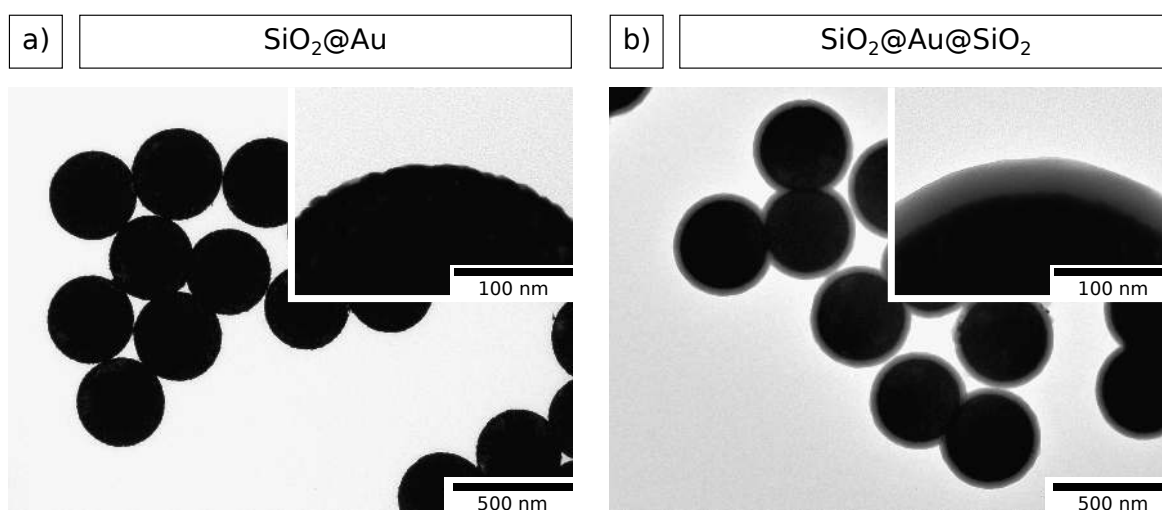
Figure 31: TEM analysis of as-deposited gold nanoshell and outer silica shell. (a) Homogeneous seeded growth of the gold shell on the GNP-decorated silica particle surface is achieved. **(b)** A smooth outer silica shell with constant thickness could successfully be deposited onto the gold nanoshell.

deposition nuclei for seeded growth of homogeneous platinum nanoshells with variable thickness. In the present work, in lieu of chloroplatinic acid, chloroauric acid was used. As described in Section 3.4.2, an aged mixture of chloroauric acid and potassium carbonate (K-gold solution) has proven to favor surface-attached reduction and avoid secondary nucleation in solution.[192] Therefore, a K-gold solution was used as the gold precursor. Ascorbic acid served as reducing agent in order to enable a more controlled reduction compared to other reported reducing agents (see Section 3.4.2). The obtained SiO_2@Au particle sample was characterized by TEM, representative micrographs are shown in Figure 31. Gold nanoshells with a thickness of $\sim$12 nm could be deposited homogeneously on all particles. This is in good agreement with the observations made for the growth of platinum nanoshells.[199] Although a slight surface roughness is present (see Figure 31a, inset), the homogeneity of the nanoshell appears significantly higher than in other reported studies,[190,231–233] particularly for thin shells. The employment of ascorbic acid as reducing agent is a possible reason for this. It is assumed that the rather mild redox conditions enable a slower and more controlled reduction of gold and, consequently, lead to a more homogeneous dispersion over the entire particle surface.

In a subsequent step, a silica shell was deposited on top of the gold nanoshell using the protocol for silica encapsulation of platinum nanoshells.[199] Briefly, this was achieved by hydrolysis of TEOS and polycondensation on the gold nanoshell surface using polyvinylpyrrolidone as coupling agent. The obtained SiO_2@Au@SiO_2 particle sample
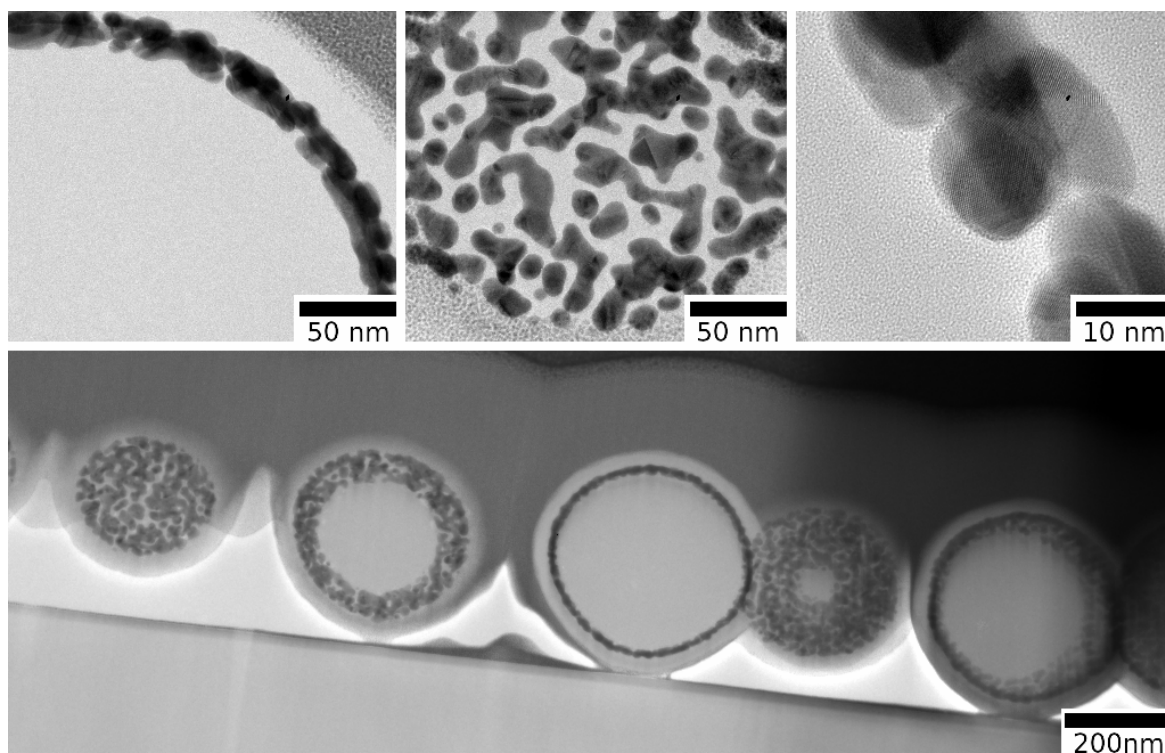
Figure 32: FIB/TEM analysis of SiO$_2$@Au@SiO$_2$ particle assemblies. Representative scanning transmission electron micrographs of SiO$_2$@Au@SiO$_2$ particles, sliced by focused ion beam thinning. The camouflage structure of the deposited gold is clearly visible and disproves the existence of a closed gold nanoshell. The FIB/TEM characterization was performed approximately three months after the shell deposition.
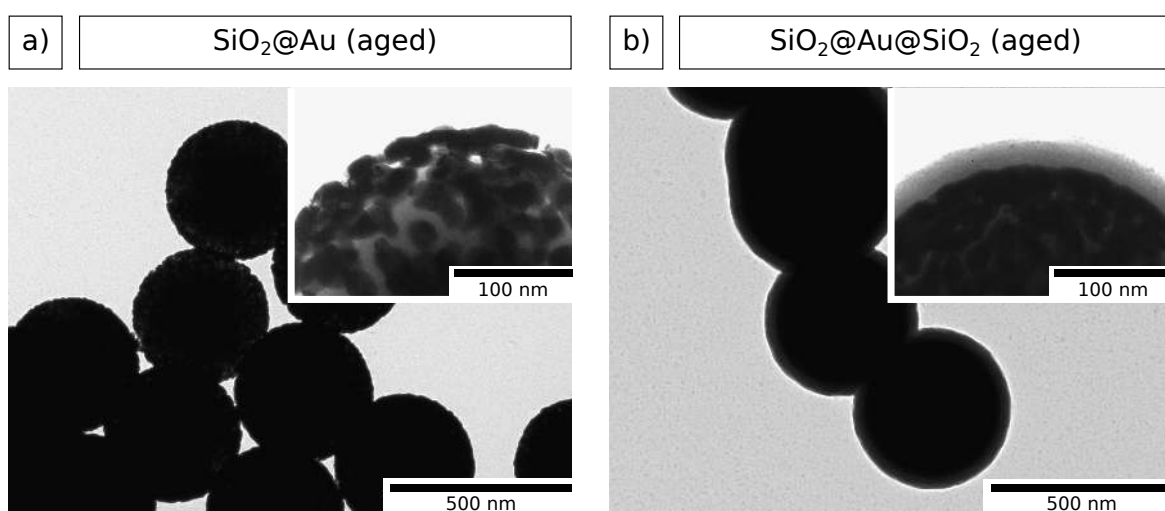
Figure 33: TEM analysis of aged SiO$_2$@Au@SiO$_2$ particles. Representative transmission electron micrographs of **(a)** SiO$_2$@Au and **(b)** SiO$_2$@Au@SiO$_2$ particles three months after synthesis. A significant segregation of gold and the formation of a camouflage structure is observed, even underneath the outer silica shell.

was characterized using TEM, representative micrographs are depicted in Figure 31b. A smooth silica shell with a constant thickness of $\sim$35 nm homogeneously deposited on all particles is observed. In order to study the morphology of both shells in more detail, a sample of the SiO_2@Au@SiO_2 particles was assembled on a silicon substrate and thinned using FIB technique. The obtained lamella with a thickness of $\sim$100 nm was characterized using TEM, which allows a cross-sectional insight into the material structure. Representative micrographs are shown in Figure 32. The cross-sections of the silica core and outer shell (light) and the gold inner shell (dark) are clearly visible. Surprisingly, the gold shell shows a non-closed camouflage structure. At this point it should be noted that a period of approximately three months had passed between the fabrication of core@shell@shell particles and the FIB/TEM characterization. It was therefore unclear, whether the observed delamination and segregation of gold was caused by the FIB processing or proceeded over time, presumably due to poor adhesion characteristics of gold on silica.[234] Hence, TEM characterization of the aged samples was conducted, representative micrographs are depicted in Figure 33. In comparison with the freshly prepared samples (Figure 31), significant gold segregation is observed, even underneath the outer silica shell. It is therefore concluded that the segregation observed in Figure 32 was probably not caused by the FIB preparation. Presumably, a high surface energy of the gold shell is the driving force underlying the observed behavior and the poor adhesion between gold and silica additionally facilitates delamination.[234] While as-prepared SiO_2@Au(@SiO_2) composite particles exhibit a promising morphology of the gold nanoshell with respect to contiguity and homogeneity, the findings show a poor long-term persistence of the shell structure. This remains a serious hurdle for potential applications of silica-supported gold nanoshells.

In high temperature photonic materials, e.g., metasurfaces for selective TPV emitters, a closed gold nanoshell with defined geometry is crucial. The results in this section demonstrate that these requirements are difficult to achieve with the typical silica@gold material system due to unfavorable material interactions and structural instability of the gold shell. Furthermore, because of its limited thermal stability, silica may not be suitable for the design of materials applied in high temperature environments ($<$1000 °C). However, the experiences with this interesting nanomaterial inspired the development of a novel material system, which will be discussed in the next section.

5.4   Zirconia@Gold Composite Particles

In this study, a novel approach for the preparation of zirconia@gold spherical mesoparticles in aqueous solution is presented. It was inspired by the method for silica@gold particles that was discussed in the previous section. Zirconia mesoparticles, prepared by the method described in Section 5.1, served as a starting material. The immobilization of nanoparticulate gold on the surface of such particles and the controlled deposition of additional gold by seeded reduction have not yet been reported in the literature. The permanent attachment of gold on zirconia is therefore likely to pose a major synthetic challenge. The results presented in this section were published recently.[235] In the underlying study, I was leading investigator regarding conceptualization, methodology, validation, investigation, and formal analysis as well as manuscript draft writing, editing, and review. Preliminary experiments contributing to the design of the study were conducted by Mr. Jan-Dominik Krueger in the course of his Bachelor thesis during my doctorate studies and under my supervision.[236] The zirconia particles used here were prepared by Mr. Sebastian Döring in the context of his Master thesis.[223]

Undoped zirconia mesoparticles with an average particle diameter of (384 ± 36) nm were dried and calcined at $600\,°C$ for $3\,h$ in order to remove residual organics and to achieve densification. The approach for the preparation of ZrO_2@Au composite particles resembles the synthesis protocol for SiO_2@Au particles that was described in the previous section (see Figure 28): Amino-functionalization of the ceramic particle surface followed by immobilization of GNPs and finally seeded growth deposition of gold. However, zirconium compounds analogue to APTES are not commercially available and the sol-gel chemistry of zirconia and silica are very different due to the large discrepancies regarding the reactivities of the respective precursors.[237] Therefore, amino-functionalization of the zirconia particle surface could not be achieved similarly to that of silica particles. For the immobilization of GNPs on the zirconia surface, a dual strategy was pursued here. It involved the employment of aminomethylphosphonic acid (AMPA) as coupling agent and acidification using hydrochloric acid. The subsequent seeded growth deposition was expected to be achieved similarly to that on GNP-decorated silica particles. The complete synthesis strategy is schematically illustrated in Figure 34.

AMPA was chosen as coupling agent for several reasons: it possesses both an amine and a phosphonic acid group, which are known to have sufficient binding affinity to GNP and zirconia surfaces, respectively;[239–242] it is a small molecule, keeping the amount of introduced organic material low; and it is commercially available at a low cost. Among
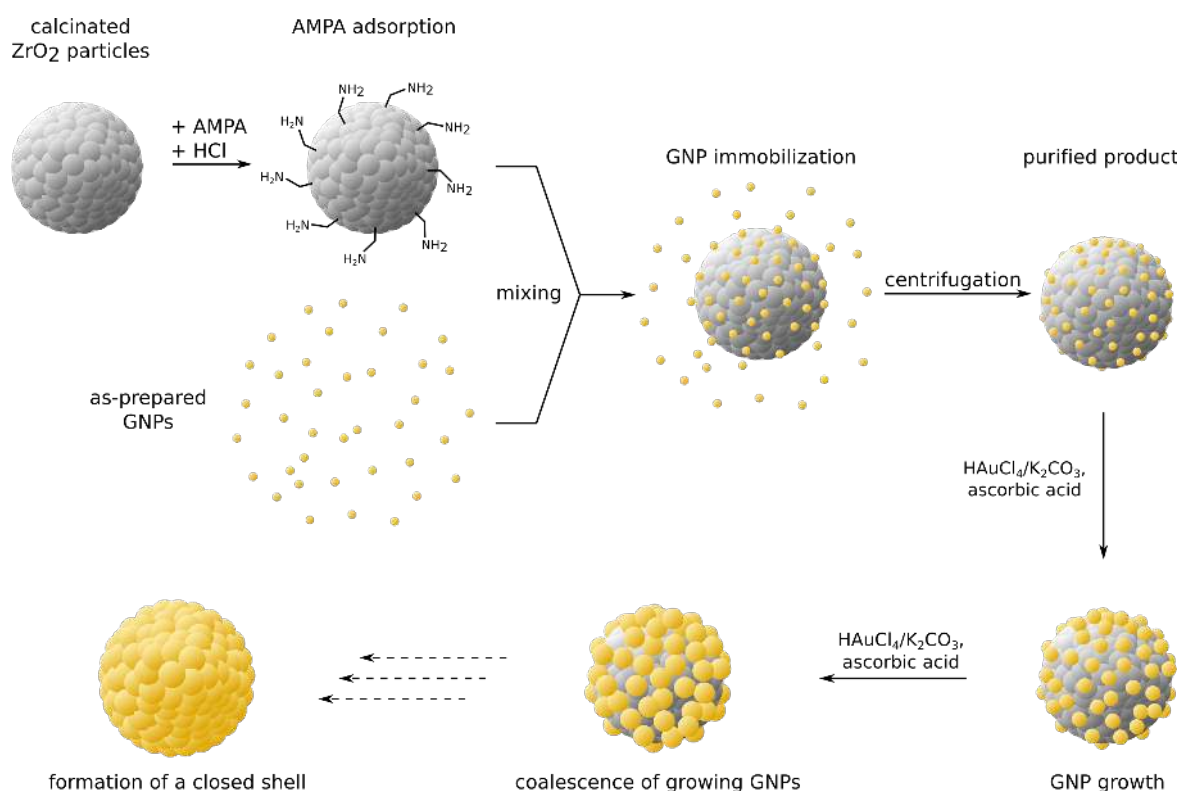
Figure 34: Synthesis strategy for novel zirconia@gold composite mesoparticles. Small GNPs are immobilized on the surface of calcined zirconia particles using aminomethylphosphonic acid (AMPA) and HCl. After purification, additional gold can be deposited by seeded growth. Repeated gold deposition is expected to result in the formation of a closed gold nanoshell. Licensed under Creative Commons, reprinted from reference [235].

the reagents involved during GNP immobilization, most components are pH-sensitive: the zirconia surface, the GNP surface and its electrostatic stabilizer THPC, and the ampholytic AMPA. It is therefore obvious that the pH will have a significant impact on the process and the efficacy of GNP deposition. Studies on the immobilization of citrate-stabilized GNPs on amine-functionalized silicon suggest that a pH of ∼5 would be optimal for the desired attractive interaction between the GNPs and AMPA.[243,244] GNPs prepared by the Duff method, as used here, possess a negative surface charge.[222] The amine functional group of AMPA should therefore be protonated in order to exhibit electrostatic attraction towards the GNPs. This was pursued by acidification of the reaction solution. In contrast to the amino-functionalization of silica particles using APTES, here, the amine group is not attached to the ceramic surface by a covalent bond. Hence, the merely electrostatic interaction between the zirconia surface and phosphonic acid of AMPA must be considered, too. AMPA is ampholytic with three relevant Brønsted protons and can occur in four possible protonation states,
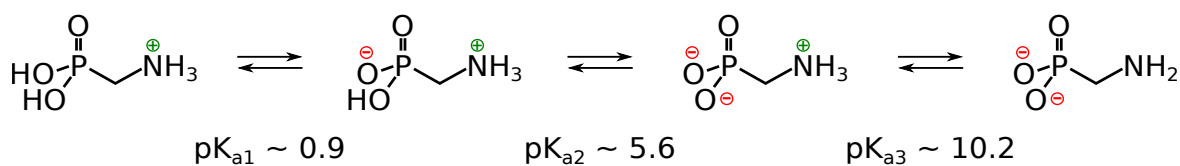
Figure 35: Ampholytic behavior of aminomethylphosphonic acid (AMPA). Due to the Brønsted-active functional groups AMPA occurs in four states of protonation in aqueous solution, depending on the pH. The given pK_a values denote the acidities of the corresponding protons.[238]

depending on the pH. These are shown in Figure 35 with the respective pK_a values,[238] resulting in an isoelectric point at ~3.25. For zirconia in water, the isoelectric point is approximately 6.7 to 6.9.[245,246] Therefore, at a pH between these two values, opposite charge of the phosphonic acid group of AMPA and the zirconia surface are expected, enabling electrostatic attraction.

These theoretical considerations provide good indications for suitable pH values for GNP immobilization on zirconia particles. However, the system is rather complex and involves too many components to enable a precise prediction of the optimal pH. It is therefore reasonable to determine the optimal pH empirically, which represents the first experimental series in this part of the dissertation. Furthermore, the influence of the acidity and the presence or absence of AMPA on the success of GNP immobilization were investigated, with the goal of maximizing the amount and surface density of immobilized GNPs. The most promising sample was then reproduced and used in subsequent experiments for the deposition of additional gold by seeded growth.

5.4.1 GNP-Immobilization at Varying pH Using AMPA

The addition of a strong acid in variable amounts is a straightforward way of adjusting the pH. In this study hydrochloric acid was used for this purpose. The experimental design for the GNP immobilization is schematically illustrated in Figure 34. Calcined zirconia mesoparticles and AMPA (final concentration: 6 mM) were mixed and variable amounts of HCl (final concentrations: 10^{-6} to 1 M) were added. Finally, an as-prepared colloidal solution of small GNPs (Ø (2.8 ± 0.9) nm) was added under intense mixing. All experiments were also similarly conducted in absence of AMPA in order to differentiate the effects of HCl alone from that of AMPA and HCl in combination. Purification was subsequently performed by repeated centrifugation and redispersion in water in order to separate the particles from excess free GNPs and small molecules (AMPA, THPC, HCl). The purified samples were characterized using SEM, ultraviolet/visible (UV/vis) spectroscopy, and elemental analysis by atomic absorption spectroscopy (AAS).
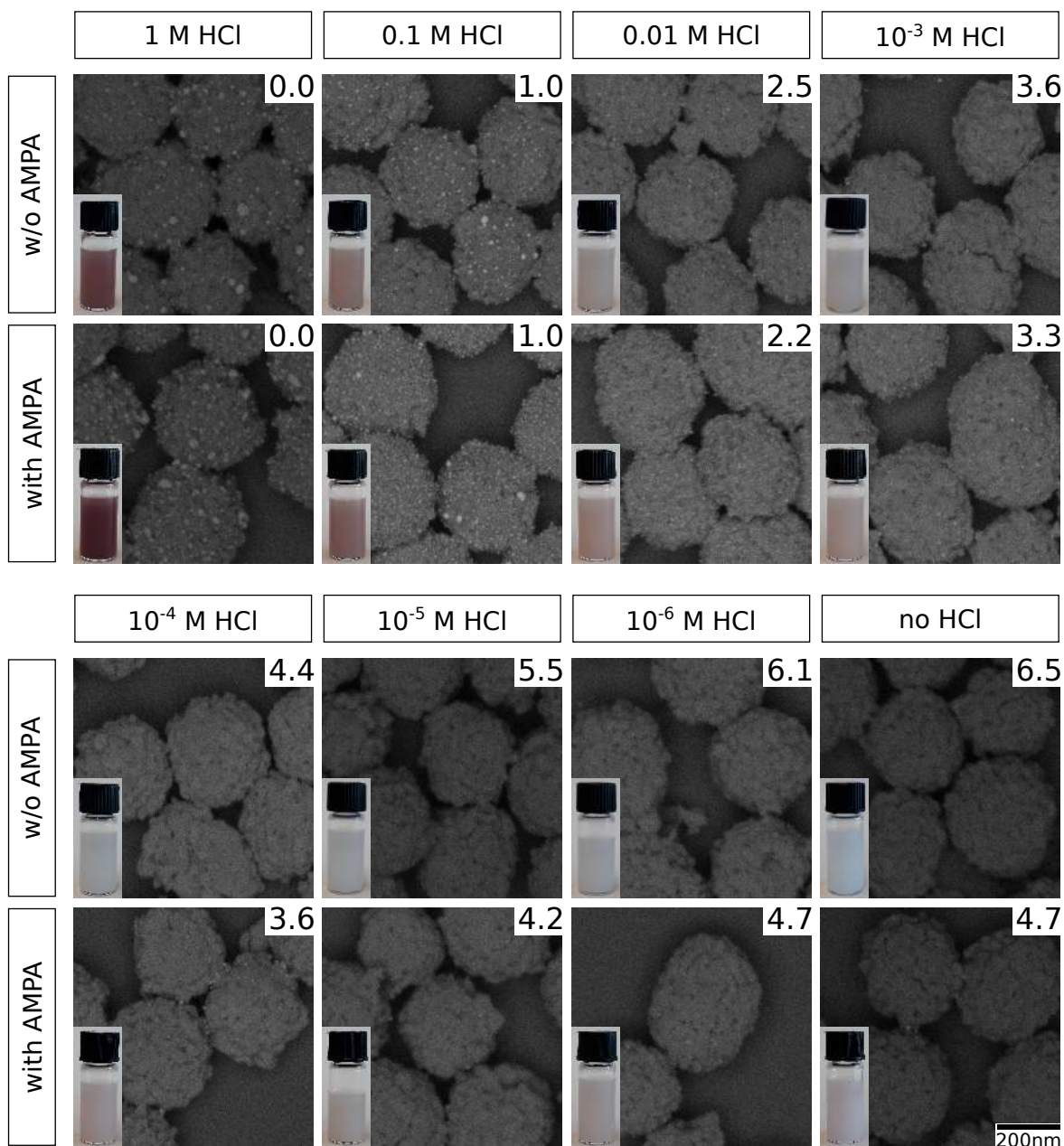
Figure 36: SEM analysis of GNP-decorated zirconia particles prepared under varying synthetic conditions. The samples were obtained by GNP immobilization at different HCl concentrations and in presence or absence of AMPA. Photographic images of the purified particle suspensions are shown in the insets, pH values were determined experimentally and are indicated in the top right corner. SEM images were collected using an energy-selective backscatter (ESB) detector, yielding a strong contrast between zirconia (dark) and gold (bright). Licensed under Creative Commons, reprinted from reference [235].

Additionally, pH values were determined experimentally for each sample. Representative SEM micrographs, corresponding photographic images and the respective pH values are depicted in Figure 36. It should be noted that the smallest GNPs can most likely not be detected due to the limited spatial resolution of the instrument. However, a sufficiently large fraction of GNPs is visible in order to draw meaningful conclusions about the GNP coverage from the micrographs shown.

Here, a clear trend of increasing GNP coverage with higher HCl concentrations and lower pH is observed. Significant amounts of immobilized GNPs are found for concentrations $\geq 10^{-3}$ M and pH values ≤ 3.3 in the presence of AMPA and ≥ 0.01 M and pH values ≤ 2.5 in absence of AMPA. Moreover, these particle suspensions (with the exception of those obtained with 1 M HCl) exhibit a light brownish color. This corresponds to the typical surface plasmon absorption of nanometer-sized GNPs and confirms their immobilization. A similar observation is made for samples with AMPA at HCl concentrations $\leq 10^{-4}$ M, though no GNPs were found by SEM. It is presumed that GNPs with sizes below the detection limit have been immobilized and cause the SPR excitation but are invisible in SEM. At an HCl concentration of ≥ 0.1 M, significant occurrence of GNP aggregates is observable in SEM. Particularly for the samples obtained at 1 M, a deep red/purple coloration indicates a significant spectral red-shift of the SPR excitation band, as discussed in Section 3.4.1. This finding confirms the occurance of GNP aggregation and coalescence. Black precipitates (not visible in the photographs) additionally support this conclusion. Apparently, an acidic environment at a pH between approximately 1 and 4 is favorable for GNP immobilization. This is in agreement with the literature, where similar observations were reported for adsorption of GNPs and metal complexes on oxide surfaces.[222,247] It should be noted, that the use of hydrochloric acid not only introduces acidic protons but also chloride ions. The observed effects are likely to be due by the acidity caused by the protons. However, an involvement of the chloride ions to any extent cannot be excluded with certainty at this point.

Regarding the influence of AMPA, samples obtained in the presence of AMPA show significantly higher GNP coverage than those prepared in absence of AMPA. This is particularly found for samples obtained at HCl concentrations of 10^{-3}, 0.01, and 0.1 M. The SEM results presented in Figure 36 therefore suggest that AMPA promotes GNP immobilization, as assumed based on the theoretical considerations at the beginning of this section. However, the enhancement of GNP immobilization by acidification using HCl in suitable concentrations is more pronounced than that achieved by AMPA coupling.
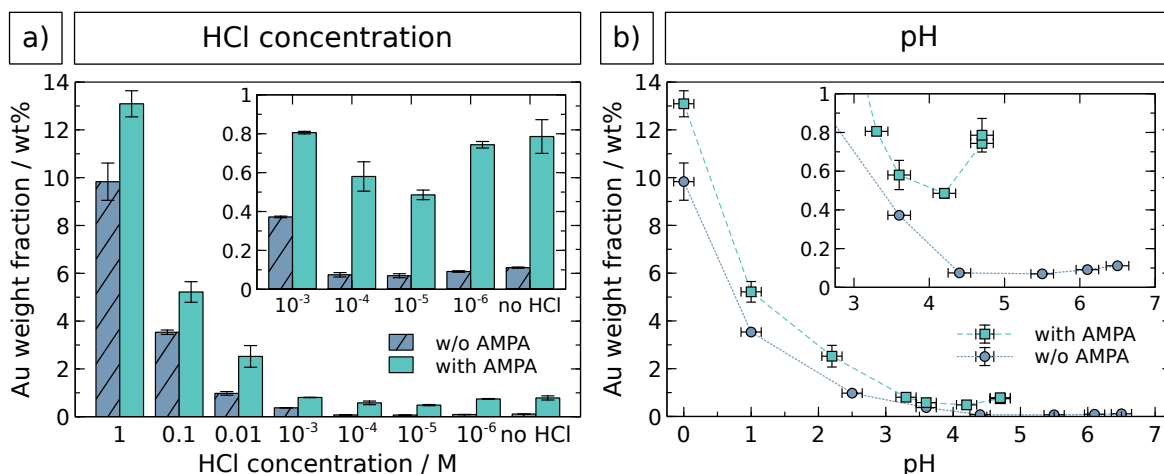
Figure 37: AAS analysis of GNP-decorated zirconia particles prepared under varying synthetic conditions. Au weight fractions of purified particle samples after GNP immobilization as a function of **a)** the HCl concentration and **b)** the pH, in presence or absence of aminomethylphosphonic acid (AMPA). The insets show enlarged segments of the same data. Error bars indicate the uncertainty defined by the standard deviation of multiple measurements or the weighing error, whichever value is larger. Licensed under Creative Commons, reprinted from reference [235].

In order to quantify the observed variations in GNP coverage, the samples were further characterized using atomic absorption spectroscopy (AAS) and UV/vis spectroscopy. The results are illustrated in Figure 37 and Figure 38, respectively. To account for deviations in particle concentrations as a result of the synthesis and purification process, weight concentrations were determined gravimetrically. The UV/vis results were therefore corrected via division by the particle concentrations. Details are provided in Table 10 in the Experimental Section and in the Appendix (Table 13).

The AAS and UV/vis results clearly confirm the general trend already identified by SEM and the observed coloration of suspensions: With increasing HCl concentration, the amount of immobilized gold increases substantially. Furthermore, GNP immobilization proves to be more effective when conducted in the presence of AMPA. Comparing the results with samples obtained in absence of AMPA and as a function of pH (Figure 37b and Figure 38b), the observed effect cannot be explained by the acidity alone. A favorable effect of AMPA due to electrostatic coupling, as considered prior to this study, seems reasonable.

For HCl concentrations of $\leq 0.01\,\mathrm{M}$ and pH values ≥ 2.2, there were no indications for significant GNP aggregation, hence the determined Au fraction presumably represents only immobilized GNPs. However, for higher HCl concentrations and lower pH, SEM has revealed substantial occurrence of GNP aggregation. Although, high Au fractions were obtained in AAS analysis for these samples, they must be ascribed at least partially
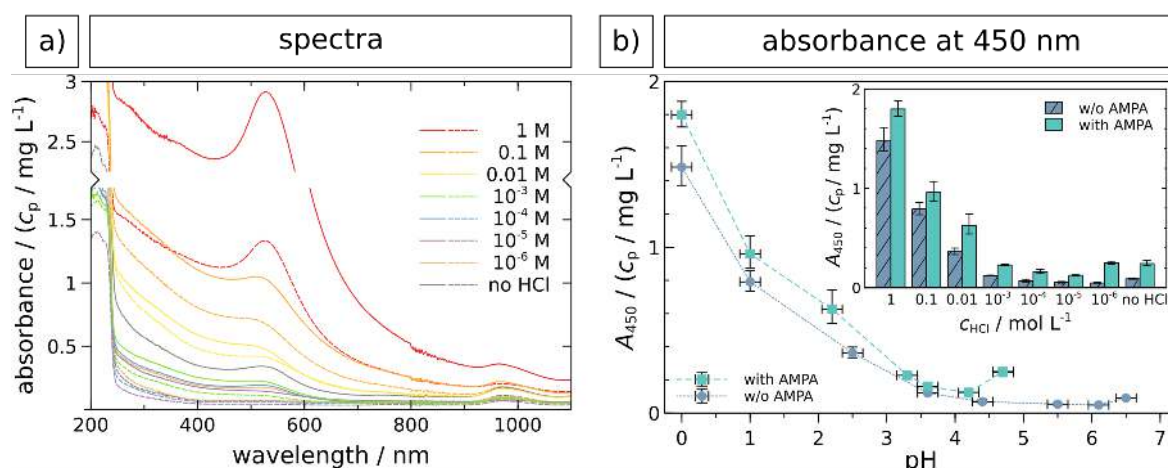
Figure 38: UV/vis analysis of GNP-decorated zirconia particles prepared under varying synthetic conditions corrected for varying particle concentrations. **a)** Absorbance spectra for samples obtained by GNP immobilization at varying HCl concentrations, in presence (solid lines) and absence (dashed lines) of AMPA. **b)** Extracted absorbance at 450 nm as a function of HCl concentration (inset) and pH (main plot). Error bars indicate the uncertainties concerning the determination of pH (horizontal) and particle concentration (vertical). Licensed under Creative Commons, reprinted from reference [235].

to GNP aggregates, either immobilized or freely dispersed but too large for effective separation during purification. This assumption is also strengthened by the spectral red-shift of the SPR band in the UV/vis spectra.

In summary, the following conclusions were drawn from this study: The coverage of zirconia particle surfaces with immobilized GNPs can be significantly increased by lowering the pH via addition of hydrochloric acid; The employment of AMPA as a coupling agent has a significant but weaker promoting effect; At higher HCl concentrations (≥ 0.1 M) or low pH (≤ 1), GNP aggregation occurs; Optimal conditions for GNP immobilization with high surface coverage but without aggregation are in the region of 0.01 M HCl in combination with the addition of 6 mM AMPA. A scaled-up reproduction of the respective experiment was conducted to prepare a larger sample quantity for further experiments. The characterization results of the reproduced sample were in very good agreement with those of the original sample, details are provided in Table 10 in Table 10 in the Experimental Section and in the Appendix (Table 13).

5.4.2   Seeded Growth of Immobilized GNPs

In a subsequent study, it was intended to achieve a controlled and homogeneous growth of the immobilized GNPs by seeded reduction of ionic gold, as illustrated in Figure 34. Preliminary experiments had confirmed, that deposition of gold on bare zirconia

Table 7: EDX quantification of ZrO$_2$@Au particles at different stages during gold deposition. The data were obtained by analysis of single particles or groups of a few particles and given in atom% relative to the sum of the three quantified elements. Indicated uncertainties represent the standard deviations of multiple measurements. Licensed under Creative Commons, reprinted from reference [235].

element	after GNP immobilization	after 1 deposition cycle	after 2 deposition cycles
O	65.1 ± 0.0	49.2 ± 6.4	54.1 ± 2.5
Zr	34.0 ± 0.1	36.8 ± 0.8	36.9 ± 1.8
Au	0.9 ± 0.1	4.0 ± 0.1	9.0 ± 0.7

particles was unsuccessful and led to uncontrolled formation of gold aggregates rather than homogeneous coverage of the particle surface. The preceding GNP immobilization was therefore considered a crucial step. Here, seeded growth was carried out in two identical deposition cycles. The purified suspension of GNP-decorated zirconia particles was therefore used as starting material. An aqueous solution of chloroauric acid and potassium carbonate ('K-gold', see Section 3.4.2) was prepared and used as gold precursor. For each deposition cycle, the diluted particle suspension was mixed with ascorbic acid as reducing agent followed by the dropwise addition of the K-gold solution at a constant rate under vigorous stirring. After the addition, stirring was continued for 1 h. Lastly, purification was achieved by repeated centrifugation and redispersion in water. Here, two deposition cycles were performed.

The subsequent characterization was conducted with samples of the three stages of gold deposition (after GNP immobilization, after 1 deposition cycle, and after 2 deposition cycles) in order to evaluate the stepwise progress of gold deposition. They were analyzed using SEM, TEM, and STEM/EDX element mapping. In addition, photographic images of the readily dispersed particle suspensions were taken. The results are presented in Figure 39. The SEM images (top row) indicate a gradual and significant growth of the immobilized GNPs between the three stages. There are no indications for the formation of gold aggregates, which suggests good control over the GNP-seeded reduction process. TEM images at higher magnifications (second row) clearly confirm the findings by SEM. Here, an overall growth of the GNPs from ∼3 to ∼15 nm after two deposition cycles is observed. Distinct changes are also found with respect to the coloration of the particle suspensions. The pale brownish color of the GNP-decorated particles transitioned over a strong red/purple to dark violet/black tone (top row, insets). Again, the color impressions are caused by SPR excitation, which is very sensitive to the GNP size and inter-particle distances. The first change from brownish to red/purple is similar to that
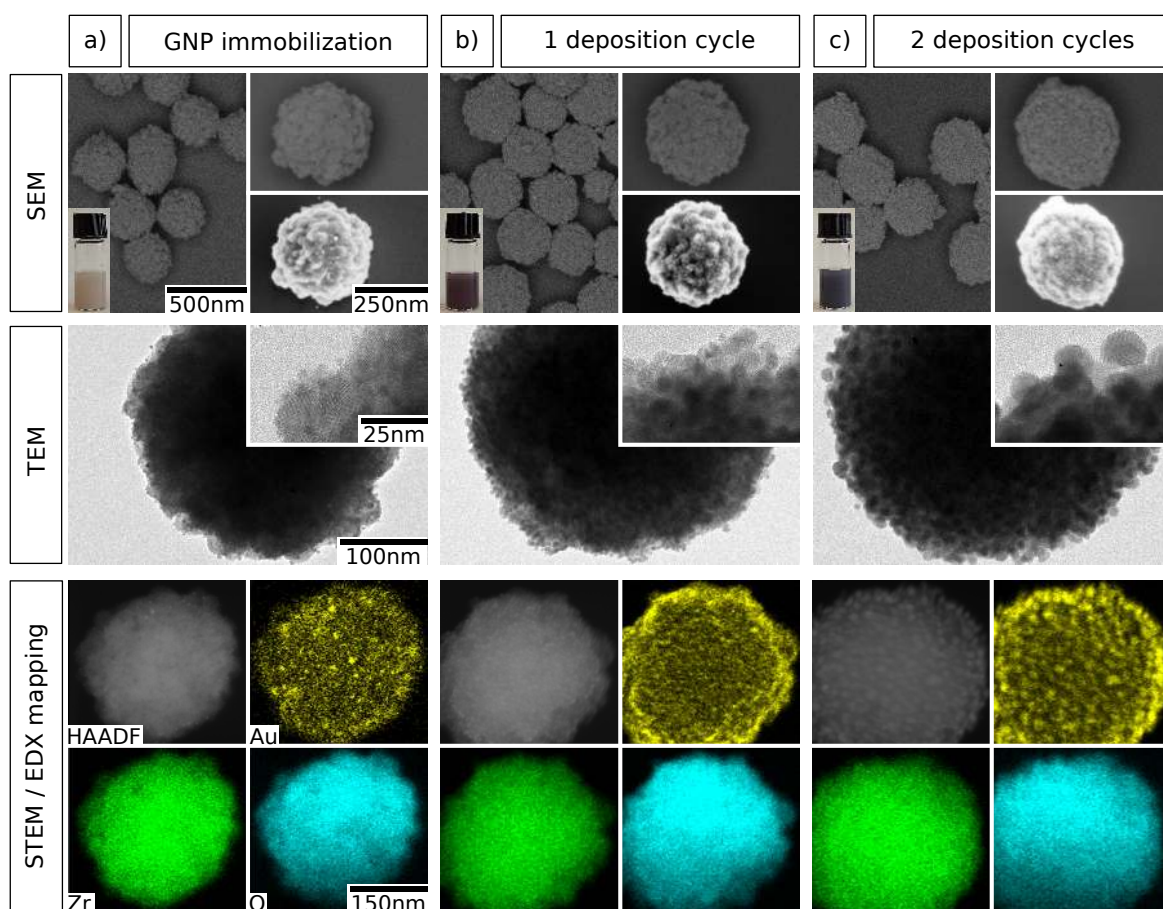
Figure 39: Electron microscopic, elemental, and photographic analysis of gold deposition on GNP-decorated zirconia particles at different stages. Characterization was performed **(a)** after GNP immobilization, **(b)** after 1 deposition cycle, and **(c)** after 2 deposition cycles. SEM images were obtained using an ESB (left and top right) or an in-lens detector (bottom right). Different individual particles from the same sample are shown in each column. Licensed under Creative Commons, reprinted from reference [235].

observed after GNP immobilization at high HCl concentrations in the previous study (see Figure 36) and indicates the formation of particle clusters and small aggregates. The second color shift to violet/black is likely to be a result of GNP coalescence and the starting formation of a metal nanoshell.[189,199] The EDX mappings of single particles after each deposition stage (bottom row) provide a good visualization of the gradual GNP growth and, additionally, confirm the observations made by electron microscopy. Finally, EDX quantification of the expected elements (oxygen, zirconium, and gold) was carried out, the results are summarized in Table 7. As expected, a rather low gold fraction of 0.9 atom% is found for GNP-decorated zirconia particles, which translates into a weight fraction of 4.1 wt%. This is slightly higher than the value of 2.5 wt% obtained by AAS for the original sample in the previous study (see Figure 37). The

values are however in acceptable agreement in the light of the different analytic methods and the fact that the reproduction was also an up-scaled synthesis. After one and two cycles of gold deposition the gold fraction increased significantly to 4.0 and 9.0 atom%, respectively. The non-linear behavior is presumably due to the larger gold surface area that is available for reduction of additional gold in the second deposition cycle compared to the first one. Overall, the results are in excellent agreement with the findings from the diverse imaging methods presented in Figure 39. In summary, the results of this experimental series demonstrate the successful deposition of gold on zirconia particles by GNP immobilization and seeded growth.

6   Summary and Conclusion

In this dissertation several studies were presented focusing on the synthesis and characterization of sol-gel derived (doped) zirconia mesoparticles and the investigation of their microstructural behavior under thermal loading. Furthermore, the deposition of gold nanoshells and their morphological changes after ageing were reported, as well as a novel synthetic approach to prepare zirconia@gold composite mesoparticles. First, zirconia particles doped with 0 to 50 mol% alumina with similar particle sizes of $\sim$300 nm were successfully synthesized by the employment of eicosanoic acid and hydroxypropyl cellulose as stabilizing agents and adjustment of their mixing ratio and the total amount of stabilizer. The obtained particles were annealed at 800, 1000, and 1200 °C, and characterized with regard to crystal phase compositions and grain sizes. It was shown that alumina-doping effectively stabilizes the tetragonal/cubic zirconia phase and impedes the undesirable martensitic phase transformation to the monoclinic phase when annealed at 800 and 1000 °C, at least partly. Moreover, it was demonstrated that grain growth could be reduced by alumina-doping although the effect seems marginal and it could not be characterized in depth. Element mapping experiments revealed significant alumina segregation at the grain boundaries after annealing at 800 °C, suggesting that the observed phase stabilization may be caused by this inter-grain alumina layer due to impeded atomic diffusion and spatial constraint.

In a subsequent study, alumina/yttria-codoping of zirconia particles was examined in comparison with the respective alumina- and yttria-monodoped species with respect to synthesis conditions and thermal stability. Here, it was shown that codoping can be achieved easily with appropriate precursor mixtures. However, the control over the particle size proved to be challenging. Crystal phase analysis of particle samples annealed at 800, 1000, 1200, and 1400 °C indicated that codoping with alumina and yttria stabilizes the tetragonal zirconia phase similarly to yttria monodoping and substantially more effectively than alumina-doping. Analysis of the grain sizes after annealing also indicated a comparable behavior of alumina/yttria-codoped and yttria-monodoped zirconia particles. Only after annealing at 1400 °C, indications for an additional grain growth inhibiting effect by co-doping were observed.

A third study adressed the growth of gold nanoshells on silica mesospheres and the subsequent encapsulation with an outer silica nanoshell. It was shown that the use of ascorbic acid as reducing agent can yield a closed and homogeneous gold nanoshell and an outer silica shell is easily deposited on top of it by common sol-gel technique. Focused ion beam thinning of silica@gold@silica particles revealed substantial segregation and

delaminiation of gold and the formation of a camouflage structure. It could be demonstrated that this was an effect accompanying the ageing of such composite particles over the course of several months.

Finally, a novel approach to zirconia@gold composite particles, a new type of hybrid material, was presented. The proposed multi-step synthetic route is based on similar methods for the preparation of silica@gold particles, but needed substantial modification for applicability to the different ceramic particle material. It includes the immobilization of gold nanoparticles on calcined zirconia mesoparticles using the bifunctional linker aminomehtylphosphonic acid (AMPA) and acidification with hydrochloric acid in appropriate amounts. Here, it could be shown that a combination of 0.01 M HCl and 6 mM AMPA yielded effective and homogeneous coverage of the mesoparticle surface with gold nanoparticles, while lower or higher acidities led to poor immobilization efficiency or significant nanoparticle aggregation, respectively. Seeded growth of the surface-attached nanoscopic gold could be successfully achieved by careful and controlled reduction of ionic gold using ascorbic acid as reducing agent.

In conclusion, this work contributes to a better understanding of synthetic aspects governing the sol-gel synthesis of (doped) zirconia mesoparticles as well as the microstructural processes involved in their thermal stabilization. It sheds light on the effects of alumina-doping of zirconia particles, a yet neglected topic in this field, and revealed their potential relevance to the respective scientific community. The observations concerning ageing-induced delamination of gold nanoshells on silica nanospheres revealed a fundamental issue of limited stability of silica@gold particles, which will be relevant to the diverse potential applications for this kind of material. Lastly, the novel approach for the preparation of zirconia@gold composite particles provides a new synthetic tool and may benefit the design and development of functional materials, e.g., for optical metamaterials or composite catalysts, in future research.

7 Outlook

The results presented and discussed in the first part of this dissertation contribute to a deeper understanding of the syntheses of alumina-, yttria, and alumina/yttria-codoped mesoparticles and their structural behavior when annealed at high temperatures up to 1400 °C. The working temperature of next-generation TBCs is supposed to exceed 1500 °C in the near future.[248] Therefore, studying the thermal stability of such particle samples at higher temperatures will be of great importance with respect to their relevance for commercial TBCs. In order to gain more insights into the processes during annealing, in situ XRD experiments are desirable in future studies. Furthermore, the prepared particles have a non-ideal size and size distribution for the potential use in structural coloration. Therefore, additional efforts should be made to achieve narrower size distributions and to reduce the final particle size below 100 nm. Here, alternative synthesis routes should be considered, too. In the context of this potential application, an effective encapsulation with a different ceramic material is of interest. While previous studies have demonstrated the difficulty to encapsulate zirconia microparticles with an alumina shell,[55] it might be conceivable that such alumina encapsulation is facilitated by alumina-doping and segregation at grain boundaries, as reported in this dissertation. The successful encapsulation would pave the way for the use as building blocks for structural coloration or TBC materials. Therefore, the assembly of particles as photonic glasses as well as the subsequent characterization of the optical properties and thermal stability are of great scientific interest. Alumina/Yttria-codoping has not shown any additional phase stabilizing effect as opposed to conventional yttria-monodoping, but the results indicate a possible reduction of grain growth at 1400 °C. The respective data has not yet been confirmed, which will be necessary for reliable interpretation of this observation. In future experiments, this behavior could further be studied as a function of the dopant amount and after annealing at even higher temperatures. In the context of codoping, microstructural insights, e.g., by EDX mapping, are highly desirable.

The second part of this dissertation was dedicated to the controlled deposition of gold on silica and zirconia mesoparticles. The adaption of established synthesis protocols for SiO_2@Au core@shell particles yielded granular but closed gold nanoshells, which appeared to segregate over the course of months to form a camouflage structure. Here, a continuous monitoring of the segregation process by repeated characterization should provide valuable information about the process. Moreover, a comparison of the segregation tendency with other metal nanoshells, e.g, platinum, should be

conducted. This will be particularly relevant with respect to potential photonic applications, where a closed shell is crucial. Finally, a novel method for the synthesis of ZrO_2@Au composite particles using AMPA and HCl was reported. Here, further experiments should clarify the nature of the observed effects of AMPA and HCl on the immobilization of GNPs on the zirconia surface. Measurements concerning the zeta potentials of the involved particles seem particularly interesting in order to shed light on the electrostatic interactions governing this process. In order to fully understand the role of hydrochloric acid in this context, similar experiments using a different reagent for acidification should be performed for comparison. Furthermore, it should be examined whether a closed gold nanoshell can be obtained using this method. Therefore, additional deposition cycles and systematic adjustments to the synthetic parameters during deposition should be addressed. A more detailed investigation of the composite particle microstructure could be approached by FIB thinning and subsequent electron microscopic characterization. Moreover, experiments concerning the catalytic properties should be used to evaluate their suitability as a catalyst material. Here, a kinetic study using an easily measurable benchmark reaction, e.g., the photometric quantification of the reduction of 4-nitrophenol,[249] seems particularly promising. The comparison of particles obtained in the different stages of gold deposition might provide new information regarding a possible involvement of the ceramic support in the catalytic mechanism.

8 Experimental Section

8.1 Preparation

Materials

In moisture-sensitive procedures, the following anhydrous reagents were used: aluminum(III) *iso*-propoxide (99.99 %, ABCR), 1-butanol (99.5 %, ACROS Organics), ethanol absolute (99.5 %, ACROS Organics), 1-propanol (99.9 %, Alfa Aesar), yttrium(III) *iso*-propoxide (98 %, ABCR), zirconium(IV) *n*-propoxide (70 wt% in *n*-propanol, Alfa Aesar). The following reagents were used in all other preparation procedures: aminomethylphosphonic acid ($\geq$97 %, TCI Chemicals), 3-aminopropyl triethoxysilane (97 %, Sigma-Aldrich), ammonium hydroxide solution (28 wt%, VWR Chemicals), L-ascorbic acid (99 %, Alfa Aesar), 1-butanol (99.5 %, Th.Geyer), eicosanoic acid ($\geq$99.0 %, Sigma-Aldrich), ethanol absolute (99.8 %, VWR Chemicals), hydrogen tetrachloroaurate trihydrate (99.99 %, Alfa Aesar), hydrochloric acid (37 %, VWR Chemicals), hydroxypropyl cellulose (99 %, 20 mesh, $M_\mathrm{w} = 80\,000\,\mathrm{g\,mol^{-1}}$, Sigma-Aldrich), lithium metaborate (99.9 %, Sigma-Aldrich), magensium nitrate dihydrate solution (10 g Mg in 17 % nitric acid, Supelco), nitric acid solution (65 % in water, ACROS Organics), palladium nitrate trihydrate solution (10 % Pd in 10 % nitric acid, 99.999 % trace metals basis, Sigma-Aldrich), pH-indicator strips (MQuant 0-2.5, 2.5-4.5, 4.0-7.0, Merck), polyvinylpyrrolidone ($M_\mathrm{w} = 40\,000\,\mathrm{g\,mol^{-1}}$, Sigma-Aldrich), potassium carbonate (99.997 %, Alfa Aesar), sodium carbonate monohydrate ($\geq$99.5 %, Sigma-Aldrich), sodium hydroxide solution (0.1 M, Merck), sulfuric acid (96 %, Chemsolute), tetraethyl orthosilicate (99.99 %, Sigma-Aldrich), tetrahydrofuran (99.9 %, Sigma-Aldrich), tetrakis(hydroxymethyl) phosphonium chloride solution (80 % in water, Sigma-Aldrich), water (18.2 MΩ, $\leq$4 ppb TOC, ELGA PURELAB flex 2). Bottled nitrogen gas (99.999 %, Praxair) was utilized in the glove box for preparation, in the experimental procedures nitrogen gas produced from liquified nitrogen was used.

(Doped) Zirconia Particle Synthesis

The synthesis route for undoped and (co)doped zirconia mesoparticles is based on earlier protocols reported by Widoniak et al. and Leib et al.,[147,148] and was recently published.[143] Thereafter, a similar procedure was followed with varying amounts of reagents, different reaction times, and temperatures, which are summarized Table 8 and Table 9. First, the stabilizers (eicosanoic acid and hydroxypropyl cellulose) were dissolved in 45 mL anhydrous ethanol (135 mL for the sample 20Al-2) at 55 °C under

Table 8: Experimental parameters for the sol-gel syntheses of alumina-doped particles. The data correspond to the samples discussed in Section 5.1. Licensed under Creative Commons, reprinted from reference [143].

sample	Al-precursor / mg	Zr-precursor / mg	eicosanoic acid / mg	HPC / mg	water / µL	induction time / s
A0	-	1690	63.0	26.0	180	25 ± 3
A2	15	1650	56.0	23.4	190	120 ± 5
A4	29	1610	58.4	21.4	190	45 ± 3
A6	44	1580	55.8	23.6	190	25 ± 3
A10	73	1510	55.9	23.3	190	25 ± 3
A12	88	1480	55.7	23.4	190	25 ± 3
A14	104	1440	55.5	23.6	190	20 ± 2
A16	118	1410	53.7	24.3	190	15 ± 2
A18	132	1380	52.1	25.6	190	15 ± 2
A20	148	1340	52.0	25.1	190	15 ± 2
A30	220	1180	48.4	27.8	190	5 ± 1
A40	293	1010	44.7	30.3	190	5 ± 1
A50	366	830	28.2	40.5	190	3 ± 1

continuous magnetic stirring. Meanwhile, the respective alkoxide precursors, namely zirconium *n*-propoxide, aluminum *iso*-propoxide and/or yttrium *iso*-propoxide, were mixed with 5 to 8 mL anhydrous 1-propanol under nitrogen atmosphere using a glove box (MBraun Workstation MB 150B-G). While the precursor suspension was ultrasonicated (Bandelin, Sonorex Super RK 106) for 10 to 20 min, ultrapure water was added to the stabilizer solution. After ultrasonication, the clear precursor solution was transferred into a syringe and quickly injected into the stabilizer solution under vigorous stirring (550 rpm), thus initiating the reaction. The induction time, i.e., the duration from initiation to the first visible turbidity, was measured and the stirring speed was reduced to 250 rpm upon induction. Stirring at constant temperature was continued for 3 h. It should be noted that a different precursor batch was used for the sample A0 than for all other samples of this study. This required a significant adjustment of the stabilizer composition as well as the amount of water. As a consequence, the observed induction time showed a strong discrepancy from the other samples which must be considered when interpreting the results.

The obtained turbid suspensions were subsequently transferred into $\sim$45 mL ice-cooled 1-butanol in order to terminate the hydrolysis and condensation reactions followed by purification. For this purpose, the particles were separated from the solvent by centrifugation (10 000*g*, 4 min, 4 °C), decanting of the supernatant, and redispersion

Table 9: Experimental parameters for the sol-gel syntheses of alumina/yttria-(co)doped particles. The data correspond to the samples discussed in Section 5.2.

sample	Al-pre-cursor /mg	Y-pre-cursor /mg	Zr-pre-cursor /mg	eicosano-ic acid /mg	HPC /mg	water /µL	induction time /s
20A-1	151	-	1340	23.3	54.4	190	24 ± 3
20A-2	444	-	4027	68.5	161.5	570	27 ± 3
8Y	-	81	1577	24.9	52.2	210	95 ± 3
20Al8Y-1	148	80	1206	23.6	52.0	190	20 ± 3
20Al8Y-2	146	78	1207	47.3	30.2	170	10 ± 3

in ~25 mL ethanol, assisted by vortex agitation and ultrasonication. This step was repeated twice with reduced centrifugation speeds ($8000g$, $6000g$) and otherwise identical parameters. Finally, the purified particles were redispersed in ~10 mL ethanol. The glassware was freed from residues using concentrated sulfuric acid and washing with water before reuse. A reproduction of the sample A0 was used for the preparation of ZrO_2@Au composite particles (see Section 8.1).

Silica Particle Synthesis

The silica particles used in this dissertation were synthesized, characterized and provided by my predecessor Dr. Alexey Petrov (UHH). The particle sample used here has also previously been used in the context of his dissertation and an earlier publication of our group.[199,230] They were obtained by the Stöber method,[134] using the following protocol: 150 mL ethanol, 4.5 mL ultrapure water, and 20 mL ammonium hydroxide solution (28 wt%) were mixed in a 250 mL wide-mouth bottle and heated to 50 °C under continuous stirring under nitrogen gas atmosphere. Subsequently, 8.4 mL tetraethyl orthosilicate (TEOS) were added quickly. After 30 s, the mixture became slightly turbid, complete opacity was reached after 6 min. Stirring at 50 °C was continued for 16 h. Two seeded growth steps were performed by addition of 10 mL ultrapure water followed by 5 mL TEOS and continuous stirring at 50 °C for 24 h, respectively. The obtained particles were characterized by TEM, yielding an average diameter of 337 nm (±2.5 %).

Amino-Functionalization of Silica Particles

For the amino-functionalization, the sample was transferred into tetrahydrofuran (THF) by repeated centrifugation (6000g, 5 min, 5 °C), decanting of the supernatant, and resuspending in ethanol (2×) and THF (2×) by ultrasonication. After a final centrifugation step at the same conditions, the particles were redispersed in 160 mL THF by ultrasonication. Under continuous stirring, the mixture was heated to 60 °C under nitrogen atmosphere, followed by the addition of 7.5 mL 3-aminopropyl triethoxysilane (APTES). Stirring at constant temperature was continued for 16 h. Subsequently, the sample was purified by repeated centrifugation (6000g, 5 min, 5 °C), decanting of the supernatant, and redispersion in ethanol. After the final centrifugation step, the particles were redispersed in 180 mL ethanol. It was subsequently characterized by TEM, yielding an average diameter of 347 nm ($\pm$2.9 %). A concentration of 31 g L^{-1} was determined gravimetrically.

Gold Nanoparticle Synthesis

Small-sized gold nanoparticles (GNPs) were obtained using a protocol reported by Duff et al.[187] To this end, 45 mL ultrapure water and 3 mL sodium hydroxide solution (0.1 M) were mixed in a 100 mL wide-mouth bottle under continuous stirring at room temperature, followed by the addition of 8.9 µL tetrakis(hydroxymethyl)phosphonium chloride (THPC) solution (80 wt%). Under vigorous stirring, 2 mL of a freshly prepared chloroauric acid solution (1 wt%) was added rapidly. Within a few seconds, a color change from light yellow to dark brown was observed. Stirring of the mixture was continued for 30 min and the obtained solution was subsequently stored at 4 °C in the dark. The GNPs were characterized by TEM and UV/Vis spectroscopy.

GNP Immobilization on Amino-Functionalized Silica Particles

Immobilization of GNPs on the surface of amino-functionalized silica particles was achieved using a modification of the protocol by Oldenburg et al.[189] A bottle containing a complete as-obtained GNP batch was placed into an ultrasonic bath and 3.5 mL of the thoroughly redispersed silica particle suspension was quickly added. At the same time, ultrasonication was started and continued for 15 min. The mixture was subsequently stirred for 30 min and purified by repeated centrifugation (6000g, 5 min, 5 °C), decanting of the supernatant, and redispersion in ultrapure water. After the third centrifugation step, the particles were redispersed in 50 mL water and characterized by TEM.

Gold Nanoshell Deposition on GNP-decorated Silica Particles

Gold nanoshells were deposited on silica particles after immobilization of GNPs on the particle surface. The protocol is inspired by previously published methods.[198,199] First, a K-gold solution was prepared by dissolving 375 mg chloroauric acid and 600 mg potassium carbonate in 300 mL water, stirring for 1 h, and aging for 2 h at 4 °C in the dark. To the K-gold solution, 2.5 mL of the as-prepared suspension of GNP-decorated silica particles were added and the mixture was stirred 4 h at ambient temperature. Subsequently, it was cooled in an ice-bath and an ascorbic acid solution (40 mg in 5 mL water) was added under continuous stirring. After a period of extended stirring for 12 h, a small sample was taken and purified for TEM characterization by repeated centrifugation ($3000g$, 10 min, 0 °C), decanting of the supernatant, and redispersion in ethanol.

Silica Nanoshell Deposition on Silica@Gold Particles

The method for the deposition of an outer silica shell on silica@gold composite particles is based on a previously reported method for the preparation of silica@platinum@silica hybrid particles.[199] To the as-prepared SiO_2@Au particle suspension, 100 mL of a 5 wt% polyvinylpyrrolidone (PVP, $M_w = 40\,000\,\mathrm{g\,mol^{-1}}$) solution were added and mixed for 1 h by shaking. Excess PVP was separated by centrifugation ($2000g$, 10 min, 0 °C) and resuspension in 10 mL water. After addition of 56 mL ethanol and 1 mL ammonium hydroxide solution (28 wt%), 700 µL TEOS were added step-wise under continuous stirring, 100 µL every 30 min. The suspension was stirred for 72 h and subseqently purified by repeated centrifugation ($2000g$, 10 min, 0 °C), decanting of the supernatant, and redispersion in ethanol. After the last centrifugation cycle, the sample was resuspended in 15 mL ethanol and characterized by TEM. A small sample of this batch was used for FIB preparation and subsequent TEM analysis.

GNP Immobilization on Zirconia Particles

The preparation of zirconia@gold composite particles was published recently.[235] Prior to GNP immobilization, zirconia particles were dried for 4 h at 80 °C (Heraeus Vacutherm VT) and atmospheric pressure. Then, the sample was calcined at 600 °C for 3 h in a muffle oven (Nabertherm L9/SKM) in order to remove residual organics and complete densification of the particles. A suspension was prepared by homogenizing 170 mg of the calcined particles using an agate mortar and redispersion in 10 mL water using ultrasonication. GNP immobilization was conducted at varying HCl concentrations and

Table 10: Experimental parameters for GNP immobilization. The data correspond to the samples discussed in Section 5.4. Licensed under Creative Commons, reprinted from reference [235].

sample	c_{AMPA} / mM	c_{HCl} / M	pH
0	-	1	0.0
0A	6	1	0.0
1	-	0.1	1.0
1A	6	0.1	1.0
2	-	0.01	2.5
2A	6	0.01	2.2
3	-	10^{-3}	3.6
3A	6	10^{-3}	3.3
4	-	10^{-4}	4.4
4A	6	10^{-4}	3.6
5	-	10^{-5}	5.5
5A	6	10^{-5}	4.2
6	-	10^{-6}	6.1
6A	6	10^{-6}	4.7
7	-	-	6.5
7A	6	-	4.7

in presence or absence of aminomethylphosphonic acid (AMPA) (6 mM), as summarized in Table 10. First, a GNP sol was prepared by the Duff method as described above. For every sample, 1 mL of the as-obtained GNP sol was mixed with 100 mL of the readily redispersed aqueous suspension of calcinated zirconia particles under continuous stirring. Subsequently, the aqueous AMPA solution (1 wt%), ultrapure water, and hydrochloric acid (37 wt%) were added in the appropriate amounts to obtain a final volume of 1.5 mL for all samples with the reagent concentrations specified in Table 10. Stirring was continued for 30 min, after which the particle samples were purified by repeated centrifugation (10 000g, 5 min, ambient temperature), decanting of the supernatant, and redispersion in water. The pH was determined for each sample from the supernatant of the first centrifugation using pH indicator strips (MQuant 0-2.5, 2.5-4.5, 4.0-7.0; Merck). The obtained particles were characterized by SEM, AAS, and UV/vis spectroscopy. A scaled-up reproduction (factor 20) of the sample 2A was prepared analogously. This sample was characterized by SEM, AAS, gravimetry, TEM, and STEM/EDX mapping and subsequently used for the deposition of additional gold by seeded reduction as described in the following paragraph.
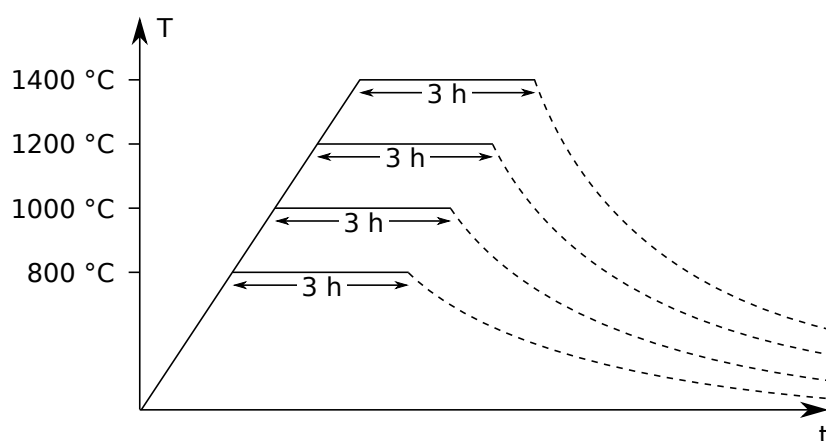
Figure 40: Schematic representation of temperature programs for annealing experiments.
Particle samples were annealed in alumina crucibles and heated with a constant rate of $5\,°C\,min^{-1}$
to the target temperature ($800\,°C$, $1000\,°C$, $1200\,°C$, or $1400\,°C$). The target temperature was held
constant for $3\,h$ and subsequently the samples were allowed to cool down to room temperature at
cooling rates of $\leq 5\,°C$.

Seeded Growth Gold Deposition on Zirconia Particles

Additional gold was deposited on GNP-decorated zirconia particles by seeded reduction
as published recently.[235] Therefore, a K-gold solution was prepared by mixing $17.2\,mg$
chloroauric acid trihydrade, $28.4\,mg$ potassium carbonate, and $226\,mL$ ultrapure water.
The solution was stirred for $30\,min$ and aged for $24\,h$ at $4\,°C$ in the dark. For every
gold deposition cycle, $5\,µL$ of a freshly prepared $0.1\,M$ L-ascorbic acid solution were
added to $800\,µL$ water, followed by addition of $200\,µL$ of the purified suspension
of GNP-decorated zirconia mesoparticles and continued stirring for $15\,min$. Under
continuous stirring, $500\,µL$ of the previously prepared K-gold solution were added
dropwise at a constant rate of $0.3\,mL\,h^{-1}$ using a syringe pump. After extended stirring
for $1\,h$, purification was conducted by repeated centrifugation ($10\,000g$, $10\,min$, ambient
temperature), decanting of the supernatant, and redispersion in water. The sample
was finally redispersed in $200\,µL$ water, characterized by SEM, AAS, gravimetry, TEM,
and STEM/EDX mapping.

Annealing Experiments

High-temperature annealing experiments were carried out based on the works of Leib
et al.[8,148,165] and as published recently.[143] All particle samples were dried prior to
the annealings. For this purpose, the solvent was evaporated at room temperature
and ambient pressure in a first step. Afterwards, the obtained solids were dried in an

oven (Heraeus Vacutherm VT) at 80 °C and atmospheric pressure for 4 h. The dry and densified samples were then carefully ground to form a powder, using an agate mortar. For every annealing experiment, $\sim$30 mg of a particle powder sample was placed into an alumina crucible and heated to either of the target temperatures (800 °C, 1000 °C, 1200 °C, 1400 °C, or 1500 °C). The temperature programs with a fixed heating rate of 5 °C min^{-1}, a static heating period of 3 h and passive cooling rates of $\leq$5 °C min^{-1} are illustrated in Figure 40 . Annealings at temperatures up to 1000 °C were performed in a muffle oven (Nabertherm L9/SKM), for higher temperatures a tube furnace (Carbolite SFT16/180) was used. Annealed particle samples were carefully ground using an agate mortar and redispersed in ethanol, assisted by vortex agitation and ultrasonication, prior to subsequent characterization.

Focused Ion Beam Preparation

FIB preparation of alumina-doped zirconia particles was carried out by my colleague and collaborator Dr. Tobias Krekeler at the TUHH. FIB preparation of SiO_2@Au@SiO_2 composite particles was performed by Mr. Andreas Kornowski. Thin lamellae of selected particle samples were prepared using focused ion beam thinning (FEI Helios G3 UC). To this end, single particles were initially covered generously with platinum via ion-deposition. Then, a lamella was formed using an electron beam. The lamella was extracted using a common lift-out technique and fixed to a copper lift-out grid. Thinning to a final lamella thickness of $\sim$100 nm was achieved using a 80 pA 30 kV Ga$^+$-beam in a cross-section cleaning pattern. For final polishing of the surface a 15 pA 5 kV Ga$^+$-beam was used.

8.2 Characterization

Inductively-Coupled Plasma - Optical Emission Spectroscopy (ICP-OES)

ICP-OES was used for quantitative elemental analysis of (co-)doped zirconia mesoparticles. For this purpose, particle samples were solubilized using an optimized fusion protocol:[250] 10 mg of a dried particle sample were transferred into a platinum crucible and 150 mg of a sodium/potassium carbonate (1:1) mixture and 150 mg lithium metaborate were added. The powder was homogenized and annealed in a bunsen burner flame and subsequently in a muffle oven at 1000 °C. After cooling to ambient temperature, 5 mL nitric acid (8 %) were added and volumized to 50 mL with demineralized water. This solution was diluted (factor 4 or 5) prior to the measurement. The instrument

(Spectro Acros) was background corrected and calibrated using matrix-adjusted calibration solutions. Aluminum was quantified using the signals at 257.139 nm, 272.262 nm, 339.198 nm, and 343.823 nm. For zirconium the signals at 176.641 nm, 308.215 nm, 309.271 nm, 394.401 nm, and 396.150 nm were used. For every sample, a minimum of two determinations were performed and the obtained values were averaged.

Atomic Absorption Spectroscopy (AAS)

AAS was conducted for quantification of the gold weight fraction of GNP-decorated zirconia and zirconia@gold composite particle samples. Therefore, 250 µL of each specimen were dried, weighed and solubilized using an aqua regia fusion. After the addition of 4.00 mL aqua regia (caution: hazardous reagent!) the mixture was boiled for 1 h and left to cool for 15 min. Subsequently, it was volumized to 25.0 mL using demineralized water and the solution was diluted three times by a factor of 10 prior to the measurements. A graphite tube AAS instrument (Analytik Jena, ContrAA 700) was used and calibrated in the range of 5.00 to 40.0 µg L^{-1}. As matrix modifier, 5 µL of a palladium/magnesium nitrate solution (0.1 %/0.05 %) were employed. For signal quantification, a wavelength of 242.7 nm was used. For each sample, double determinations were performed the results were averaged.

Transmission Electron Microscopy (TEM)

TEM was used predominantly for the determination of particle sizes and examination of particle morphologies. The specimens were prepared from readily mixed particle suspensions by drop-casting a volume of 10 µL onto a carbon-coated copper grid. After drying at ambient conditions, TEM analysis (Jeol JEM-1011 HRTEM) was performed in ultrahigh vacuum ($<5 \times 10^{-7}$ mbar) at an acceleration voltage of 100 kV. Particle size statistics were determined using the software ImageJ 1.52a. For samples discussed in Section 5.1, particle diameters were collected manually using binarized TEM images by drawing vertically centered horizontal edge-to-edge lines and measuring the lengths. For all other samples, particle diameters were obtained by automated analysis of the particle cross-sections using binarized TEM images and calculated from the projection area assuming a perfectly circular shape. For each sample, a minimum number of 100 particles were used for the size statistics. Average thicknesses of gold nanoshells were determined by the increase of the mean diameter compared to the bare core particles. Silica shell thicknesses were obtained by measuring the radial distance from the dark metal shell offset to the particle surface.

Energy-Dispersive X-Ray Spectroscopy (EDX)

Standard EDX analysis of (co-)doped zirconia mesoparticles was performed using a transmission electron microscope (Philips HT-TEM CM 300), equipped with an EDX detector and operating at $200\,\text{kV}$ in ultrahigh vacuum. For signal detection, a selected area containing one or a few particles was analyzed using an appropriate aperture. For quantification, the lines at $2.042\,\text{keV}$ (Zr L_α), $1.486\,\text{keV}$ (Al K_α), $1.922\,\text{keV}$ (Y L_α), and $0.525\,\text{keV}$ (O K_α) were used.

Scanning Electron Microscopy (SEM)

SEM analysis was primarily used for the investigation of particle morphologies and microstructures. The instrument (Carl Zeiss GEMINI LEO 1550 HRSEM) was equipped with a LaB_6 emitter and an in-lens detector as well as an energy-selective backscatter (ESB) detector. It was operated at an acceleration voltage of 2 to $5\,\text{kV}$ and a vacuum level of $<10^{-6}\,\text{mbar}$. SEM specimens were prepared by drop-casting $30\,\text{µL}$ of a readily redispersed particle suspension onto a polished silicon wafer piece.

EDX Mapping and Scanning Transmission Electron Microscopy (STEM)

STEM/EDX mapping of FIB-lamellae of alumina-doped zirconia particles was carried out by Dr. Tobias Krekeler using a FEI Talos F200X equipped with a Super-X EDS detector. The beam current was set to $1\,\text{nA}$ at $200\,\text{kV}$. The selected sample areas were scanned with a pixel size of $387\,\text{pm}$ resulting in a horizontal field width of $198\,\text{nm}$. X-rays were collected in an energy range of 0 to $20\,\text{keV}$ with a dispersion of $5\,\text{eV}$ per channel, a dwell time of $10\,\text{µs}$ per pixel and a frame time of $3.4\,\text{s}$. The overall count numbers and total measurement times were 8458 and $16\,\text{h}$ for the as-prepared particle sample, and 4142 and $4\,\text{h}$ for the annealed particle sample, respectively. For the latter, elemental maps were averaged with a 3×3 px box filter for enhanced contrast. Quantification was performed assuming no absorption and applying a Brown-Powell ionization cross-section model in FEI Velox Software. The signal intensities at $1.4875\,\text{keV}$ (Al $\text{K}_{\alpha1}$), $15.7749\,\text{keV}$ (Zr $\text{K}_{\alpha1}$), and $0.524\,\text{keV}$ (O $\text{K}_{\alpha1}$) were used for quantification. STEM/EDX mapping of zirconia@gold composite particles was conducted by Mr Andreas Kornowski using the $\text{K}_{\alpha1}$ signals for oxygen and zirconium and the $\text{L}_{\alpha1}$ signal for gold.

X-Ray Diffraction (XRD)

XRD powder diffractograms of annealed zirconia particle samples were collected using a Philips PANalytical X'Pert PRO MPD. Samples were ground carefully using an agate mortar, thoroughly resuspended in ethanol using ultrasonication and drop-casted onto a Si(911)-single crystal XRD substrate. Prior to measurements, the solvent was allowed to evaporate completely at ambient conditions. Diffractograms were collected in the 2θ range between 10° and 80° or 10° and 90°, with a step size of 0.033° and a time per step of 75 s. Data evaluation was conducted using the software Maud 2.78(1.0).[251] As-collected diffractograms were background corrected and refined using crystallographic information for monoclinic (ICSD 62993), tetragonal (ICSD 62994), and cubic zirconia (ICSD 62995), as well as α-alumina (COD 1000032).[69,251] The crystallographic information was adjusted to the estimated dopant content regarding atom types and occupation ratios, prior to refinement. Instrumental broadening parameters were determined using a LaB_6 standard (NIST 660a) and hence used for all refinements.

Ultraviolet/Visible Spectroscopy (UV/vis)

Due to significant scattering of ceramic mesoparticle suspensions, optical spectroscopy (Varian Cary 5000) was conducted in diffuse reflection mode using an integrated sphere accessory (Ulbricht sphere). For this purpose, 1.5 mL of each sample were transferred into a standard quartz cuvette (10 mm path length), which was positioned in the center of the sphere and absorption was measured. Spectra were corrected for a baseline, recorded using 1.5 mL water. Prior to measurements, samples were readily redispersed. The analyzed optical ranged from 300 to 1100 nm at a step size of 1 nm.

Bibliography

[1]   BP, Natural Gas, **2018**, `https://www.bp.com/en/global/corporate/` `energy-economics/energy-outlook/demand-by-fuel/natural-gas.html` (visited on July 26, 2020).

[2]   B. Dudley, BP Statistical Review of World Energy, **2018**, `https://www.bp.` `com/en/global/corporate/energy-economics/statistical-review-of-` `world-energy.html` (visited on July 26, 2020).

[3]   International Air Transport Association, 20-Year Passenger Forecast 2017, `https` `://www.iata.org/en/publications/store/20-year-passenger-forecast/` (visited on Mar. 26, 2020).

[4]   A. Mazurkiewicz, J. Smolik, *Archives of Metallurgy and Materials* **2015**, *60*, 2161–2172.

[5]   N. P. Padture, M. Gell, E. H. Jordan, *Science* **2002**, *296*, 280–284.

[6]   R. Vaßen, M. O. Jarligo, T. Steinke, D. E. Mack, D. Stöver, *Surface and Coatings Technology* **2010**, *205*, 938–942.

[7]   V. Shklover, L. Braginsky, G. Witz, M. Mishkirey, C. Hafner, *Journal of Computational and Theoretical Nanoscience* **2008**, *5*, 1–32.

[8]   E. W. Leib, R. M. Pasquarelli, J. J. do Rosário, P. N. Dyachenko, S. Döring, A. Puchert, A. Y. Petrov, M. Eich, G. A. Schneider, R. Janssen, H. Weller, T. Vossmeyer, *Journal of Materials Chemistry C* **2016**, *4*, 62–74.

[9]   P. N. Dyachenko, J. J. Do Rosário, E. W. Leib, A. Y. Petrov, R. Kubrin, G. A. Schneider, H. Weller, T. Vossmeyer, M. Eich, *ACS Photonics* **2014**, *1*, 1127–1133.

[10] H. Zollinger, *Color Chemistry: Synthesis, Properties and Applications of Organic Dyes and Pigments*, Second Edition, WILEY-VCH, Weinheim, **1991**.

[11] T. Bechtold, R. Mussak, *Handbook of Natural Colorants*, John Wiley & Sons Ltd., Hoboken, NJ, **2009**.

[12] M. Jansen, H. P. Letschert, *Letters To Nature* **2000**, *404*, 980–982.

[13] F. Wang, X. Zhang, Y. Lin, L. Wang, J. Zhu, *ACS Applied Materials and Interfaces* **2016**, *8*, 5009–5016.

[14] Y. Häntsch, G. Shang, A. Petrov, M. Eich, G. A. Schneider, *Advanced Optical Materials* **2019**, *7*, 1–8.

[15] S. Magkiriadou, J. G. Park, Y. S. Kim, V. N. Manoharan, *Physical Review E - Statistical Nonlinear and Soft Matter Physics* **2014**, *90*, 1–8.

[16] Y. Zhao, Z. Xie, H. Gu, C. Zhu, Z. Gu, *Chemical Society Reviews* **2012**, *41*, 3297–3317.

[17] Joefrei, Common kingfisher, licensed under CC BY-SA 3.0, `https://upload.` `wikimedia.org/wikipedia/commons/a/a6/Ein_Eisvogel_im_Schwebflug.` `jpg` (visited on July 26, 2020).

[18] Izzy LeCours, Morpho peleides, licensed under CC BY, `http://tierdoku.de/index.php?title=Bild:Morpho-peleides-1624.jpg` (visited on July 23, 2020).

[19] Danmekis, Giant Black Opal, licensed under CC BY-SA 3.0, `https://commons.wikimedia.org/wiki/File:Black_Opal_from_Red_Carpet_Opals.JPG` (visited on July 26, 2020).

[20] R. C. Schroden, M. Al-Daous, C. F. Blanford, A. Stein, *Chemistry of Materials* **2002**, *14*, 3305–3315.

[21] P. Bueno, K. P. Furlan, D. Hotza, R. Janssen, *Journal of the American Ceramic Society* **2018**, *102*, 686–694.

[22] G. Shang, L. Maiwald, H. Renner, D. Jalas, M. Dosta, S. Heinrich, A. Petrov, M. Eich, *Scientific Reports* **2018**, *8*, 1–9.

[23] M. Finsel, M. Hemme, S. Döring, J. S. V. Rüter, G. T. Dahl, T. Krekeler, A. Kornowski, M. Ritter, H. Weller, T. Vossmeyer, *RSC Advances* **2019**, *9*, 26902–26914.

[24] H. Ritchie, M. Roser, Renewable Energy, licensed under CC BY, **2017**, `https://ourworldindata.org/renewable-energy/` (visited on July 26, 2020).

[25] L. C. Andreani, A. Bozzola, P. Kowalczewski, M. Liscidini, L. Redorici, *Advances in Physics: X* **2019**, *4*, 1548305.

[26] T. J. Coutts, M. C. Fitzgerald, *Scientific American* **1998**, *279*, 90–95.

[27] T. J. Coutts, *Solar Energy Materials and Solar Cells* **2001**, *66*, 443–452.

[28] R. E. Nelson, *Semiconductor Science and Technology* **2003**, *18*, S141–S143.

[29] N.-P. Harder, P. Würfel, *Semiconductor Science and Technology* **2003**, *18*, S151–S157.

[30] A. Lenert, D. M. Bierman, Y. Nam, W. R. Chan, I. Celanović, M. Soljačić, E. N. Wang, *Nature Nanotechnology* **2014**, *9*, 126–130.

[31] A. Licht, N. Pfiester, D. DeMeo, J. Chivers, T. E. Vandervelde, *MRS Advances* **2019**, *4*, 2271–2282.

[32] N. A. Pfiester, T. E. Vandervelde, *Physica Status Solidi (A) Applications and Materials Science* **2017**, *214*, 1–24.

[33] R. Sakakibara, V. Stelmakh, W. R. Chan, M. Ghebrebrhan, J. D. Joannopoulos, M. Soljačić, I. Čelanović, *Journal of Photonics for Energy* **2019**, *9*, 1.

[34] C. J. Crowley, N. A. Elkouh, P. J. Magari in AIP Conference Proceedings, *Vol. 460*, **2011**, p. 197.

[35] V. Rinnerbauer, S. Ndao, Y. X. Yeng, W. R. Chan, J. J. Senkevich, J. D. Joannopoulos, M. Soljačić, I. Celanovic, *Energy and Environmental Science* **2012**, *5*, 8815–8823.

[36] P. N. Dyachenko, A. Y. Petrov, M. Eich, *Applied Physics Letters* **2013**, *103*, 211105.

[37] C. Shemelya, D. Demeo, N. P. Latham, X. Wu, C. Bingham, W. Padilla, T. E. Vandervelde, *Applied Physics Letters* **2014**, *104*, 201113.

[38] P. N. Dyachenko, J. J. do Rosário, E. W. Leib, A. Y. Petrov, M. Störmer, H. Weller, T. Vossmeyer, G. A. Schneider, M. Eich, *Optics Express* **2015**, *23*, A1236.

[39] Z. Zhou, O. Yehia, P. Bermel, *Journal of Nanophotonics* **2016**, *10*, 016014.

[40] H. Knözinger, *Heterogeneous Catalysts and Catalytic Processes*, Springer, Boston, MA, **1991**, pp. 7–25.

[41] B. Cornils, *Catalysis from A to Z*, WILEY-VCH Verlag, Weinheim, **2013**.

[42] G. Ertl, H. Knozinger, J. Weitkamp, *Environmental Catalysis*, John Wiley & Sons Ltd., Hoboken, NJ, **2008**.

[43] W. Reschetilowski, *Einführung in die Heterogene Katalyse*, Springer, Berlin/ Heidelberg, **2015**, pp. 1–277.

[44] Syrris Ltd., Solid phase catalysis in continuous flow, `https://blog.syrris.com/2018/06/22/solid-phase-catalysis-in-continuous-flow/` (visited on Apr. 1, 2020).

[45] H. H. Kung, M. C. Kung, *Catalysis Today* **2004**, *97*, 219–224.

[46] S. B. A. Hamid, R. Schlögl in *The Nano-Micro Interface*, John Wiley & Sons Ltd., Hoboken, NJ, **2015**, Chapter 20, pp. 405–430.

[47] M. Guazzato, M. Albakry, S. P. Ringer, M. V. Swain, *Dental Materials* **2004**, *20*, 449–456.

[48] B. J. McEntire, B. S. Bal, M. N. Rahaman, J. Chevalier, G. Pezzotti, *Journal of the European Ceramic Society* **2015**, *35*, 4327–4369.

[49] A. K. Mishra, *Sol-gel based nanoceramic materials: Preparation, properties and applications*, Springer International Publishing, Basel, **2016**.

[50] I. J. Shon, J. K. Yoon, K. T. Hong, *Metals and Materials International* **2017**, *23*, 940–947.

[51] A. Persson, V. Lekholm, G. Thornell, L. Klintberg, *Applied Physics Letters* **2015**, *106*, 194103.

[52] H. Cai, R. Sun, X. Yang, X. Liang, C. Wang, P. Sun, F. Liu, C. Zhao, Y. Sun, G. Lu, *Ceramics International* **2016**, *42*, 12503–12507.

[53] D. Mæland, C. Suciu, I. Wærnhus, A. C. Hoffmann, *Journal of the European Ceramic Society* **2009**, *29*, 2537–2547.

[54] N. Mahato, A. Gupta, K. Balani, *Nanomaterials and Energy* **2012**, *1*, 27–45.

[55] M. Finsel, Dissertation, Universität Hamburg, **2019**.

[56] R. H. J. Hannink, M. V. Swain, *Annual Review of Materials Science* **1994**, *24*, 359–408.

[57] P. G. Klemens in Thermal conductivity, *Vol. 23*, **1996**, pp. 209–220.

[58] A. Slifka, B. Filla, J. Phelps, G. Bancke, C. Berndt, *Journal of Thermal Spray Technology* **1998**, *7*, 43–46.

[59] K. W. Schlichting, N. P. Padture, P. G. Klemens, *Journal of Materials Science* **2001**, *36*, 3003–3010.

[60] B. Liang, C. Ding, *Surface and Coatings Technology* **2005**, *197*, 185–192.

[61] R. E. Latta, E. C. Duderstadt, R. E. Fryxell, *Journal of Nuclear Materials* **1970**, *35*, 345–346.

[62] D. R. Clarke, C. G. Levi, *Annual Review of Materials Research* **2003**, *33*, 383–417.

[63] B. Yan, C. V. McNeff, F. Chen, P. W. Carr, A. V. McCormick, *Journal of the American Ceramic Society* **2001**, *84*, 1721–1727.

[64] A. A. Ashkarran, S. A. A. Afshar, S. M. Aghigh, M. Kavianipour, *Polyhedron* **2010**, *29*, 1370–1374.

[65] J. He, J. Chen, L. Ren, Y. Wang, C. Teng, M. Hong, J. Zhao, B. Jiang, *ACS Applied Materials and Interfaces* **2014**, *6*, 2718–2725.

[66] J. Chevalier, *Biomaterials* **2006**, *27*, 535–543.

[67] J. R. Kelly, I. Denry, *Dental Materials* **2008**, *24*, 289–298.

[68] R. H. J. Hannink, P. M. Kelly, B. C. Muddle, *Journal of the American Ceramic Society* **2000**, *83*, 461–487.

[69] C. J. Howard, R. J. Hill, B. E. Reichert, *Acta Crystallographica Section B* **1988**, *44*, 116–120.

[70] F. F. Lange, *Journal of Materials Science* **1982**, *17*, 225–234.

[71] A. Navrotsky, *Journal of Materials Chemistry* **2005**, *15*, 1883–1890.

[72] J. E. Bailey, D. Lewis, Z. M. Librant, L. J. Porter, *Journal of the British Ceramic Society* **1972**, *71*, 25–30.

[73] T. Mitsuhashi, M. Ichihara, U. Tatsuke, *Journal of the American Ceramic Society* **1974**, *57*, 97–101.

[74] R. C. Garvie, M. F. Goss, *Journal of Materials Science* **1986**, *21*, 1253–1257.

[75] T. Chraska, A. H. King, C. C. Berndt, *Materials Science and Engineering A* **2000**, *286*, 169–178.

[76] S. Shukla, S. Seal, *Journal of Physical Chemistry B* **2004**, *108*, 3395–3399.

[77] M. W. Pitcher, S. V. Ushakov, A. Navrotsky, B. F. Woodfield, G. Li, J. Boerio-Goates, B. M. Tissue, *Journal of the American Ceramic Society* **2005**, *88*, 160–167.

[78] P. Scherrer in *Nachrichten von der Gesellschaft der Wissenschaften zu Göttingen, Mathematisch-Physikalische Klasse*, Weidmannsche Buchhandlung, Berlin, **1918**, pp. 98–100.

[79] H. M. Rietveld, *Journal of Applied Crystallography* **1969**, *2*, 65–71.

[80] M. N. Rahaman, *Ceramic Srocessing and Sintering*, Second Edition, CRC Press, Boca Raton, FL, **2017**.

[81] Y. M. Chiang, D. P. Birnie, W. D. Kingery, John Wiley & Sons Ltd., Hoboken, NJ, **1996**.

[82] S. A. Ostanin, E. I. Salamatov, *JETP Letters* **2001**, *74*, 552–555.

[83] P. Li, I. W. Chen, J. E. Penner-Hahn, *Physical Review B* **1993**, *48*, 10074–10081.

[84] G. Stapper, M. Bernasconi, N. Nicoloso, M. Parrinello, *Physical Review B - Condensed Matter and Materials Physics* **1999**, *59*, 797–810.

[85] S. Fabris, A. T. Paxton, M. W. Finnis, *Acta Materialia* **2002**, *50*, 5171–5178.

[86] P. S. Manning, J. D. Sirman, R. A. De Souza, J. A. Kilner, *Solid State Ionics* **1997**, *100*, 1–10.

[87] J. Molina-Reyes, H. Tiznado, G. Soto, M. Vargas-Bautista, D. Dominguez, E. Murillo, D. Sweeney, J. Read, *Journal of Materials Science: Materials in Electronics* **2018**, *29*, 15349–15357.

[88] G. Witz, V. Shklover, W. Steurer, S. Bachegowda, H. P. Bossmann, *Journal of the American Ceramic Society* **2007**, *90*, 2935–2940.

[89] S.-L. Hwang, I. W. Chen, *Journal of the American Ceramic Society* **1990**, *73*, 3269–3277.

[90] J. A. Allemann, B. Michel, H. B. Märki, L. J. Gauckler, E. M. Moser, *Journal of the European Ceramic Society* **1995**, *15*, 951–958.

[91] J. Frenkel, *Kinetic Theory of Liquids*, University Press, New York, **1946**, p. 36.

[92] W. D. Kingery, *Journal of the American Ceramic Society* **1974**, *57*, 1–12.

[93] W. D. Kingery, *Journal of the American Ceramic Society* **1974**, *57*, 74–83.

[94] E. W. Leib, Dissertation, Universität Hamburg, **2016**.

[95] I. W. Chen, *Materials Science and Engineering A* **1993**, *166*, 51–58.

[96] N. Claussen, *Journal of the American Ceramic Society* **1976**, *59*, 49–51.

[97] N. Claussen, *Journal of the American Ceramic Society* **1978**, *61*, 85–86.

[98] F. F. Lange, *Journal of Materials Science* **1982**, *17*, 247–254.

[99] K. Tsukuma, K. Ueda, M. Shimada, *Journal of the American Ceramic Society* **1985**, *68*, C-4–C-5.

[100] S. Rajendran, J. Drennan, S. P. S. Badwal, *Journal of Materials Science Letters* **1987**, *6*, 1431–1434.

[101] S. Rajendran, *Journal of Materials Science* **1992**, *27*, 433–440.

[102] M. A. Stough, J. R. Hellmann, *Journal of the American Ceramic Society* **2002**, *85*, 2895–2902.

[103] T. Chraska, K. Neufuss, J. Dubský, P. Ctibor, P. Rohan, *Ceramics International* **2008**, *34*, 1229–1236.

[104] K. Ishida, K. Hirota, O. Yamaguchi, H. Kume, S. Inamura, H. Miyamoto, *Journal of the American Ceramic Society* **1994**, *77*, 1391–1395.

[105] A. Nazeri, S. B. Qadri, *Surface and CoatingsTechnology* **1996**, *86-87*, 166–169.

[106] T. Klimova, M. L. Rojas, P. Castillo, R. Cuevas, J. Ramírez, *Microporous and Mesoporous Materials* **1998**, *20*, 293–306.

[107] V. V. Srdić, M. Winterer, H. Hahn, *Journal of the American Ceramic Society* **2000**, *83*, 1853–1860.

[108] M. L. Balmer, H. Eckert, N. Das, F. F. Lange, *Journal of the American Ceramic Society* **1996**, *79*, 321–326.

[109] K. Matsui, N. Ohmichi, M. Ohgai, H. Yoshida, Y. Ikuhara, *Journal of Materials Research* **2006**, *21*, 2278–2289.

[110] A. Keyvani, M. Saremi, M. H. Sohi, *Journal of Alloys and Compounds* **2011**, *509*, 8370–8377.

[111] C. Zhu, A. Javed, P. Li, F. Yang, G. Y. Liang, P. Xiao, *Surface and Coatings Technology* **2012**, *212*, 214–222.

[112] W. H. Rhodes, *Journal of the American Ceramic Society* **1981**, *64*, 19–22.

[113] K. S. Mazdiyasni, *Ceramics International* **1982**, *8*, 42–56.

[114] B. Fegley Jr, E. A. Barringer in Better Ceramics Through Chemistry, *Vol. 32*, **1984**, pp. 187–197.

[115] Clarivate Web of Science, InCites Journal Citation Reports (accessed on Apr. 9, 2020), search for "zirconia particle synthesis" in title.

[116] E. Matijević, A. Bell, R. Brace, P. McFadyen, *Journal of The Electrochemical Society* **1973**, *120*, 893–899.

[117] E. Matijević, *Accounts of Chemical Research* **1981**, *14*, 22–29.

[118] M. A. Blesa, A. J. Maroto, S. I. Passaggio, N. E. Figliolia, G. Rigotti, *Journal of Materials Science* **1985**, *20*, 4601–4609.

[119] M. Déchamps, B. Djuriçić, S. Pickering, *Journal of the American Chemical Society* **1995**, *78*, 2873–2880.

[120] K. Matsui, H. Suzuki, M. Ohgai, H. Arashi, *Journal of the American Ceramic Society* **1995**, *78*, 146–152.

[121] A. Singhal, L. M. Toth, J. S. Lin, K. Affholter, *Journal of the American Chemical Society* **1996**, *118*, 11529–11534.

[122] K. Lee, A. Sathyagal, P. W. Carr, A. V. McCormick, *Journal of the American Ceramic Society* **1999**, *82*, 338–342.

[123] Y. T. Moon, H. K. Park, D. K. Kim, C. H. Kim, *Journal of the American Ceramic Society* **1995**, *78*, 2690–2694.

[124] Y. T. Moon, D. K. Kim, C. H. Kim, *Journal of the American Ceramic Society* **1995**, *78*, 1103–1106.

[125] S.-C. Zhang, G. L. Messing, M. Borden, *Journal of the American Ceramic Society* **1990**, *73*, 61–67.

[126] Y. L. Song, S. C. Tsai, C. Y. Chen, T. K. Tseng, C. S. Tsai, J. W. Chen, Y. D. Yao, *Journal of the American Ceramic Society* **2004**, *87*, 1864–1871.

[127] H. Yang, J. Ouyang, X. Zhang, N. Wang, C. Du, *Journal of Alloys and Compounds* **2008**, *458*, 474–478.

[128] H. Uchiyama, K. Takagi, H. Kozuka, *Colloids and Surfaces A: Physicochemical and Engineering Aspects* **2012**, *403*, 121–128.

[129] D. G. Shchukin, R. A. Caruso, *Chemistry of Materials* **2004**, *16*, 2287–2292.

[130] A. Pattanayak, A. Subramanian, *Powder Technology* **2009**, *192*, 359–366.

[131] R. A. Shalliker, G. K. Douglas, *Journal of Liquid Chromatography and Related Technologies* **1997**, *20*, 1651–1666.

[132] C. Verissimo, O. L. Alves, *Journal of the American Ceramic Society* **2006**, *89*, 2226–2231.

[133] J. H. Schattka, E. H. Wong, M. Antonietti, R. A. Caruso, *Journal of Materials Chemistry* **2006**, *16*, 1414–1420.

[134] W. Stöber, A. Fink, E. Bohn, *Journal of Colloid and Interface Science* **1968**, *26*, 62–69.

[135] E. a. Barringer, H. K. Bowen, *Journal of the American Ceramic Society* **1982**, *65*, C-199–C-201.

[136] B. Fegley, P. White, H. K. Bowen, *Journal of the American Ceramic Society* **1985**, *68*, C60–C62.

[137] K. Uchiyama, T. Ogihara, T. Ikemoto, N. Mizutani, M. Kato, *Journal of Materials Science* **1987**, *22*, 4343–4347.

[138] T. Ogihara, N. Mizutani, M. Kato, *Journal of the American Ceramic Society* **1989**, *26*, 421–426.

[139] V. K. LaMer, R. H. Dinegar, *Journal of the American Chemical Society* **1950**, *72*, 4847–4854.

[140] T. Ogihara, N. Mizutani, M. Kato, *Ceramics International* **1987**, *13*, 35–40.

[141] H. Kumazawa, Y. Hori, E. Sada, *The Chemical Engineering Journal* **1993**, *51*, 129–133.

[142] S.-K. Lee, M. Ikeda, N. Mizutani, *Journal of the Ceramic Society of Japan* **1991**, *99*, 300–304.

[143] G. T. Dahl, S. Döring, T. Krekeler, R. Janssen, M. Ritter, H. Weller, T. Vossmeyer, *Materials* **2019**, *12*, 2856.

[144] L. Lerot, F. Legrand, P. De Bruycker, *Journal of Materials Science* **1991**, *26*, 2353–2358.

[145] O. Van Cantfort, B. Michaux, R. Pirard, J. P. Pirard, A. J. Lecloux, *Journal of Sol-Gel Science and Technology* **1997**, *8*, 207–211.

[146] B. Yan, C. V. McNeff, P. W. Carr, A. V. McCormick, *Journal of the American Ceramic Society* **2005**, *88*, 707–713.

[147] J. Widoniak, S. Eiden-Assmann, G. Maret, *European Journal of Inorganic Chemistry* **2005**, 3149–3155.

[148] E. W. Leib, U. Vainio, R. M. Pasquarelli, J. Kus, C. Czaschke, N. Walter, R. Janssen, M. Müller, A. Schreyer, H. Weller, T. Vossmeyer, *Journal of Colloid and Interface Science* **2015**, *448*, 582–592.

[149] J. H. Jean, T. A. Ring, *American Ceramic Society Bulletin* **1986**, *65*, 1574–1577.

[150] J. H. Jean, T. A. Ring, *Langmuir* **1986**, *2*, 251–255.

[151] J. H. Jean, T. A. Ring, *Colloids and Surfaces* **1988**, *29*, 273–291.

[152] S. Shukla, S. Seal, R. Vij, S. Bandyopadhyay, *Nano Letters* **2003**, *3*, 397–401.

[153] V. G. Keramidas, W. B. White, *Journal of the American Ceramic Society* **1974**, *57*, 22–24.

[154] R. C. Garvie, *Journal of Physical Chemistry* **1965**, *69*, 1238–1243.

[155] R. C. Garvie, *Journal of Physical Chemistry* **1978**, *82*, 218–224.

[156] J. Livage, K. Doi, C. Mazières, *Journal of the American Ceramic Society* **1968**, *51*, 349–353.

[157] F. Zhang, P. J. Chupas, S. L. A. Lui, J. C. Hanson, W. A. Caliebe, P. L. Lee, S. W. Chan, *Chemistry of Materials* **2007**, *19*, 3118–3126.

[158] R. Srinivasan, L. Rice, B. H. Davis, *Journal of the American Ceramic Society* **1990**, *73*, 3528–3530.

[159] R. Srinivasan, B. H. Davis, O. B. Cavin, C. R. Hubbard, *Journal of the American Ceramic Society* **1992**, *75*, 1217–1222.

[160] M. Bhagwat, V. Ramaswamy, *Materials Research Bulletin* **2004**, *39*, 1627–1640.

[161] M. Dapiaggi, F. Maglia, I. Tredici, B. Maroni, G. Borghini, U. A. Tamburini, *Journal of Physics and Chemistry of Solids* **2010**, *71*, 1038–1041.

[162] W. Pyda, *Journal of the European Ceramic Society* **1997**, *17*, 121–127.

[163] C. Guiot, S. Grandjean, S. Lemonnier, J. P. Jolivet, P. Batail, *Crystal Growth and Design* **2009**, *9*, 3548–3550.

[164] Y. Chang, S. Dong, H. Wang, K. Du, Q. Zhu, P. Luo, *Materials Research Bulletin* **2012**, *47*, 527–531.

[165] E. W. Leib, R. M. Pasquarelli, M. Blankenburg, M. Müller, A. Schreyer, R. Janssen, H. Weller, T. Vossmeyer, *Particle and Particle Systems Characterization* **2016**, *33*, 645–655.

[166] I. Freris, P. Riello, F. Enrichi, D. Cristofori, A. Benedetti, *Optical Materials* **2011**, *33*, 1745–1752.

[167] O. Siiman, A. Burshteyn, *Journal of Physical Chemistry B* **2000**, *104*, 9795–9810.

[168] X. Xia, Y. Liu, V. Backman, G. A. Ameer, *Nanotechnology* **2006**, *17*, 5435–5440.

[169] L. R. Hirsch, J. B. Jackson, A. Lee, N. J. Halas, J. L. West, *Analytical Chemistry* **2003**, *75*, 2377–2381.

[170] Z. J. Jiang, C. Y. Liu, *Journal of Physical Chemistry B* **2003**, *107*, 12411–12415.

[171] S.-C. Yi, C. Y. Kim, C. Y. Jung, S. H. Jeong, W. J. Kim, *Materials Research Bulletin* **2011**, *46*, 12–18.

[172] Z. J. Jiang, C. Y. Liu, L. W. Sun, *Journal of Physical Chemistry B* **2005**, *109*, 1730–1735.

[173] The British Museum, The Lycurgus Cup, licensed under CC BY-NC-SA 4.0, `https://www.britishmuseum.org/collection/object/H_1958-1202-1` (visited on July 23, 2020).

[174] G. T. Dahl, Master Thesis, Universität Hamburg, **2016**.

[175] G. Mie, *Annalen der Physik* **1908**, *330*, 377–445.

[176] S. A. Kalele, A. A. Kundu, S. W. Gosavi, D. N. Deobagkar, D. D. Deobagkar, S. K. Kulkarni, *Small* **2006**, *2*, 335–338.

[177] N. Halas, *MRS Bulletin* **2005**, *30*, 362–367.

[178] M. Brust, M. Walker, D. Bethell, D. J. Schiffrin, R. Whyman, *Chemical Communications* **1994**, 801–802.

[179] D. V. Leff, L. Brandt, J. R. Heath, *Langmuir* **1996**, *12*, 4723–4730.

[180] J. Turkevich, P. C. Stevenson, J. Hillier, *Discussions of the Faraday Society* **1951**, *11*, 55–75.

[181] J. Kimling, M. Maier, B. Okenve, V. Kotaidis, H. Ballot, A. Plech, *Journal of Physical Chemistry B* **2006**, *110*, 15700–15707.

[182] S. K. Sivaraman, S. Kumar, V. Santhanam, *Journal of Colloid and Interface Science* **2011**, *361*, 543–547.

[183] F. Schulz, T. Homolka, N. G. Bastús, V. Puntes, H. Weller, T. Vossmeyer, *Langmuir* **2014**, *30*, 10779–10784.

[184] M. Wuithschick, A. Birnbaum, S. Witte, M. Sztucki, U. Vainio, N. Pinna, K. Rademann, F. Emmerling, R. Kraehnert, J. Polte, *ACS Nano* **2015**, *9*, 7052–7071.

[185] C. Ziegler, A. Eychmüller, *The Journal of Physical Chemistry C* **2011**, *115*, 4502–4506.

[186] W. Baschong, J. M. Lucocq, J. Roth, *Histochemistry* **1985**, *83*, 409–411.

[187] D. G. Duff, A. Baiker, P. P. Edwards, *Journal of the Chemical Society Chemical Communications* **1993**, *272*, 96.

[188] D. G. Duff, A. Baiker, *Studies in Surface Science and Catalysis* **1995**, *91*, 505–512.

[189] S. Oldenburg, R. Averitt, S. Westcott, N. Halas, *Chemical Physics Letters* **1998**, *288*, 243–247.

[190] M. J. García-Soto, O. González-Ortega, *Gold Bulletin* **2016**, *49*, 111–131.

[191] M. Lahav, E. A. Weiss, Q. Xu, G. M. Whitesides, *Nano Letters* **2006**, *6*, 2166–2171.

[192] A. M. Brito-Silva, R. G. Sobral-Filho, R. Barbosa-Silva, C. B. de Araújo, A. Galembeck, A. G. Brolo, *Langmuir* **2013**, *29*, 4366–4372.

[193] C. Graf, A. Van Blaaderen, *Langmuir* **2002**, *18*, 524–534.

[194] C. M. Aguirre, C. E. Moran, J. F. Young, N. J. Halas, *Journal of Physical Chemistry B* **2004**, *108*, 7040–7045.

[195] D. Kandpal, S. Kalele, S. K. Kukarni, *Solid State Phenomena* **2007**, *69*, 277–283.

[196] H. Li, X. Ma, J. Dong, W. Qian, *Analytical Chemistry* **2009**, *81*, 8916–8922.

[197] B. E. Brinson, J. B. Lassiter, C. S. Levin, R. Bardhan, N. Mirin, N. J. Halas, *Langmuir* **2008**, *24*, 14166–14171.

[198] X. Zhang, S. Ye, X. Zhang, L. Wu, *Journal of Materials Chemistry C* **2015**, *3*, 2282–2290.

[199] A. Petrov, H. Lehmann, M. Finsel, C. Klinke, H. Weller, T. Vossmeyer, *Langmuir* **2016**, *32*, 848–857.

[200] N. Phonthammachai, J. C. Y. Kah, G. Jun, C. J. R. Sheppard, M. C. Olivo, S. G. Mhaisalkar, T. J. White, *Langmuir* **2008**, *24*, 5109–5112.

[201] B. Storti, F. Elisei, S. Abbruzzetti, C. Viappiani, L. Latterini, *Journal of Physical Chemistry C* **2009**, *113*, 7516–7521.

[202] Y. Gao, J. Gu, L. Li, W. Zhao, Y. Li, *Langmuir* **2016**, *32*, 2251–2258.

[203] Y. Zhang, Y. Shen, X. Yang, S. Sheng, T. Wang, M. F. Adebajo, H. Zhu, *Journal of Molecular Catalysis A: Chemical* **2009**, *316*, 100–105.

[204] M. Haruta, *Gold Bulletin* **2004**, *37*, 27–36.

[205] G. J. Hutchings, *Catalysis Today* **2005**, *100*, 55–61.

[206] M. Haruta, *Catalysis Today* **1997**, *36*, 153–166.

[207] F. Moreau, G. C. Bond, A. O. Taylor, *Journal of Catalysis* **2005**, *231*, 105–114.

[208] L. Ilieva, J. Sobczak, M. Manzoli, B. Su, D. Andreeva, *Applied Catalysis A: General* **2005**, *291*, 85–92.

[209] M. Ojeda, E. Iglesia, *Angewandte Chemie - International Edition* **2009**, *48*, 4800–4803.

[210] D. Stíbal, J. Sá, J. A. Bokhoven, *Catalysis Science and Technology* **2013**, *3*, 94–98.

[211] S. E. Collins, J. M. Cíes, E. Del Río, M. López-Haro, S. Trasobares, J. J. Calvino, J. M. Pintado, S. Bernal, *Journal of Physical Chemistry C* **2007**, *111*, 14371–14379.

[212] M. Vicario, J. Llorca, M. Boaro, C. de Leitenburg, A. Trovarelli, *Journal of Rare Earths* **2009**, *27*, 196–203.

[213] F. Vindigni, M. Manzoli, T. Tabakova, V. Idakiev, F. Boccuzzi, A. Chiorino, *Applied Catalysis B: Environmental* **2012**, *125*, 507–515.

[214] M. Haruta, T. Kobayashi, H. Sano, N. Yamada, *Chemistry Letters* **1987**, *16*, 405–408.

[215] Y. C. Chang, D. H. Chen, *Journal of Hazardous Materials* **2009**, *165*, 664–669.

[216] M. A. Soria, P. Pérez, S. A. C. Carabineiro, F. J. Maldonado-Hódar, A. Mendes, L. M. Madeira, *Applied Catalysis A: General* **2014**, *470*, 45–55.

[217] V. Idakiev, T. Tabakova, A. Naydenov, Z. Y. Yuan, B. L. Su, *Applied Catalysis B: Environmental* **2006**, *63*, 178–186.

[218] D. He, H. Shi, Y. Wu, B. Q. Xu, *Green Chemistry* **2007**, *9*, 849–851.

[219] F. Menegazzo, F. Pinna, M. Signoretto, V. Trevisan, F. Boccuzzi, A. Chiorino, M. Manzoli, *ChemSusChem* **2008**, *1*, 320–326.

[220] Q. Y. Bi, X. L. Du, Y. M. Liu, Y. Cao, H. Y. He, K. N. Fan, *Journal of the American Chemical Society* **2012**, *134*, 8926–8933.

[221] Q.-Y. Bi, J.-D. Lin, Y.-M. Liu, H.-Y. He, F.-Q. Huang, Y. Cao, *Journal of Power Sources* **2016**, *328*, 463–471.

[222] J. D. Grunwaldt, C. Kiener, C. Wögerbauer, A. Baiker, *Journal of Catalysis* **1999**, *181*, 223–232.

[223] S. Döring, Master Thesis, Universität Hamburg, **2017**.

[224] S. J. Bennison in *Engineering Materials Handbook, Vol. 4: Ceramics and Glasses*, ASM International, Metals Park, OH, **1991**, pp. 304–312.

[225] L. Klauke, Bachelor Thesis, Universität Hamburg, **2018**.

[226] R. F. Gonçalves, M. J. Godinho, E. R. Leite, A. P. MacIel, E. Longo, J. A. Varela, *Journal of Materials Science* **2007**, *42*, 2222–2225.

[227] V. V. Srdic, M. Winterer, A. Moller, G. Miehe, H. Hahn, V. Srdić, M. Winterer, A. Möller, G. Miehe, H. Hahn, V. V. Srdic, M. Winterer, A. Moller, G. Miehe, H. Hahn, *Journal of the American Ceramic Society* **2001**, *84*, 2771–2776.

[228] V. V. Srdić, S. Rakić, Z. Cvejić, *Materials Research Bulletin* **2008**, *43*, 2727–2735.

[229] I. Zorić, M. Zäch, B. Kasemo, C. Langhammer, *ACS Nano* **2011**, *5*, 2535–2546.

[230] A. Petrov, Dissertation, Universität Hamburg, **2016**.

[231] J. C. Y. Kah, N. Phonthammachai, R. C. Y. Wan, J. Song, T. White, S. Mhaisalkar, I. Ahmad, C. Sheppard, M. Olivo, *Gold Bulletin* **2008**, *41*, 23–36.

[232] T. C. Preston, R. Signorell, *ACS Nano* **2009**, *3*, 3696–3706.

[233] Z. Liang, Y. Liu, S. S. Ng, X. Li, L. Lai, S. Luo, S. Liu, *Journal of Nanoparticle Research* **2011**, *13*, 3301–3311.

[234] P. Benjamin, C. Weaver, *Proceedings of the Royal Society of London A* **1960**, *254*, 177–183.

[235] G. T. Dahl, J.-D. Krueger, S. Döring, H. Weller, T. Vossmeyer, *Nanomaterials* **2020**, *10*, 1197.

[236] J.-D. H. Krueger, Bachelor Thesis, Universität Hamburg, **2019**.

[237] F. del Monte, W. Larsen, J. D. Mackenzie, *Journal of the American Ceramic Society* **2000**, *83*, 628–634.

[238] E. L. Delmonico, J. Bertozzi, N. E. de Souza, C. C. Oliveira, *Acta Scientiarum - Technology* **2014**, *36*, 513–519.

[239] J. Zheng, Z. Zhu, H. Chen, Z. Liu, *Langmuir* **2000**, *16*, 4409–4412.

[240] M. Ben Haddada, J. Blanchard, S. Casale, J. M. Krafft, A. Vallée, C. Méthivier, S. Boujday, *Gold Bulletin* **2013**, *46*, 335–341.

[241] S. Marcinko, A. Y. Fadeev, *Langmuir* **2004**, *20*, 2270–2273.

[242] C. Queffélec, M. Petit, P. Janvier, D. A. Knight, B. Bujoli, *Chemical Reviews* **2012**, *112*, 3777–3807.

[243] T. Zhu, X. Fu, T. Mu, J. Wang, Z. Liu, *Langmuir* **1999**, *15*, 5197–5199.

[244] D. Aureau, Y. Varin, K. Roodenko, O. Seitz, O. Pluchery, Y. J. Chabal, *Journal of Physical Chemistry C* **2010**, *114*, 14180–14186.

[245] G. A. Parks, *Chemical Reviews* **1965**, *65*, 177–198.

[246] G. L. Drisko, V. Luca, E. Sizgek, N. Scales, R. A. Caruso, *Langmuir* **2009**, *25*, 5286–5293.

[247] J. P. Brunelle, *Pure and Applied Chemistry* **1978**, *50*, 1211–1229.

[248] B. Liu, Y. Liu, C. Zhu, H. Xiang, H. Chen, L. Sun, Y. Gao, Y. Zhou, *Journal of Materials Science and Technology* **2019**, *35*, 833–851.

[249] T. Aditya, T. Pal, A. Pal, T. Pal, *Chemical Communications* **2015**, *51*, 9410–9431.

[250] O. Proske, *Analyse der Metalle*, 2. Auflage, Springer Verlag, Berlin/Göttingen/ Heidelberg, **1961**, pp. 998–1001.

[251] L. Lutterotti, P. Scardi, *Journal of Applied Crystallography* **1990**, *23*, 246–252.

[252] Institut für Arbeitsschutz der DGUV, GESTIS-Stoffdatenbank, `http://www.d guv.de/ifa/GESTIS/GESTIS-Stoffdatenbank/index.jsp` (visited on Oct. 30, 2019).

[253] VWR Chemicals, Sicherheitsdatenblatt Ammoniak 28% AnalaR NORMAPUR vom 08.04.2018 (accessed on July 31, 2020).

[254] Sigma-Aldrich, Sicherheitsdatenblatt Tetrachlorogold(III)-säure Trihydrat vom 05.11.2019 (accessed on Feb. 11, 2020).

[255] Sigma-Aldrich, Sicherheitsdatenblatt Hydroxypropyl cellulose vom 28.01.2019 (accessed on Oct. 30, 2019).

[256] Merck KgaA, Sicherheitsdatenblatt Magnesium Matrix Modifier vom 05.04.2020 (accessed on July 31, 2020).

[257] The Linde Group, Sicherheitsdatenblatt Stickstoff, verdichtet vom 16.01.2013 (accessed on July 31, 2020).

[258] Sigma-Aldrich, Sicherheitsdatenblatt Palladium(II) nitrate solution vom 29.01.2020 (accessed on July 31, 2020).

[259] Sigma-Aldrich, Sicherheitsdatenblatt Polyvinylpyrrolidon vom 09.10.2019 (accessed on July 31, 2020).

[260] Carl Roth, Sicherheitsdatenblatt Natronlauge 0,1 mol/l Maßlösung vom 08.08.2019 (accessed on Feb. 12, 2020).

[261] Sigma-Aldrich, Sicherheitsdatenblatt Tetrakis-(hydroxymethyl)-phosphonium-chlorid-Lösung vom 24.04.2019 (accessed on Feb. 11, 2020).

[262] Sigma-Aldrich, Sicherheitsdatenblatt Yttrium(III) tris(isopropoxide) vom 01.11.2012 (accessed on Oct. 30, 2019).

[263] ThermoFisher Scientific, Sicherheitsdatenblatt Zirconium(IV) n-propoxide, 70 % w/w in n-propanol vom 22.02.2018 (accessed on Oct. 30, 2019).

[264] Institut für Arbeitsschutz der DGUV, Liste der krebserzeugenden, keimzellmutagenen und reproduktionstoxischen Stoffe (KMR-Stoffe), `https://publikati onen.dguv.de/forschung/ifa/allgemeine-informationen/3517/liste-d er-krebserzeugenden-keimzellmutagenen-und-reproduktionstoxischen-stoffe-kmr-stoffe` (visited on Feb. 12, 2020).

Appendix

Supplementary Material
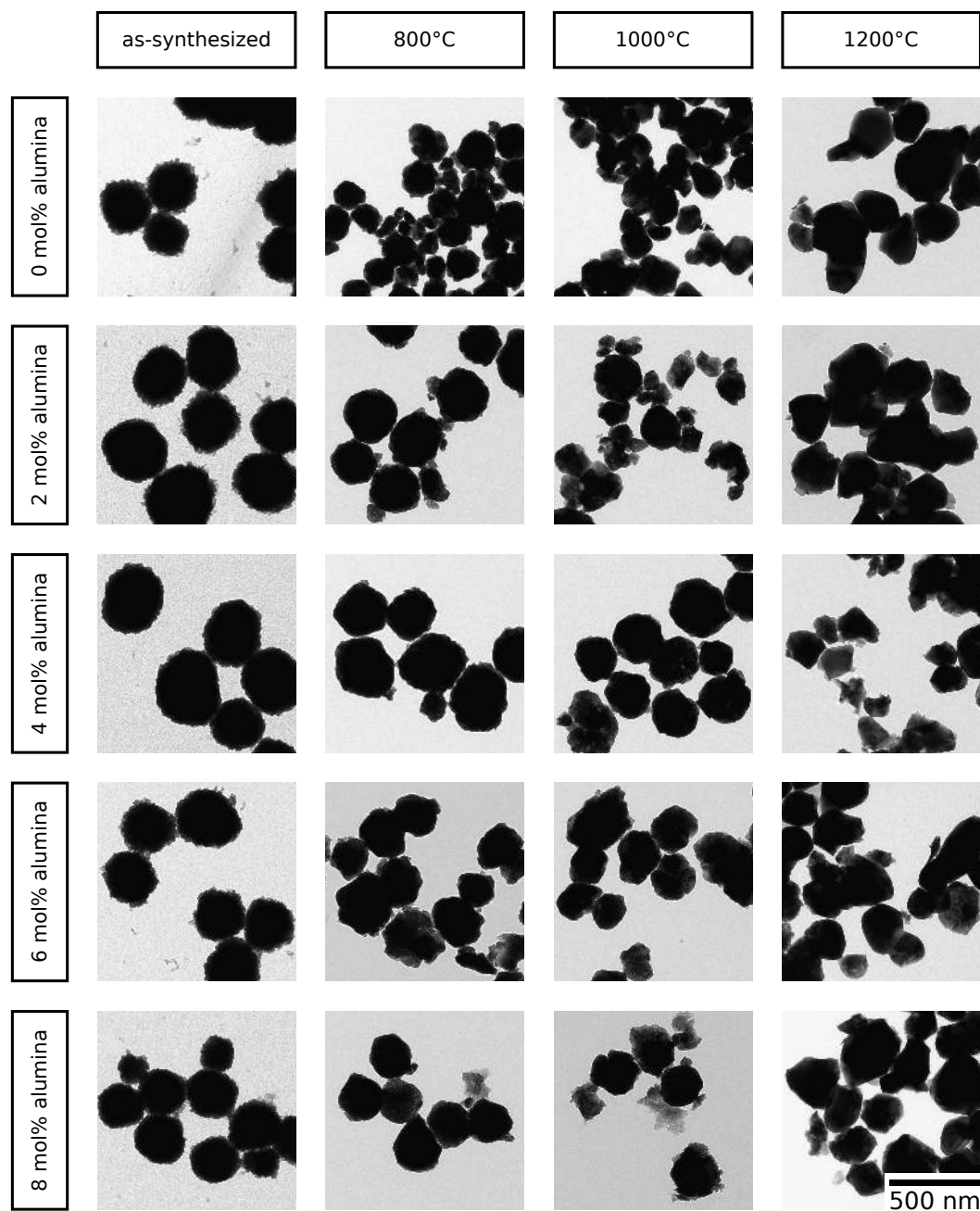
Figure 41: Representative TEM micrographs of zirconia particles doped with 0, 2, 4, 6, and 8 mol-% alumina, as synthesized and after annealing at 800, 1000, and 1200 °C. Licensed under Creative Commons, reprinted from reference [143].
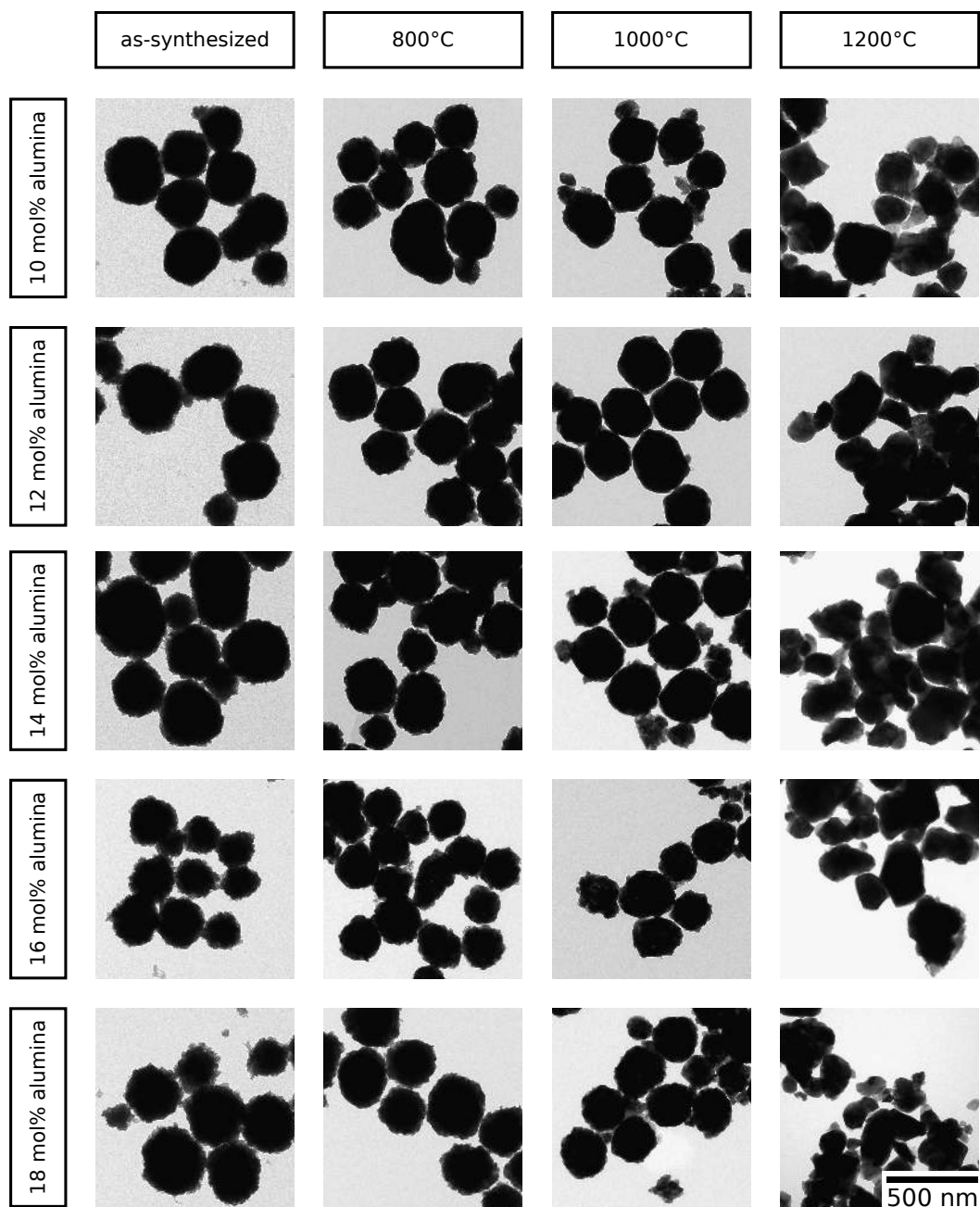
Figure 42: Representative TEM micrographs of zirconia particles doped with 10, 12, 14, 16, and 18 mol-% alumina, as synthesized and after annealing at 800, 1000, and 1200 °C. Licensed under Creative Commons, reprinted from reference [143].
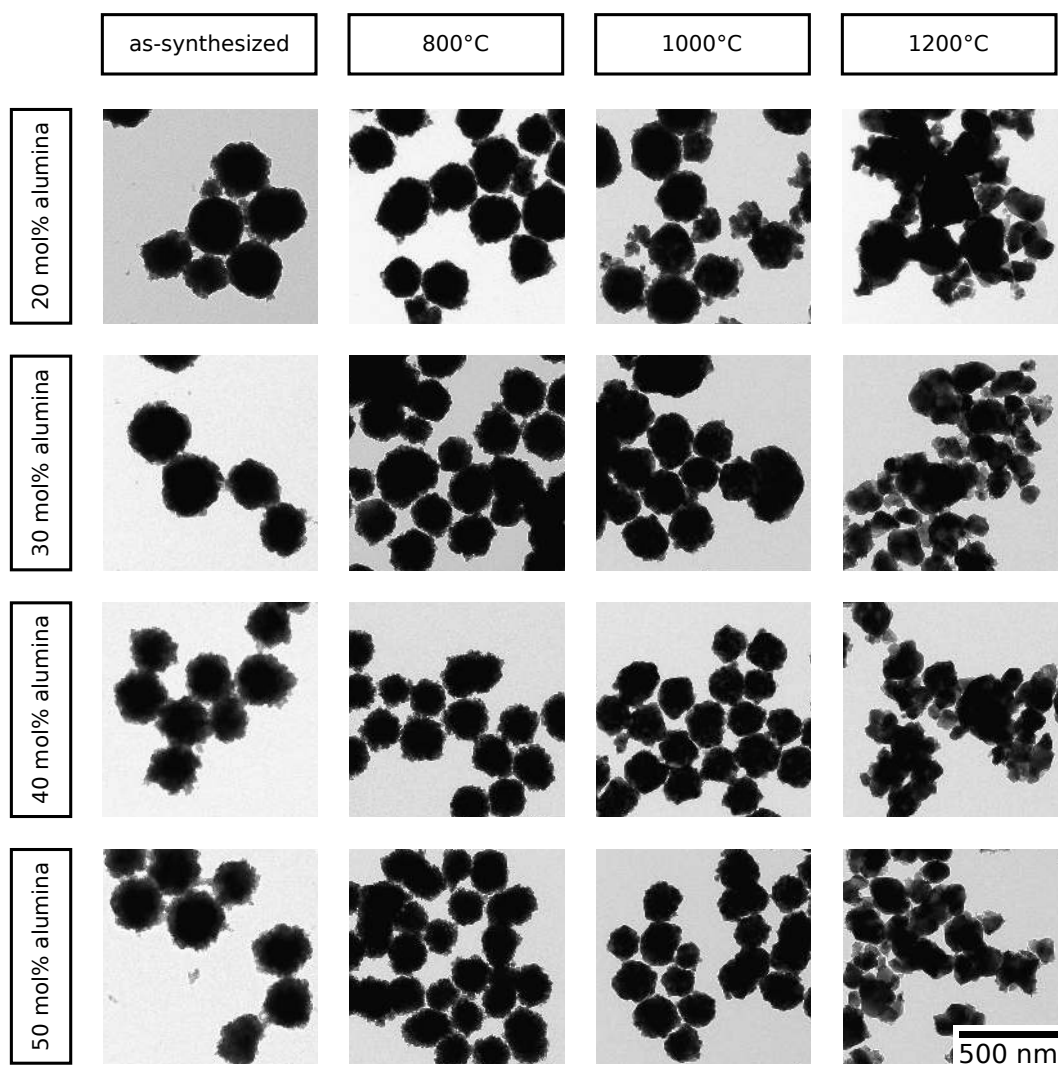
Figure 43: Representative TEM micrographs of zirconia particles doped with 20, 30, 40, and 50 mol-% alumina, as synthesized and after annealing at 800, 1000, and 1200 °C. Licensed under Creative Commons, reprinted from reference [143].
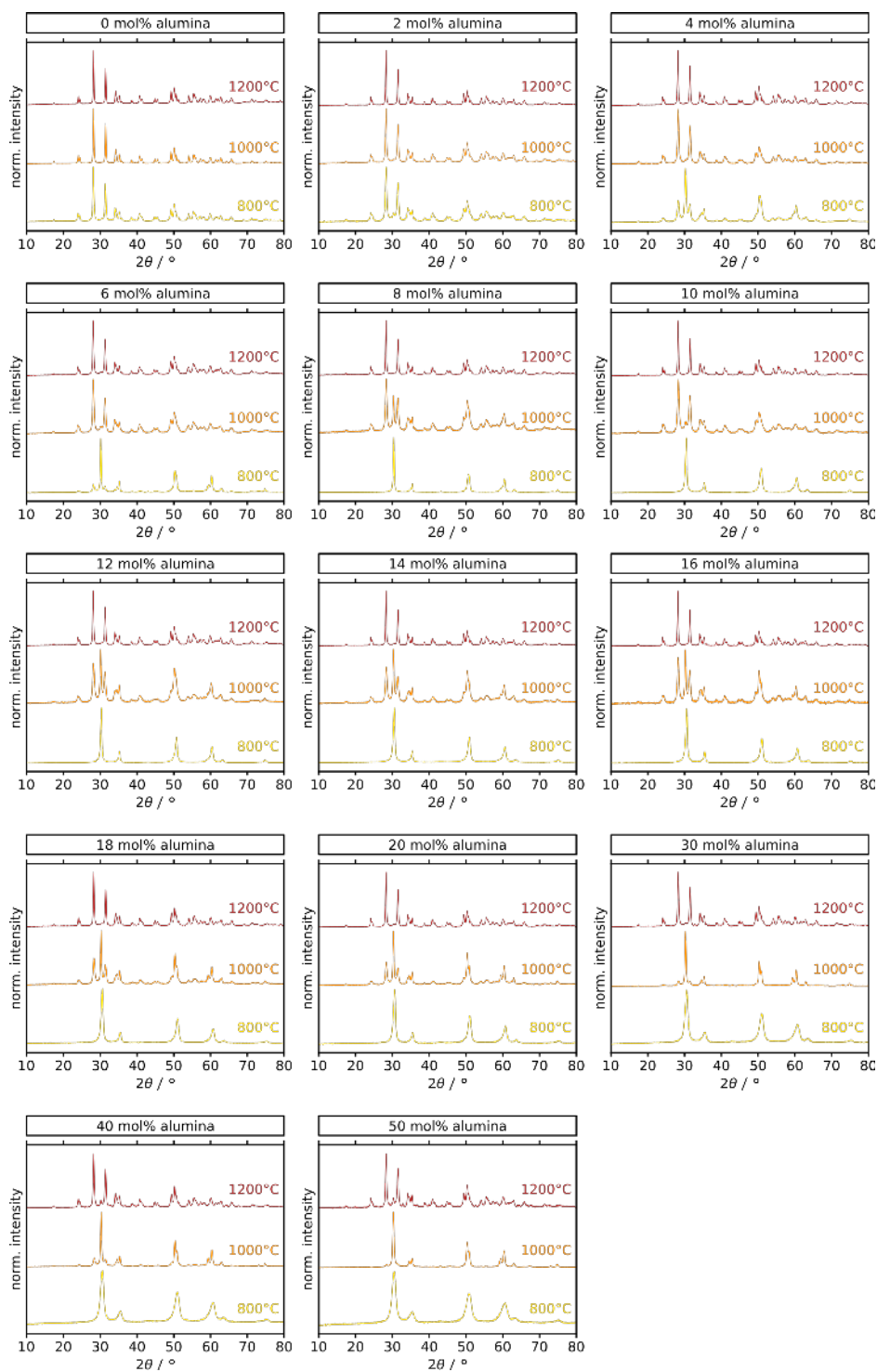
Figure 44: Powder X-ray diffractograms of all alumina-doped particle samples, after annealing at 800, 1000, and 1200 °C for 3 h. Licensed under Creative Commons, reprinted from reference [143].
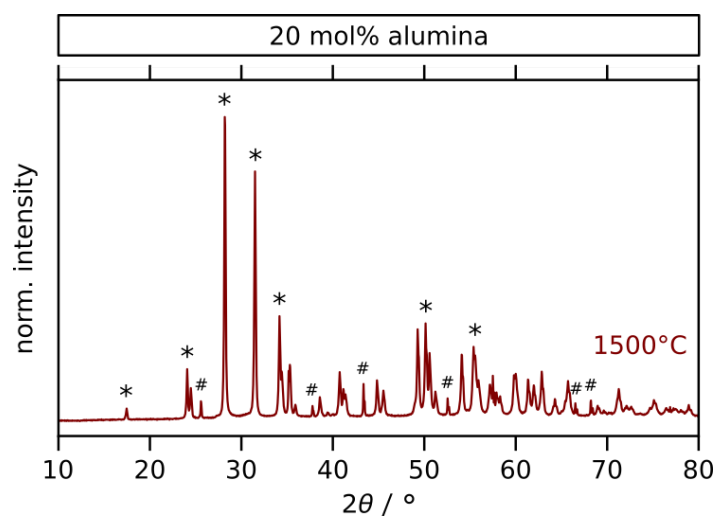
Figure 45: Powder X-ray diffractogram of a particle sample doped with 20 mol-% alumina, after annealing at 1500 °C for 3 h. At this temperature crystallization of α-alumina (#) is clearly visible besides the monoclinic zirconia phase (∗). Licensed under Creative Commons, reprinted from reference [143].

Table 11: XRD characterization results extracted from Rietveld-refined diffractograms for alumina-doped zirconia particle samples, annealed at 800, 1000, and 1200 °C. The alumina contents are given in mol%, temperatures in °C, phase weight fractions (PWF) of monoclinic (m) and tetragonal/cubic (t/c) zirconia in wt%, and average crystallite sizes (CS) in nm. Errors represent the uncertainties in the refinement as given by the software MAUD. Values in brackets are considered inaccurate due to insufficient signal intensities. Licensed under Creative Commons, reprinted from reference [143].

Al_2O_3	T	PWF_m	$PWF_{t/c}$	CS_m	$CS_{t/c}$
	800	97.06 ± 0	2.94 ± 0.2	44.171	(216.931)
0	1000	98.95 ± 0	1.05 ± 0.12	69.944	(101.304)
	1200	99.31 ± 0.52	0.69 ± 0.07	99.683	(99.725)
	800	83.22 ± 0	16.78 ± 1.34	31.123	17.187
2	1000	98.75 ± 1.03	1.25 ± 0.12	62.253	(97.6)
	1200	99.08 ± 0.83	0.92 ± 0.09	85.952	(110.574)
	800	49.89 ± 0.63	50.11 ± 0.39	42.856	26.266
4	1000	72.61 ± 0.33	27.39 ± 1.63	35.175	143.682
	1200	99.11 ± 0.76	0.89 ± 0.07	75.415	(110.067)
	800	38.07 ± 0	61.93 ± 1.66	22.444	46.917
6	1000	72.99 ± 0	26.79 ± 0.52	35.707	92.377
	1200	98.62 ± 0.79	1.38 ± 0.08	71.407	(119.718)
	800	8.77 ± 2.91	91.23 ± 0.98	(28.7584)	42.056
8	1000	69.92 ± 0	30.07 ± 0.7	35.14	27.249
	1200	98.62 ± 0.77	1.38 ± 0.09	78.411	(89.388)
	800	1.50 ± 0.21	98.50 ± 0.96	(6.529)	26.611
10	1000	67.40 ± 0.43	32.60 ± 0.98	32.7	36.642
	1200	98.78 ± 0.75	1.22 ± 0.08	79.487	(120.177)
	800	0.61 ± 0.27	99.39 ± 1.13	(46.95)	27.67
12	1000	65.90 ± 0	33.79 ± 0.29	28.582	28.178
	1200	98.82 ± 0.71	1.18 ± 0.09	73.633	(116.135)
	800	0.62 ± 0.13	99.38 ± 1.03	(30.373)	21.234
14	1000	66.96 ± 0.74	33.04 ± 0.37	27.402	33.818
	1200	98.83 ± 0.88	1.17 ± 0.1	81.666	(96.814)
	800	5.03 ± 0.86	94.97 ± 0.97	(43.277)	20.44
16	1000	62.70 ± 0.64	37.30 ± 0.46	30.156	35.515
	1200	98.90 ± 0.86	1.10 ± 0.09	81.121	(122.794)

Al$_2$O$_3$	T	PWF$_m$	PWF$_{t/c}$	CS$_m$	CS$_{t/c}$
	800	0.54 ± 0.18	99.46 ± 0.48	(98.942)	17.878
18	1000	61.09 ± 0.50	38.91 ± 0.31	27.467	37.484
	1200	98.59 ± 0.86	1.41 ± 0.1	73.356	(73.31)
	800	0.32 ± 0.14	99.67 ± 0.96	(97.286)	17.347
20	1000	60.83 ± 0.34	39.17 ± 0.21	25.872	43.307
	1200	98.35 ± 0.71	1.65 ± 0.09	74.107	(118.225)
	800	0.00 ± 0	100.00 ± 0.75	(100.0)	12.386
30	1000	60.37 ± 0.77	39.63 ± 0.14	21.036	44.055
	1200	98.02 ± 0.9	1.98 ± 0.11	45.925	(126.672)
	800	0.00 ± 0	100.00 ± 0.72	(100.0)	11.42
40	1000	54.76 ± 1.08	45.24 ± 0.33	21.159	39.395
	1200	95.64 ± 0.74	4.36 ± 0.13	41.784	(43.177)
	800	0.00 ± 0	100.00 ± 0.64	(70.375)	9.902
50	1000	30.02 ± 1.1	69.98 ± 0.29	22.942	34.277
	1200	95.28 ± 1.06	4.72 ± 0.17	37.556	(133.199)

Table 12: XRD characterization results extracted from Rietveld-refined diffractograms for alumina-doped, yttria-doped, and alumina/yttria-codoped zirconia particle samples, annealed at 800, 1000, and 1200 °C. Temperatures are given in °C, phase weight fractions (PWF) of monoclinic (m) and tetragonal/cubic (t/c) zirconia in wt%, and average crystallite sizes (CS) in nm. Errors represent the uncertainties in the refinement as given by the software MAUD. Values in brackets are considered inaccurate due to insufficient signal intensities.

sample	T	PWF_m	$PWF_{t/c}$	CS_m	$CS_{t/c}$
	800	14.9 ± 1.5	85.1 ± 1.5	5.78	17.7
20A-1	1000	44.8 ± 0.8	55.2 ± 0.8	19.1	19.1
	1200	95.3 ± 7.6	4.7 ± 7.6	57.7	(9.2)
20A-2	1400	95.5 ± 0.5	4.5 ± 0.5	161.5	(5.6)
	800	4.5 ± 0.8	95.5 ± 0.8	(74.6)	30.6
8Y-1	1000	8.3 ± 0.9	90.7 ± 0.9	(5.54)	44.0
	1200	8.8 ± 0.9	91.2 ± 0.8	(8.0)	50.3
	1400	6.9 ± 0.6	93.1 ± 0.6	(19.4)	173.6
	800	1.9 ± 0.6	98.1 ± 0.6	(97.9)	16.3
20A8Y-1	1000	1.2 ± 0.4	98.6 ± 0.4	(91.4)	36.9
	1200	4.3 ± 0.2	95.7 ± 0.2	(62.0)	51.1
	800	1.4 ± 0.2	98.6 ± 0.2	85.0	(15.0)
20A8Y-2	1000	0.6 ± 0.3	99.4 ± 0.3	(88.7)	24.7
	1200	4.6 ± 0.7	95.4 ± 0.7	(39.2)	55.1
	1400	6.3 ± 0.3	93.7 ± 0.3	(90.7)	54.9

Table 13: Characterization results for all GNP immobilization experiments. The concentrations of HCl, AMPA, and the particle concentration after purification are denoted by c_{HCl}, c_{AMPA}, and c_p, respectively. w_{Au} is the gold weight fraction determined by AAS, A_{450} represents the absorbance at 450 nm in UV/vis/NIR spectroscopy. Uncertainties are determined by the weighing error for c_p and by the weighing error or the standard deviation of double measurements for AAS (whichever is larger). All pH values were obtained with a tolerance of ± 0.15. The sample R2A was a scale-up reproduction of the sample 2A at identical synthesis conditions. Licensed under Creative Commons, reprinted from reference [235].

sample	c_p / $g\,L^{-1}$	w_{Au} / wt%	A_{450}
0	417 ± 33	9.83 ± 0.78	0.618
0A	550 ± 24	13.10 ± 0.54	0.989
1	433 ± 33	3.53 ± 0.09	0.343
1A	467 ± 47	5.22 ± 0.43	0.448
2	533 ± 47	0.98 ± 0.07	0.194
2A	450 ± 71	2.52 ± 0.45	0.282
3	833 ± 33	0.37 ± 0.00	0.100
3A	833 ± 33	0.81 ± 0.01	0.189
4	800 ± 141	0.07 ± 0.01	0.055
4A	917 ± 118	0.58 ± 0.08	0.148
5	850 ± 118	0.07 ± 0.01	0.046
5A	1067 ± 47	0.49 ± 0.02	0.133
6	850 ± 71	0.09 ± 0.00	0.041
6A	583 ± 33	0.74 ± 0.02	0.146
7	500 ± 33	0.11 ± 0.00	0.045
7A	650 ± 71	0.79 ± 0.09	0.158
R2A	650 ± 33	2.83 ± 0.01	0.381

Safety

Chemicals

Table 14: List of chemicals and GHS classifications.

Substance	GHS pictograms	H- and P-statements
aluminum(III) *i*-propoxide[252]		H228 P210
aminomethylphosphonic acid[252]		H314 P280 P305+P351+P338 P310
3-aminopropyl triethoxysilane[252]		H302 H314 H317 P280 P301+P330+P331 P302+P352 P305+P351+P338 P308+P310
ammonium hydroxide solution[253]		H314 H335 H400 P280 P273 P301+P330+P331 P304+P340 P308+P310
aqua regia[252]		H272 H314
L-ascorbic acid[252]	-[a]	-[a]
1-butanol[252]		H226 H302 H318 H315 H335 H336 P210 P280 P302+P352 P304+P340 P305+P351+P338 P313
chloroaruic acid (trihydrate)[254]		H314 H317 P260 P280 P301+P330+P331 P303+P361+P353 P305+P351+P338

[a] Not a hazardous substance or mixture according to Regulation (EC) No. 1272/2008.
This substance is not classified as dangerous according to Directive 67/548/EEC.

Substance	GHS Pictograms	H- and P-statements
ethanol[252]		H225 H319 P210 P240 P305+P351+P338 P403+P233
hydrochloric acid[252]		H290 H314 H335 P260 P280 P303+P361+P353 P304+P340+P310 P305+P351+P338
hydroxypropyl cellulose[255]	-[a]	-[a]
eicosanoic acid[252]	-[a]	-[a]
lithium metaborate[252]	-[a]	-[a]
magnesium nitrate solution[256]		H272 H290 H314 H332 EUH071 P210 P220 P280 P303+P361+P353 P304+P340+P310 P305+P351+P338+P310 P370+P378
nitric acid[252]		H272 H290 H314 H330 EUH071 P280 P301+P330+P331
nitrogen[257]		H280 P403
palladium nitrate solution[258]		H271 H290 H314 H332 H411 EUH071 P210 P273 P280 P303+P361+P353 P304+P340+P312 P305+P351+P338+P310
polyvinylpyrrolidone[259]	-[a]	-[a]

[a] Not a hazardous substance or mixture according to Regulation (EC) No. 1272/2008.
This substance is not classified as dangerous according to Directive 67/548/EEC.

Substance	GHS Pictograms	H- and P-statements
potassium carbonate[252]		H315 H319 H335 P302+P352 P305+P351+P338
1-propanol[252]		H225 H318 H336 P210 P240 P305+P351+P338 P313 P403+P233
sodium carbonate[252]		H319 P260 P305+P351+P338
sodium hydroxide solution (0.1 M)[260]		H290 P234 P390
sulfuric acid[252]		H290 H314 P280 P301+P330+P331 P303+P361+P353 P308+P310
tetraethyl orthosilicate[252]		H226 H332 H319 H335 P210 P261 P280 P303+P361+P353 P304+P340+P312 P370+P378 P403+P235
tetrahydrofuran[252]		H225 H302 H319 H335 H351 EUH019 P210 P280 P301+P312+P330 P305+P351+P338 P370+P378 P403+P235
tetrakis(hydroxymethyl) phosphonium chloride solution (80% in H$_2$O)[261]		H301 H311 H315 H318 H334 H411 P261 P273 P280 P301+P310 P305+P351+P338 P342+P311

[a] Not a hazardous substance or mixture according to Regulation (EC) No. 1272/2008.
This substance is not classified as dangerous according to Directive 67/548/EEC.

Substance	GHS Pictograms	H- and P-statements
water[252]	_a	_a
yttrium(III) *i*-propoxide[262]		H228 H315 H319 H335 P210 P261 P305+P351+P338
zirconium(IV) *n*-propoxide solution (70% w/w in *n*-propanol)[263]		H226 H318 H336 P210 P261 P280 P301+P312 P304+P340 P305+P351+P338 P310

a Not a hazardous substance or mixture according to Regulation (EC) No. 1272/2008.
This substance is not classified as dangerous according to Directive 67/548/EEC.

Hazard and Precautionary Statements

Table 15: List of relevant H-, EUH- and P-statements.

Identifier	Statement
H225	Highly flammable liquid and vapour.
H226	Flammable liquid and vapour.
H228	Flammable solid.
H271	May cause fire or explosion; strong oxidiser.
H272	May intensify fire; oxidiser.
H280	Contains gas under pressure; may explode if heated.
H290	May be corrosive to metals.
H301	Toxic if swallowed.
H302	Harmful if swallowed.
H311	Toxic in contact with skin.
H314	Causes severe skin burns and eye damage.
H315	Causes skin irritation.
H317	May cause an allergic skin reaction.
H318	Causes serious eye damage.

Identifier	Statement
H319	Causes serious eye irritation.
H330	Fatal if inhaled.
H332	Harmful if inhaled.
H334	May cause allergy or asthma symptoms orbreathing difficulties if inhaled.
H335	May cause respiratory irritation.
H336	May cause drowsiness or dizziness.
H351	Suspected of causing cancer.
H400	Very toxic to aquatic life.
H411	Toxic to aquatic life with long lasting effects.
EUH019	May form explosive peroxides.
EUH066	Repeated exposure may cause skin dryness or cracking.
EUH071	Corrosive to the respiratory tract.
P210	Keep away from heat/sparks/open flames/hot surfaces. — No smoking.
P220	Keep/Store away from clothing/.../combustible materials.
P233	Keep container tightly closed.
P234	Keep only in original container.
P235	Keep cool.
P240	Ground/bond container and receiving equipment.
P260	Do not breathe dust/fume/gas/mist/vapours/spray.
P261	Avoid breathing dust/fume/gas/mist/vapours/spray.
P273	Avoid release to the environment.
P280	Wear protective gloves/protective clothing/eye protection/face protection.
P301	IF SWALLOWED:
P302	IF ON SKIN:

Identifier	Statement
P303	IF ON SKIN (or hair):
P304	IF INHALED:
P305	IF IN EYES:
P308	IF exposed or concerned:
P310	Immediately call a POISON CENTER or doctor/physician.
P311	Call a POISON CENTER or doctor/physician.
P312	Call a POISON CENTER or doctor/physician if you feel unwell.
P313	Get medical advice/attention.
P330	Rinse mouth.
P331	Do NOT induce vomitting.
P338	Remove contact lenses, if present and easy to do. Continue rinsing.
P340	Remove victim to fresh air and keep at rest in a position comfortable for breathing.
P342	If experiencing respiratory symptoms:
P351	Rinse cautiously with water for several minutes.
P352	Wash with plenty of soap and water.
P353	Rinse skin with water/shower.
P361	Remove/Take off immediately all contaminated clothing.
P370	In case of fire:
P378	Use appropriate media for extinction.
P390	Absorb spillage to prevent material damage.
P403	Store in a well-ventilated place.

Liste der verwendeten KMR-Stoffe

Nachname: Dahl   Matrikelnummer: 6616724

Vorname: Gregor Thomas   Studiengang: Chemie

Arbeitsbereich: Doktorarbeit

Zeitraum: 10/2016 – 06/2020

Tabelle 16: Auflistung der verwendeten KMR Substanzen, Kat. 1 und 2.[264]

CAS-Nummer	Stoffname (IUPAC)	Verfahren, eingesetzte Menge	Kategorie
109-99-9	Tetrahydrofuran	Silikapartikel-Funktionalisierung, 560 mL	K2
124-64-1	Tetrakis(hydroxymethyl)-phosphoniumchlorid	Goldnanopartikelsynthese, 8.9 µL	K2

_____   _____

Datum   Gregor Thomas Dahl

_____   _____

Datum   Vorgesetzter

Danksagung

Ich bedanke mich bei Horst Weller und Tobias Vossmeyer für die herzliche Aufnahme in die Arbeitsgruppe und die Möglichkeit, dort unter hervorragenden Bedingungen forschen, diskutieren und viel lernen zu können.

Bei Tobias Vossmeyer und Alf Mews möchte ich mich für die Übernahme der Dissertationsgutachten bedanken. Gleichermaßen danke ich Horst Weller, Michael Fröba und Gabriel Bester für die Teilnahme an der Prüfungskommission meiner Disputation.

Mein ganz besonderer Dank gilt Tobias Vossmeyer für die Bereitstellung eines spannenden Forschungsthemas, die stets herausragende inhaltliche und menschliche Unterstützung während meiner Promotionszeit, die vielen lehrreichen Gespräche und Diskussionen und die uneingeschränkte Bereitschaft, bei Problemen und Fragen auch kurzfristig zur Seite zu stehen. Ich schätze seine Hingabe bei der Betreuung meiner Arbeit sehr, durch sie konnte ich in meiner Zeit viel lernen, mich für vieles begesitern und immer wieder neu motivieren. Auch für die Durchsicht meiner Arbeit möchte ich mich bedanken.

Meine Promotion wurde als Teil des Sonderforschungsbereichs (SFB) "M^3 – Maßge-schneiderte Multiskalige Materialsysteme"mit finanzieller Unterstützung durch die Deutsche Forschungsgemeinschaft (DFG) ermöglicht. Hierfür und für die vielfältigen Möglichkeiten, in deren Genuss ich dadurch gekommen bin, bin ich sehr dankbar.

Meinem Vorgänger Alexey Petrov danke ich für die gute Einarbeitung in das Thema, die fachlichen und praktische Unterstützung bei ersten Experimenten im Labor und eine gute Zusammenarbeit in den ersten Monaten meiner Promotion.

Ich möchte mich bei allen Kooperationspartnern und Ko-Authoren im Rahmen des SFB für die gute und fruchtbare Zusammenarbeit, sowie allen Mitarbeitern in diesem spannenden Projekt für viele inspirierende Gespräche und tolle Erfahrungen bedanken. In besonderem Maße gilt mein Dank Tobias Krekeler und Malte Blankenburg für die sehr lehrreiche Unterstützung mit ihrer fachlichen Expertise. Außerdem danke ich dem Team des Graduiertenkollegs, im Besonderen Alette Winter, Ulrike Herzog und Nils Geyer für das Ermöglichen der zahl- und lehrreichen Tutorials und Sommerakademien.

Weiterhin danke ich allen Mitarbeitern der Serviceabteilungen für zahlreiche Analytik und Unterstützung bei der Umsetzung experimenteller Aufbauten, insbesondere Robert Schön, Stefan Werner, Almut Barck, Eugen Klein, Iris Benkenstein, Dirk Eifler, sowie den Glasbläsern und dem Team der Mechanikwerkstatt.

Bei Maik Finsel und Michael Kampferbeck möchte ich mich für das Korrekturlesen dieser Dissertation ganz herzlich bedanken.

Außerdem möchte ich mich herzlich bei meinen studentischen Praktikanten Sebastian Döring, Lea Klauke, Jan-Dominik Krueger, Lennard Jönsson und Ekaterina Salikhova für ihre tatkräftige Unterstützung im Labor und ihre maßgeblichen Beiträge zu den Ergebnissen in dieser Arbeit bedanken.

Meinen alten und neuen Bürokollegen Mazlum Yesilmen, Maik Finsel, Clemens Schröter, Hendrik Schlicke, Svenja Kunze und Sophia Bittinger danke ich für eine tolle Zeit und anregende Gespräche. Auch den Freunden des Tischfußballs Michael Kampferbeck, Jil Rüter, Sebastian Willruth, Alexey Petrov und Daniel Jostes danke ich für viele kurzweilige Mittagspausen und das willkommene Kontrastprogramm zum Forschungsalltag. Darüber hinaus möchte ich mich bei bei meinen Kollegen Bendix Ketelsen, Hauke Hartmann, Rieke Koll, Friederieke Gorris, Felix Thiel, Marius Schuhmacher, und allen aktuellen und ehemaligen Kollegen der gesamten Arbeitsgruppe für die angenehme Arbeitsatmosphäre, viele anregende Gespräche und eine unvergessliche Zeit bedanken.

Den Kolleginnen Beate Kreutzer, Marion Manin, Martina Krasa und Sigrid Zeckert im Sekretariat, sowie Waltraud Wallenius und Uta Fischer im Studienbüro danke ich für die tatkräftige Unterstützung bei allen organisatorischen Belangen. Weiterhin bedanke ich mich bei Kathrin Hoppe für ihr Engagement bei der Koordination der studentischen Praktika.

Bei all meinen Freunden möchte ich mich bedanken für die nötige Ablenkung in der Freizeit, für die ungebrochene Unterstützung und das Verständnis in den vielen Momenten, in denen Freundschaften zugunsten der Arbeit zurückstecken mussten. In diesen Zeiten beweisen sich gute Freundschaften und für die bin ich sehr dankbar.

Zum Schluss danke ich meiner Familie, meiner Oma Christel, meinem Bruder Roman und natürlich ganz ganz besonders meinen Eltern Peter und Katharina. Ihr habt mich seit ich denken kann zu jeder Zeit, in jeder Situation bedingungslos unterstützt, finanziell, mit eurem Rat, eurem Zuspruch und eurer Liebe. Dafür bin ich euch von Herzen dankbar. Ohne eure großartige Hilfe würde ich heute nich da stehen, wo ich stehe. Danke!

Publications

<u>Gregor T. Dahl</u>, Jan-Dominik Krueger, Sebastian Döring, Horst Weller, and Tobias Vossmeyer. Seeded Growth Synthesis of Zirconia@Gold Particles in Aqueous Solution. In: *Nanomaterials*, 10(6), **2020**, p. 1197. doi: 10.3390/nano10061197.

<u>Gregor T. Dahl</u>, Sebastian Döring, Tobias Krekeler, Rolf Janssen, Martin Ritter, Horst Weller, and Tobias Vossmeyer. Alumina-doped zirconia submicro-particles: synthesis, thermal stability, and microstructural characterization. In: *Materials*, 12(18), **2019**, p. 2856. doi: 10.3390/ma12182856.

Maik Finsel, Maria Hemme, Sebastian Döring, Jil Rüter, <u>Gregor T. Dahl</u>, Tobias Krekeler, Andreas Kornowski, Martin Ritter, Horst Weller, and Tobias Vossmeyer. Synthesis and thermal stability of ZrO_2@SiO_2 core-shell submicron particles. In: *Royal Society of Chemistry (RSC) Advances*, 9, **2019**, pp. 26902-26914. doi: 10.1039/C9RA05078G.

Esther Frohnmeyer, Nadine Tuschel, Tobias Sitz, Cornelia Hermann, <u>Gregor T. Dahl</u>, Florian Schulz, Antje J. Baeumner, and Markus Fischer. Aptamer lateral flow assays for rapid and sensitive detection of cholera toxin. In: *Analyst*, 114(5), **2019**, pp. 1840–1849. doi: 10.1039/c8an01616j.

Hendrik Schlicke, Clemens J. Schröter, <u>Gregor T. Dahl</u>, Matthias Rebber, Malte Behrens, and Tobias Vossmeyer. Membranes of organically cross-linked gold nanoparticles: Novel materials for MEMS/NEMS sensors and actuators. In: *IEEE 12th Nanotechnology Materials and Devices Conference (NMDC), Singapore*, **2017**, pp. 109-110. doi: 10.1109/ NMDC.2017.83 50522.

Hendrik Schlicke, Sophia C. Bittinger, Malte Behrens, Mazlum Yesilmen, Hauke Hartmann, Clemens J. Schröter, <u>Gregor T. Dahl</u>, and Tobias Vossmeyer. Electrostatically Actuated Membranes of Cross-Linked Gold Nanoparticles: Novel Concepts for Electromechanical Gas Sensors. In: *Proceedings 2017*, 1(4), **2017**, p. 301. doi: 10.3390/proceedings1040301.

Hendrik Schlicke, Malte Behrens, Clemens J. Schröter, <u>Gregor T. Dahl</u>, Hauke Hartmann, and Tobias Vossmeyer. Cross-Linked Gold-Nanoparticle Membrane Resonators as Microelectromechanical Vapor Sensors. In: *ACS Sensors*, 2(4), **2017**, pp. 540–546. doi: 10.1021/acssensors.6b00831.

Florian Schulz, <u>Gregor T. Dahl</u>, Stephanie Besztejan, Martin A. Schroer, Felix Lehmkühler, Gerhard Grübel, Tobias Vossmeyer, and Holger Lange. Ligand Layer Engineering To Control Stability and Interfacial Properties of Nanoparticles. In: *Langmuir*, 32(31), **2016**, pp. 7897–7907. doi: 10.1021/acs.langmuir.6b01704.

Kely Navakoski de Oliveira, Vincent Andermark, Liliane A. Onambele, <u>Gregor Dahl</u>, Aram Prokop, and Ingo Ott. Organotin complexes containing carboxylate ligands with maleimide and naphthalimide derived partial structures: TrxR inhibition, cytotoxicity and activity in resistant cancer cells. In: *European Journal of Medicinal Chemistry*, 87, **2014**, pp. 794–800. doi: 10.1016/j.ejmech.2014.09.075.

Kely Navakoski de Oliveira, Vincent Andermark, Susanne von Grafenstein, Liliane A. Onambele, <u>Gregor Dahl</u>, Riccardo Rubbiani, Gerhard Wolber, Chiara Gabbiani, Luigi Messori, Aram Prokop, and Ingo Ott. Butyltin(IV) Benzoates: Inhibition of Thioredoxin Reductase, Tumor Cell Growth Inhibition, and Interactions with Proteins. In: *ChemMedChem*, 8, **2013**, pp. 256–264. doi: 10.1002/cmdc.201200505.

Conferences

Tailor-made Multiscale Materials Systems (SFB986) – International Workshop
June 19 – 21, 2019, Hamburg, Germany
Alumina-doped zirconia microparticles for photonic applications: synthesis and thermal stability (poster presentation)
Gregor T. Dahl, Sebastian Döring, Lea Klauke, Tobias Krekeler, Horst Weller, Tobias Vossmeyer

Summer School, SFB 986 Graduate School
June 24 – 28, 2019, Travemünde, Germany
Successful Team Leadership; Career Cornerstones: Active Career Building in Academia and Business

2018 MRS Fall Meeting & Exhibit
November 25 – 30, 2018, Boston, USA
Ceramic Micro-Particles: Building Blocks for High Temperature Applications (poster presentation)
Gregor T. Dahl, Sebastian Döring, Tobias Krekeler, Martin Ritter, Horst Weller, Tobias Vossmeyer

5th International Congress and Expo on Nanotechnology and Materials Science
October 16 – 18, 2017, Dubai, UAE
Thermal stability through doping: zirconia nanoparticles for applications in high-temperature photonics (oral presentation)
Gregor T. Dahl, Maik Finsel, Sebastian Döring, Horst Weller, Tobias Vossmeyer

Summer School, SFB 986 Graduate School
July 03 – 07, 2017, Bad Bevensen, Germany
Concept, Design and Presentation of Academic Posters; Optimizing Strategies for Publishing Research in English

Curriculum Vitae

Lebenslauf entfällt aus datenschutzrechtlichen Gründen

Eidesstattliche Versicherung

Hiermit versichere ich an Eides statt, die vorliegende Dissertation selbst verfasst und keine anderen als die angegebenen Hilfsmittel benutzt zu haben. Die eingereichte schriftliche Fassung entspricht der auf dem elektronischen Speichermedium. Ich versichere, dass diese Dissertation nicht in einem früheren Promotionsverfahren eingereicht wurde.

—————————————————   —————————————————

Ort, Datum   Gregor Thomas Dahl